# Finite Temperature QCD with Domain Wall Fermions

George Tamminga Fleming

Submitted in partial fulfillment of the
requirements for the degree
of Doctor of Philosophy
in the Graduate School of Arts and Sciences

COLUMBIA UNIVERSITY

2001

# ABSTRACT

## Finite Temperature QCD with Domain Wall Fermions

GEORGE TAMMINGA FLEMING

Domain wall fermions are a new lattice fermion formulation which preserves the full chiral symmetry of the continuum at finite lattice spacing, up to terms exponentially small in an extra parameter. We discuss the main features of the formulation and its application to study of QCD with two light fermions of equal mass. We also present numerical studies of the two flavor QCD thermodynamics with $aT = 1/4$.

# Contents

# List of Tables

# List of Figures

# Acknowledgments

First, I would like to thank Martin Perl and Jeff Greensite. Without their excellent guidance, I certainly would not have come to Columbia. I would also like to thank Norman Christ and Bob Mawhinney for their patient support and a multitude of interesting discussions.

I cannot properly express the deep debt of gratitude I owe to Pavlos Vranas. Before I met him, I'd never heard of domain wall fermions and the available thesis topics seemed pretty dull and uninteresting. He opened this whole new field to me and made this project possible. Now I leave Columbia brimming full of wonderful and exciting ideas, thanks to him and the Columbia lattice group as a whole.

Finally, I would like acknowledge the wonderful love and support of my wife and friend, Bonnie Tamminga Fleming. I only hope I can live up to her example as she writes her own dissertation.

# Introductory remarks

For the last fifty years, quantum field theories have been amazingly successful at predicting observable physical phenomena involving elementary particles. A class of quantum field theories called *gauge theories*, because each contains a special internal symmetry called gauge symmetry, accurately describes the interactions, or forces, among elementary particles. Three of the four known fundamental forces (*strong*, *weak*, and *electromagnetic*) are best described by gauge theories. Furthermore, nearly all promising new theories are based on the principle of invariance under local symmetry transformations.

*Quantum Chromodynamics*, or QCD, is the gauge theory of the strong force responsible for binding protons and neutrons together to form nuclei. As a practical matter, although QCD is the underlying microscopic theory responsible for nuclear physics, theorists do not use QCD to study the formation of nuclei. The calculation is possible in principle, but the large number of degrees of freedom render it intractable. However, when particles interact at high energies, the strength of the strong interaction becomes paradoxically weak through the phenomenon called *asymptotic freedom*. Only in this perturbative regime can expansions of QCD in Feynman diagrams be used to successfully describe observed physical processes.

Another approach to understanding QCD employs the formal mathematical equivalence between statistical mechanics and quantum field theories expressed in the Euclidean path integral formalism. Systems described by statistical mechanics also

contain vast numbers of degrees of freedom yet numerical and analytic techniques have been developed to handle them. When QCD is expressed in the Euclidean path integral formalism, the analogy with statistical mechanics becomes manifest with the QCD Lagrangian as the Boltzmann weight. Unfortunately, the path integral over a continuous spacetime is divergent unless the integrals are properly regularized.

Lattice QCD provides this regularization scheme by discretizing the Euclidean spacetime manifold while exactly preserving the internal gauge symmetry. Unfortunately, the continuous Lorentz symmetries of translation and rotation are explicitly broken down to discrete subgroups in the process. The goal is to study QCD on as fine a lattice as possible to understand the continuum limit of infinitesimal lattice spacing where Lorentz symmetries are restored. Due to asymptotic freedom, the ratios of physical observables will become independent of the lattice spacing when the spacing is small enough. For the lattice QCD theorist, accomplishing a few steps toward the continuum limit is an immense undertaking involving large supercomputers. The reward for this effort is the ability to study non-perturbative regimes of QCD.

QCD at finite temperature is a non-perturbative regime where lattice QCD has emerged as an ideal tool for direct study of the thermodynamics. Theorists have long speculated that QCD at sufficiently high temperature or density undergoes a deconfining phase transition where quarks and gluons are no longer confined within meson and baryon bound states. In the limits of either infinite or zero mass quarks, the phase transition is characterized by the behavior of a physical observable called an *order parameter*. In nature, though all the quarks have finite mass, the *up* and *down* quarks are much lighter, as evidenced by the light pion masses. So, it is likely that QCD in our world resembles QCD with two massless quarks. When the quarks are massless, the deconfinement order parameter is associated with the spontaneous breakdown of chiral symmetry, the mechanism that generates massless pions.

In this work, we use a recently developed fermion formulation, *domain wall fermions*, to study aspects of QCD that are strongly influenced by chiral symmetry.

Using fermion formulations that were available in the past, the full chiral symmetry of QCD is broken at finite lattice spacing along with the Lorentz symmetry and can be restored only in the continuum limit. With domain wall fermions, chiral symmetry can be effectively restored at finite lattice spacing, *i.e.* before taking the continuum limit, albeit at some increased computational cost.

In chapter 1, after a brief overview of continuum and lattice QCD formulations intended primarily to fix the notation used in the rest of the work, we then discuss the domain wall fermion formulation and the related overlap fermion formulation. In particular, we develop a framework, based on the Gell-Mann, Oakes, and Renner (GMOR) relation, to discuss how domain wall fermions restore chiral symmetry on the lattice. Finally we discuss in general terms the physics underlying the deconfinement phase transition of QCD.

In chapter 2, we discuss some specific technical issues regarding the efficient implementation of domain wall fermions for numerical simulation with dynamical fermions. We discuss the even-odd preconditioning of the fermion matrix. We also derive the molecular dynamics equations of motion for the fermion action for use in the hybrid Monte Carlo (HMC) algorithm.

In chapter 3, we present the results of numerical simulations of $N_f$=2 QCD with light degenerate quarks. Because domain wall fermions are computationally $\mathcal{O}(10)$–$\mathcal{O}(100)$ times more expensive than standard lattice fermion formulations, we focus our efforts on studying the physics of the finite temperature transition region where the role of chiral symmetry should be of primary importance. Our initial studies on $8^3 \times 4$ lattices located the transition region. Further studies on $16^3 \times 4$ lattices searched for conclusive evidence of critical behavior in the transition region which might indicate the order of the transition. Finally, we make a quantitative estimate of the degree of chiral symmetry restoration in the broken phase using the GMOR framework introduced in chapter 1.

We use the following conventions throughout this work. All lattice fields and bare parameters are to be dimensionless. To compare these dimensionless lattice numbers with their physical dimensionful analogues, we employ the dimensionful lattice spacing. For example, the lattice pion mass $m_\pi$ at a given lattice spacing $a$ may be compared to the physical pion mass $m_\pi^{(phys)}$ by $m_\pi^{(phys)} = m_\pi/a$.

# Chapter 1

# QCD with domain wall fermions

## 1.1 Continuum description

QCD, or Quantum Chromodynamics, is the current best description of the strong nuclear force. The theory contains six types, or *flavors*, of fermions called *quarks*. Analogous to the theory of electrodynamics, where fermions called *electrons* carry electric charge, quarks carry one of three types of color charge. As electrons interact through an electromagnetic gauge field, these color-charged quarks interact through color-electric and color-magnetic gauge fields following a logical extension of Maxwell's field equations. The complex charge structure of QCD yields a far richer theory with quark confinement and gauge field self-interactions not found in the simpler electrodynamics.

QCD is described schematically by the Lagrangian density

$$\mathcal{L} = \mathcal{L}_{\text{quarks}} + \mathcal{L}_{\text{gluons}} \tag{1.1}$$

which yields the action when integrated over space-time. By treating the time coordinate as a complex parameter, we can equivalently define the Lagrangian either on the real time axis (*Minkowski* space-time) or the imaginary time axis (*Euclidean* space-time), as the theory defined on one can be analytically continued to the other. We

choose the Euclidean prescription because it allows the interpretation of the action as a Boltzmann weight in an equivalent statistical mechanics framework.

The first term in the Lagrangian density includes a description of how quarks interact with *gluons*, the bosons that constitute gauge fields

$$\mathcal{L}_{\text{quarks}} = \sum_{j=1}^{N_f} \sum_{\mu=1}^{4} \overline{q}_j \left[ \gamma_\mu \left( \partial_\mu - igA_\mu \right) + m_j \right] q_j. \tag{1.2}$$

The $\gamma_\mu$ are Hermitian matrices which satisfy the anticommutation relations $\{\gamma_\mu, \gamma_\nu\} = 2\delta_{\mu,\nu}$ appropriate for Euclidean space-time. $N_f$ is the number of quark flavors (six), the gauge fields $A_\mu$ are elements of the algebra of the Lie group SU($N_c$)

$$A_\mu = \sum_{a=1}^{N_c^2-1} A_\mu^a \frac{\lambda^a}{2} \tag{1.3}$$

and $N_c$ is the number of color charges (three). The $\lambda^a$ are the generators of the algebra of SU($N_c$) and are normalized

$$\text{tr}\left(\lambda^a \lambda^b\right) = 2\delta^{ab}. \tag{1.4}$$

The second part of the Lagrangian includes a description of the self-interaction of the gluonic fields in the absence of quarks

$$\mathcal{L}_{\text{gluons}} = \textstyle\sum_{\mu,\nu=1}^{4} \frac{1}{2} \text{Tr}\left[ F_{\mu\nu} F_{\mu\nu} \right]. \tag{1.5}$$

$$F_{\mu\nu} = \textstyle\sum_{a=1}^{N_c^2-1} F_{\mu\nu}^a \frac{\lambda^a}{2} = \left( \partial_\mu A_\nu^a - \partial_\nu A_\mu^a + g f^{abc} A_\mu^b A_\nu^c \right) \frac{\lambda^a}{2} \tag{1.6}$$

where $F_{\mu\nu}$ is the Yang-Mills field strength tensor. Note that the summation convention is implied in the right hand side of (1.6). $f^{abc}$ are the structure functions of SU($N_c$) and satisfy the commutation relations

$$\left[\lambda^a, \lambda^b\right] = 2i f^{abc} \lambda^c. \tag{1.7}$$

The action is the Euclidean spacetime integral of the Lagrangian density

$$S\left(A, \overline{q}, q\right) = \int d^4x \left( \mathcal{L}_{\text{quarks}} + \mathcal{L}_{\text{gluons}} \right). \tag{1.8}$$

The partition function is given by the path integral over all possible field configurations

$$Z = \int [\mathcal{D}A][\mathcal{D}\overline{q}][\mathcal{D}q]\ e^{-S(A,\overline{q},q)}. \tag{1.9}$$

Physical quantities are computed as a weighted average of appropriately chosen observables $\mathcal{O}$ over all field configurations, normalized by the partition function

$$\langle \mathcal{O}(A,\overline{q},q)\rangle = \frac{1}{Z}\int [\mathcal{D}A][\mathcal{D}\overline{q}][\mathcal{D}q]\ \mathcal{O}(A,\overline{q},q)\ e^{-S(A,\overline{q},q)}. \tag{1.10}$$

As written, this partition function is formally divergent because it includes integration over an infinite number of gauge configurations which are related by gauge transformations, thus of equal weight in the path integral. Restricting the path integral to sample only one element of each set of gauge-equivalent configurations will resolve this problem. For example, the method of Faddeev and Popov can be used [1, 2]. Even still, there are further divergences which must be carefully regularized to ensure the partition function is well defined.

In addition to invariance under local SU($N_c$) gauge transformations, when the $m_j$=0, the action is also invariant under independent global transformations of the left and right chiral components of the fermion fields. We define the chiral matrix $\gamma_5$ as the last remaining linearly independent matrix that anticommutes with the $\gamma_\mu$ matrices: $\{\gamma_5, \gamma_\mu\}$=0. We then define the chiral projection operators

$$P_\pm = \frac{1 \pm \gamma_5}{2} \tag{1.11}$$

and the right and left components are given by $q_R = P_+ q$ and $q_L = P_- q$. Now the transformations explicitly are

$$\begin{aligned}
q_R &\rightarrow e^{i\alpha_R \frac{\lambda^a}{2}} q_R, \\
q_L &\rightarrow e^{i\alpha_L \frac{\lambda^a}{2}} q_L, \\
q_R &\rightarrow e^{i\theta_R} q_R, \\
q_L &\rightarrow e^{i\theta_L} q_L.
\end{aligned}$$

Formally, these transformations generate the symmetry group $\mathrm{SU}_L(N_f) \otimes \mathrm{SU}_R(N_f) \otimes \mathrm{U}_L(1) \otimes \mathrm{U}_R(1)$. Furthermore, we stress that these are the symmetries of the classical action only. The full theory will only respect a subgroup of these symmetries due to quantum interactions.

The Noether currents commonly associated with these symmetries are the *non-singlet vector current*

$$j^a_\mu(x) = \overline{q}(x)\gamma_\mu \frac{\lambda^a}{2} q(x), \tag{1.12}$$

the *non-singlet axial vector current*

$$j^a_{\mu 5}(x) = \overline{q}(x)\gamma_\mu\gamma_5 \frac{\lambda^a}{2} q(x), \tag{1.13}$$

the *singlet vector current*

$$J_\mu(x) = \overline{q}(x)\gamma_\mu q(x), \tag{1.14}$$

and the *singlet axial vector current*

$$J_{\mu 5}(x) = \overline{q}(x)\gamma_\mu\gamma_5 q(x). \tag{1.15}$$

The conservation of the singlet axial vector current (1.15) is broken by the Adler–Bell–Jackiw (ABJ) anomaly. The conserved charge associated with the singlet vector current (1.14) is the *baryon number* and is conserved even when the bare quark masses are non-zero.

For massless quarks, the remaining non-singlet chiral symmetry may be spontaneously broken by the ground state: $\mathrm{SU}_L(N_f) \otimes \mathrm{SU}_R(N_f) \to \mathrm{SU}_V(N_f)$. This implies that the non-singlet vector current (1.12) is still conserved. It remains conserved even for non-zero quark masses, provided they are degenerate, and the associated conserved charge is called *isospin*. The implied breaking of the non-singlet axial vector current is responsible for the appearance of the $N_f^2 - 1$ Nambu-Goldstone bosons. Though quark mass terms explicitly break this current, for small masses spontaneous and explicit symmetry breaking effects work together to produce light Nambu-Goldstone bosons whose mass is proportional to the square root of the quark mass.

Another interesting consequence of chiral symmetry is the role it plays in the *spectral representation* of the Dirac operator. From equation (1.2), we define the continuum Dirac operator

$$\not{D} = \sum_{\mu} \gamma_\mu \left( \partial_\mu - igA_\mu \right). \tag{1.16}$$

This anti-Hermitian operator has a continuous imaginary eigenvalue spectrum: $\not{D} q_\lambda = i\lambda q_\lambda$, where each eigenvalue occurs with the density $\rho(\lambda)$, normalized so $\int d\lambda\, \rho(\lambda) = 1$. Because $\not{D}$ anticommutes with $\gamma_5$, then for each non-zero eigenvector $q_\lambda$ we can generate a new eigenvector $\gamma_5 q_\lambda = q_{-\lambda}$ whose eigenvalue is the negative of the original

$$\not{D}\left(\gamma_5 q_\lambda\right) = -\gamma_5 \left(\not{D} q_\lambda\right) = -i\lambda \left(\gamma_5 q_\lambda\right) = -i\lambda q_{-\lambda}. \tag{1.17}$$

Thus, non-zero eigenvalues always occur in pairs of opposite sign: $(i\lambda, -i\lambda)$.

A simple application of the spectral representation is to derive the spectral identity that relates the chiral condensate to the pseudoscalar susceptibility in QCD with degenerate quarks. The chiral condensate in a volume $V$ is

$$\begin{aligned} \langle \overline{q} q \rangle &\equiv -\frac{1}{4N_c V} \int_V d^4x \ \langle \overline{q}_x q_x \rangle \\ &= \frac{1}{4N_c V} \mathrm{Tr} \left\langle \left(\not{D} + m\right)^{-1} \right\rangle \\ &= \int_{-\infty}^{+\infty} d\lambda \ \frac{\overline{\rho}(\lambda)}{m + i\lambda} = 2 \int_0^{\infty} d\lambda \ \frac{\overline{\rho}(\lambda)}{m + i\lambda} \end{aligned} \tag{1.18}$$

where we have inserted an extra minus sign so that the symbol $\langle \overline{q} q \rangle$ always represents a positive number for positive $m$. We have chosen the normalization such that $\langle \overline{q} q \rangle \sim 1/m$ as $m \to \infty$. $\overline{\rho}(\lambda)$, an even function, is the quantum average of the eigenvalue density so it depends implicitly on the bare masses and couplings.

The pseudoscalar, or pion, susceptibility is (no sum on $a$)

$$\begin{aligned} \chi_{\pi^a} &= -\frac{2}{4N_c V} \int_V d^4x d^4y \left\langle \overline{q}_y \gamma_5 \frac{\tau^a}{2} q_y \overline{q}_x \gamma_5 \frac{\tau^a}{2} q_x \right\rangle \\ &= \frac{1}{4N_c V} \mathrm{Tr} \left\langle \gamma_5 \left(\not{D} + m\right)^{-1} \gamma_5 \left(\not{D} + m\right)^{-1} \right\rangle \end{aligned} \tag{1.19}$$

where we have implicitly assumed that $N_f \geq 2$. We can anticommute $\not{D}^{-1}$ and $\gamma_5$

$$\begin{aligned} \chi_{\pi^a} &= \frac{1}{4N_cV}\mathrm{Tr}\left\langle (m-\not{D})^{-1}\,(m+\not{D})^{-1}\right\rangle \\ &= \int_{-\infty}^{+\infty} d\lambda\, \frac{\overline{\rho}(\lambda)}{(m-i\lambda)(m+i\lambda)}. \end{aligned} \tag{1.20}$$

If we multiply the right hand side of (1.18) by the identity factor $(m-i\lambda)\,/\,(m-i\lambda)$ and note that $i\lambda\overline{\rho}(\lambda)$ is an odd function, then (1.18) and (1.20) give the identity

$$\langle \overline{q}q\rangle = m\chi_{\pi^a}. \tag{1.21}$$

Finally, we emphasize it is the chiral symmetry, manifested in (1.17), that is responsible for this identity. Not surprisingly, (1.21) can also be derived as the integral form of the flavor non-singlet axial Ward-Takahashi identity, another consequence of chiral symmetry. In section 1.5, we will show that (1.21), within the context of the spectral representation, provides a useful starting point for understanding chiral symmetry breaking for lattice fermions.

## 1.2 Lattice actions for gauge fields

Lattice gauge theories provide a regularization scheme for the divergences of the path integral by discretizing the Euclidean spacetime manifold. Not surprisingly, this discretization process destroys the continuous Lorentz symmetries, leaving only a hypercubic remnant. Other symmetries might also be broken if we make a poor choice when transcribing our continuum action into the lattice scheme. Wilson demonstrated [3] that the local gauge symmetry, at least, can always be exactly preserved on the lattice and other symmetries are restored in the limit of vanishing lattice spacing: $a \to 0$.

We can define the lattice partition function as the integral over all field configurations of the lattice action

$$Z = \int [\mathcal{D}U_\mu]\,[\mathcal{D}\overline{q}]\,[\mathcal{D}q]\, e^{-(S_G+S_F)}. \tag{1.22}$$

Purely gluonic contributions to the action are contained in $S_G$. Fermionic contributions are included in $S_F$ and will be discussed in section 1.3.

Starting from the $A_\mu(x)$ fields of (1.3), we define the *gauge links* $U_\mu(x)$ as the integral of the path ordered exponential of the $A_\mu(x)$ along the link connecting the site $x$ to the neighboring site one lattice spacing away in the $\mu$ direction: $x + \hat{\mu}$. As the $A_\mu(x)$ are elements of the algebra of the gauge group SU($N_c$), the gauge links are elements of the group itself. Additionally, the $U_\mu(x)$ are used to parallel transport quark fields from the site $x + \hat{\mu}$ to the site $x$.

The Wilson action for SU($N_c$) gauge theory in $d$ dimensions is [3]

$$S_G^{(W)} = \beta \sum_x \sum_{\mu<\nu} \left[ 1 - \frac{1}{N_c} \mathrm{ReTr} U_P(x, \mu, \nu) \right] \tag{1.23}$$

where $\mu, \nu \in [1, d]$ and the plaquettes $U_P(x, \mu, \nu)$ are

$$U_P(x, \mu, \nu) = U_\mu(x) U_\nu(x + \hat{\mu}) U_\mu^\dagger(x + \hat{\nu}) U_\nu^\dagger(x). \tag{1.24}$$

When the plaquette is expanded in powers of the lattice spacing, the leading term appearing at $\mathcal{O}(a^2)$ corresponds to the continuum gauge field Lagrangian density (1.5). Terms in the expansion which appear at higher powers of $a$ are called *irrelevant* because their influence vanishes in the continuum limit. Although the analogy with common statistical mechanics notation is intentional, here $\beta$ is a bare parameter of the lattice theory which corresponds to the gauge coupling $g$ in the continuum theory: $\beta = 2N_c/g^2$ as $a \to 0$.

Wilson later proposed [4] introducing irrelevant operators to the gauge action to improve the scaling of Monte Carlo simulations. Here we consider adding only the rectangle operator

$$S_G^{(R)} = \beta \sum_x \left\{ \sum_{\mu<\nu} \left[ 1 - \frac{c_0}{N_c} \mathrm{ReTr} U_P(x, \mu, \nu) \right] + \sum_{\mu \neq \nu} \left[ 1 - \frac{c_1}{N_c} \mathrm{ReTr} U_R(x, \mu, \nu) \right] \right\}. \tag{1.25}$$

We require that the coefficients satisfy the constraint $c_0 + 8c_1 = 1$, as predicted in weak coupling lattice perturbation theory. The rectangles $U_R(x, \mu, \nu)$ are

$$U_R(x,\mu,\nu) = U_\mu(x)U_\mu(x+\hat{\mu})U_\nu(x+2\hat{\mu})U_\mu^\dagger(x+\hat{\mu}+\hat{\nu})U_\mu^\dagger(x+\hat{\nu})U_\nu^\dagger(x). \tag{1.26}$$

In chapter 3, we will compare numerical simulations that include a different choice of gauge action looking for behavior which appears closer to the continuum limit.

## 1.3 Domain wall fermions on lattice boundaries

The standard approach to discretizing the continuum quark Lagrangian density (1.2) is to define the quark fields on lattice sites and replace derivatives with finite differences. For example, we can define the gauge covariant lattice central difference operator corresponding to the covariant derivative in the continuum

$$\nabla(\mu)_{x,x'} \equiv \frac{1}{2a}\left[U_\mu(x)\delta_{x+\hat{\mu},x'} - U_\mu^\dagger(x-\hat{\mu})\delta_{x-\hat{\mu},x'}\right]. \tag{1.27}$$

As we shall see below, this naive prescription leads to the well known problem of species doubling: on a $d$ dimensional finite lattice the discretized action describes $2^d$ identical species, one for each corner of the Brillouin zone. Nielsen and Ninomiya [5, 6] showed when the lattice fermion action is local, Hermitian and translationally invariant then either the fermions are doubled or chiral symmetry of the continuum action is broken on the lattice.

Wilson [7] proposed giving all but one of the doubled fermions a mass proportional to the lattice cutoff by adding an irrelevant term to the fermionic action. Using the lattice central difference operator corresponding to the Laplacian in the continuum

$$\Delta(\mu)_{x,x'} \equiv \frac{1}{a^2}\left[U_\mu(x)\delta_{x+\hat{\mu},x'} - 2\delta_{x,x'} + U_\mu^\dagger(x-\hat{\mu})\delta_{x-\hat{\mu},x'}\right], \tag{1.28}$$

the lattice action for Wilson fermions is

$$S_F^{(W)} = a^d \frac{\overline{\psi}_x}{a^{(d-1)/2}}\left\{\frac{m_0}{a}\delta_{x,x'} + \sum_{\mu=1}^{d}\left[\gamma_\mu \nabla(\mu)_{x,x'} - \frac{ar}{2}\Delta(\mu)_{x,x'}\right]\right\}\frac{\psi_{x'}}{a^{(d-1)/2}}. \tag{1.29}$$

We suppress spin and flavor indices and the summation convention implies summing $x, x'$ over all sites on the lattice. The bare fermion fields $\overline{\psi}$ and $\psi$, the bare mass $m_0$ and coefficient of the irrelevant term $r$ are all dimensionless quantities whereas $\nabla(\mu)$ and $\Delta(\mu)$ are dimensionful according to the powers of the lattice spacing in their definitions. Rearranging terms, we put the action into the standard form of a fermion matrix bilinear

$$S_F^{(W)} = \overline{\psi}_x M_{x,x'}^{(W)} \psi_{x'} \tag{1.30}$$

where $M_{x,x'}^{(W)}$ is the Wilson-Dirac fermion matrix

$$M_{x,x'}^{(W)} = (m_0 + rd)\,\delta_{x,x'} - \sum_{\mu=1}^{d} \frac{1}{2}\left[(r-\gamma_\mu)\,U_\mu(x)\delta_{x+\hat{\mu},x'} + (r+\gamma_\mu)\,U_\mu^\dagger(x-\hat{\mu})\delta_{x-\hat{\mu},x'}\right]. \tag{1.31}$$

For numerical simulation, $r$ is usually set to one to take advantage of the simplified spin structure of the spin projection matrices: $P_{\pm\mu} = (1 \pm \gamma_\mu)/2$.

The free Wilson fermion propagator is obtained by inverting the fermion matrix with all $U_\mu(x)$ set to the identity. We block-diagonalize the fermion matrix by Fourier transform to give

$$\widetilde{M}_p^{(W)} = m_0 - \sum_{\mu=1}^{d} \left[i\gamma_\mu \sin p_\mu + r\,(\cos p_\mu - 1)\right], \tag{1.32}$$

where the $p_\mu$ are dimensionless momenta that reside on the reciprocal lattice and range over $-\pi < p_\mu \leq \pi$. In the massless limit $r \to 0$ corresponding to the naive case above, we see that the propagator has a massless pole when each $p_\mu = 0$ or $\pi$. These are the corners of the Brillouin zone mentioned above and each pole is associated with one doubler species. When $0 < r \leq 1$ only the fermion species with $p_\mu = 0$ remains massless and the others acquire a mass on the order of the lattice cutoff. However, even though we have removed the doublers with the irrelevant Wilson term, chiral symmetry is not restored because the Wilson term commutes with $\gamma_5$.

The domain wall fermion formulation, originally proposed by Kaplan [8], solves the doubling problem while conserving the $\mathrm{SU}_L(N_f) \otimes \mathrm{SU}_R(N_f)$ chiral symmetry

of massless quarks on the lattice through the introduction of an infinite internal dimension which we label with coordinate $s$. To demonstrate the construction, we start with an odd $d+1$ dimensional action of free lattice Wilson fermions, see (1.29), where the bare mass parameter $m_0$ is a function of one direction, the $s$-direction. Although $m_0(s)$ can be any monotonically increasing function that crosses zero, for simplicity we discuss only step function mass terms

$$m_0(s) = \begin{cases} m_+, & s \geq 0 \\ m_-, & s < 0 \end{cases} . \tag{1.33}$$

Despite the presence of a mass term and the lack of chiral symmetry in odd dimensions, there is a normalizable, chiral basis of states that solve the equation

$$M^{(K)}\Psi_p^{\pm} = \left[\sum_{\mu=1}^{d} i\gamma_\mu \sin p_\mu\right] \Psi_p^{+} \tag{1.34}$$

where $M^{(K)}$ is Kaplan's Dirac matrix and $p_\mu$ is a $d$ dimensional momentum. The existence of such a basis indicates the spectrum contains states that propagate as massless fermions in the even $d$ dimensions. Kaplan's solution

$$\Psi_p^{+} = (\pm 1)^s e^{ip\cdot x} e^{-\mu_0|s|}, \quad \sinh\mu_0 \equiv m_0 \tag{1.35}$$

indicates the massless modes are exponentially localized on the domain wall, where the mass changes sign. Furthermore, when the extent $L_s$ along the $s$-direction is infinite, only one chirality of the massless modes is normalizable. So, even when the lattice spacing is finite, the action describes a single massless chiral fermion flavor at scales well below the lattice cutoff in the $L_s \to \infty$ limit.

On a lattice with a finite $L_s$, the solutions of the opposite chirality become normalizable and localized on the boundaries. In essence, the boundaries become anti-domain walls and at low energies the effective theory is naturally vector-like. As the separation between the opposing walls is increased by increasing $L_s$, terms that break chiral symmetry will eventually become negligible due to the exponentially suppressed overlap between modes of opposite chirality on opposite walls. So, domain

wall fermions at large $L_s$ are ideally suited for simulating the massless quarks of a vector-like theory like QCD.

If we reinterpret the $s$-direction as an internal flavor space, then gauge fields are coupled to the fermions in the natural way [9, 10, 11]. We write this as the set of constraints on the gauge field

$$U_{\mu\leq d}(x,s) = U_\mu(x); \qquad U_{d+1}(x,s) = \mathbb{1}. \tag{1.36}$$

From this perspective, domain wall fermions are identical to heavy Wilson fermions in $d$ dimensions that carry an additional flavor index $s$ and derivative terms along this $s$ direction are now interpreted as flavor mixings in a sophisticated mass matrix.

Shamir proposed [12] a variant of domain wall fermions where free boundaries at both ends of the extra direction serve as the domain wall/anti-wall. This variant naturally arises when considering the step function mass term (1.33) in the limit $m_- \to -\infty$, provided we use some care in handling the boundaries. From a practical view, this reduces by half the number of lattice sites necessary to separate the walls a fixed distance. The action is a fermion bilinear

$$S_F^{(\mathrm{dwf})} = \overline{\Psi}_{x,s} M^{(dwf)}_{x,s;x',s'} \Psi_{x',s'}. \tag{1.37}$$

Starting with the Wilson fermion matrix (1.31) we build the flavor mixing matrix from first and second order difference operators and the chiral matrix $\Gamma_5 \equiv \gamma_{d+1}$ of the effective even $d$ dimensional theory

$$M^{(dwf)}_{x,s;x',s'} = M^{(W)}_{x,x'}(-m_0)\delta_{s,s'} + \left[\Gamma_5 \hat{\nabla}_{s,s'} - \frac{r_5}{2}\hat{\Delta}_{s,s'}\right]\delta_{x,x'}. \tag{1.38}$$

The hat notation on the difference operators denotes that the operators are ungauged and dimensionless because both act on a flavor space:

$$\hat{\nabla}_{s,s'} = \frac{1}{2}\left(\delta_{s+1,s'} - \delta_{s-1,s'}\right), \tag{1.39}$$

$$\hat{\Delta}_{s,s'} = \delta_{s+1,s'} - 2\delta_{s,s'} + \delta_{s-1,s'}. \tag{1.40}$$

Following the literature, we collect terms in the action that are diagonal in the $s$-direction into an operator that acts parallel to the $d$ dimensional spacetime

$$M^{(dwf)}_{x,s;x',s'} = D^{\parallel}_{x,x'}\delta_{s,s'} + \delta_{x,x'}D^{\perp}_{s,s'}. \tag{1.41}$$

The parallel piece is simply a Wilson matrix with slightly different mass term, $D^{\parallel}_{x,x'} = M^{(W)}_{x,x'}(-m_0) + r_5\delta_{x,x'}$, which we write out explicitly for completeness

$$\begin{aligned} D^{\parallel}_{x,x'} &= (rd + r_5 - m_0)\,\delta_{x,x'} \\ &\quad - \sum_{\mu=1}^{d} \frac{1}{2}\left[(r-\gamma_\mu)\,U_\mu(x)\delta_{x+\hat{\mu},x'} + (r+\gamma_\mu)\,U^\dagger_\mu(x-\hat{\mu})\delta_{x-\hat{\mu},x'}\right]. \end{aligned} \tag{1.42}$$

The second term is the flavor mixing matrix (with flavor index $s$)

$$D^{\perp}_{s,s'} = \begin{cases} -\left(\frac{r_5-\Gamma_5}{2}\right)\delta_{1,s'} & +m_f\left(\frac{1+\Gamma_5}{2}\right)\delta_{L_s-1,s'} \quad , \quad s=0 \\ -\left(\frac{r_5-\Gamma_5}{2}\right)\delta_{s+1,s'} & -\left(\frac{r_5+\Gamma_5}{2}\right)\delta_{s-1,s'} \quad , \quad 0<s<L_s-1 \\ m_f\left(\frac{1-\Gamma_5}{2}\right)\delta_{0,s'} & -\left(\frac{r_5+\Gamma_5}{2}\right)\delta_{L_s-2,s'} \quad , \quad s=L_s-1 \end{cases}. \tag{1.43}$$

We have included a new parameter $m_f$ that plays the role of generalized boundary conditions in the $s$-direction. For $m_f = 0$ the boundaries are free and for $m_f = \pm 1$ and $r_5 = 1$ the boundaries are (anti)periodic. We shall also see that $m_f$ controls the bare mass for the effective light modes.

Until now, we have included a parameter $r_5$ analogous to the Wilson $r$ because it is possible to find massless modes in the low energy theory for $0 < r_5 \leq 1$ [8]. While $r$ plays the physical role of setting the lattice mass scale of the $2^d - 1$ doubler states for Wilson fermions, $r_5$ has no such physical interpretation. Furthermore, for $r_5 \neq 1$ the massless modes are no longer eigenvectors of $\Gamma_5$. So, for the remainder of this work we will assume $r_5 = 1$.

As in (1.32), we can diagonalize $D^{\parallel}$ in the free case by Fourier transform

$$\widetilde{D}^{\parallel}_p = b(p) - \sum_{\mu=1}^{d} i\gamma_\mu \sin p_\mu \tag{1.44}$$

where $b(p) \equiv 1 - m_0 - \sum_{\mu=1}^{d} r\,(\cos p_\mu - 1)$. As in our previous discussion of Kaplan's formulation, we want to search for a normalizable basis of states upon which the full

domain fermion matrix acts like the chirally symmetric Dirac matrix in $d$ dimensions

$$\widetilde{M}^{(\mathrm{dwf})}_{p;s,s'}\widetilde{\Psi}_{p,s'} = -\sum_{\mu=1}^{d} i\gamma_\mu \sin p_\mu \widetilde{\Psi}_{p,s}. \tag{1.45}$$

Since we chose $r_5 = 1$, the $\widetilde{\Psi}$ should also be eigenvectors of $\Gamma_5$: $\widetilde{\Psi}^{\pm}_{p,s} = \phi^{\pm}_{p,s}u^{\pm}$ where $u^{\pm}$ are constant eigenvectors of $\Gamma_5$.

We can reformulate the problem of identifying this basis into solving the zero eigenvalue problem of a different matrix

$$\mathcal{M}_{p;s,s'} \equiv \widetilde{M}^{(\mathrm{dwf})}_{p;s,s'} + \sum_{\mu=1}^{d} i\gamma_\mu \sin p_\mu \delta_{s,s'} = b(p)\delta_{s,s'} + D^{\perp}_{s,s'}. \tag{1.46}$$

Note that $\mathcal{M}$ essentially contains all the terms in $\widetilde{M}^{(\mathrm{dwf})}$ that can break chiral symmetry in the $d$ dimensional spacetime. So, the basis of chiral states corresponds to the null space of $\mathcal{M}$

$$\mathcal{M}_{p;s,s'}\widetilde{\Psi}_{p,s'} \equiv \left[b(p)\delta_{s,s'} + D^{\perp}_{s,s'}\right]\left(P_+\phi^{+}_{p,s'} + P_-\phi^{-}_{p,s'}\right) = 0 \tag{1.47}$$

where $P_\pm \equiv (1 \pm \Gamma_5)/2$ are chiral projection matrices analogous to (1.11). For $m_f$=0, the eigenvectors which solve this equation are

$$\phi^{\pm}_{p,s} = b(p)^{\mp s}\phi^{\pm}_{p,0} \tag{1.48}$$

If we can choose $m_0$ to satisfy the condition

$$-1 < 1 - m_0 - \sum_{\mu=1}^{d} (\cos p_\mu - 1) < 1 \tag{1.49}$$

then $\Psi^{-}_{p}$ is localized at the boundary $s =$ and, as $L_s \to \infty$, it is the only normalizable solution at any finite $s$. For the zero momentum state, $0 < m_0 < 2$ will satisfy the condition. Similarly, for $2r < m_0 < 2(1 + r)$, $d$ zero momentum doubler states will be bound to the domain wall. It is straightforward to derive the other conditions for the remaining doubler states. If we allow $L_s$ to be finite, $\Psi^{+}$ becomes normalizable and localized at $s = L_s - 1$.

We remind the reader that the states $\widetilde{\Psi}_{p,s}$ are not eigenvectors of the free domain wall fermion Dirac matrix. Since that Dirac matrix is non-Hermitian, it is essential to calculate the free propagator from the Hermitian second order operator: $M^{\dagger(\mathrm{dwf})}M^{(\mathrm{dwf})}$. For non-zero $m_f$, Vranas [13, 14] analytically computed the wave functions of the nearly massless modes and found the effective mass (for $r = 1$) is

$$m_{\mathrm{eff}} = m_0\,(2 - m_0)\left[m_f + (1 - m_0)^{L_s}\right]. \tag{1.50}$$

The $L_s$-dependent contribution is exactly the overlap between the wave functions of the right and left modes on opposite walls.

In the interacting case, the precise shape of the wave functions of the nearly massless modes depends upon each gauge configuration. So it is convenient to define the effective light fermion fields through the projection

$$\begin{aligned} q_x &= P_-\Psi_{x,0} + P_+\Psi_{x,L_s-1} \\ \overline{q}_x &= \overline{\Psi}_{x,L_s-1}P_- + \overline{\Psi}_{x,0}P_+. \end{aligned} \tag{1.51}$$

For large $L_s$, these fields have a large overlap with the nearly massless modes and a vanishing overlap with the other heavy modes described above.

Besides the nearly massless modes, the action also describes $2^d - 1$ fermion doublers that propagate along the wall as massive fermions with the mass of $\mathcal{O}(r/a)$. Furthermore, naive counting suggests there are an additional $2^d\,(L_s - 1)$ massive states in the spectrum. These states will contribute to a bulk infinity as $L_s \to \infty$. In section 1.4, we will identify this divergence and introduce terms into the action to cancel it and preserve the $L_s \to \infty$ limit.

## 1.4 The limit of infinite domain wall separation

Using the rules for integration of Grassmann variables, we can explicitly perform the integration over the fermionic degrees of freedom in the lattice partition function

(1.22). The resulting expression now depends explicitly on only the gauge degrees of freedom

$$Z = \int [\mathcal{D}U_\mu] \, (\det M) \, e^{-S_G} = \int [\mathcal{D}U_\mu] \, e^{-S_{\text{eff}}} \tag{1.52}$$

where $M$ is the lattice Dirac fermion matrix which appears in the fermion action, *e.g.* (1.31) or (1.38), and $S_{\text{eff}} = S_G - \operatorname{Tr} \log M$. Since the fermionic weight in the path integral is given by determinant, we can consider replacing $M$ with a different matrix $M'$ provided $\det M = \det M'$. As we shall see, this freedom allows us to uncover important details about the physics of the lattice fermions. Following the approach of Neuberger [15] and Kikukawa and Yamada [16], we will construct a product of matrices whose determinant is the same as the domain wall fermion Dirac matrix in section 1.3, yet whose $L_s \to \infty$ limit is manifestly apparent.

First, we choose a Weyl basis for the Dirac matrices

$$\gamma_{\mu=1,\cdots,d} = \begin{pmatrix} 0 & \sigma_\mu \\ \sigma_\mu^\dagger & 0 \end{pmatrix}, \tag{1.53}$$

where each block is a $2^{\frac{d}{2}-1} \times 2^{\frac{d}{2}-1}$ matrix. We define the $q \times q$ matrices

$$B = (rd + 1 - m_0) \, \delta_{x,x'} - \frac{r}{2} \sum_{\mu=1}^{d} \left[ U_\mu(x) \delta_{x+\hat{\mu},x'} + U_\mu^\dagger(x-\hat{\mu}) \delta_{x-\hat{\mu},x'} \right], \tag{1.54}$$

$$C = \frac{1}{2} \sum_{\mu=1}^{d} \sigma_\mu \left[ -U_\mu(x) \delta_{x+\hat{\mu},x'} + U_\mu^\dagger(x-\hat{\mu}) \delta_{x-\hat{\mu},x'} \right]. \tag{1.55}$$

where $q = 2^{\frac{d}{2}-1} N_f N_c \Omega$ and $\Omega$ is the number of lattice sites in the $d$ dimensional spacetime. This block notation allows us to write the matrix $D^{\|}$ of section 1.3, see (1.42), in the compact form of a $2q \times 2q$ block matrix

$$D^{\|} = \begin{pmatrix} B & -C \\ C^\dagger & B \end{pmatrix} \tag{1.56}$$

Continuing with the same strategy, the full domain wall fermion Dirac matrix in

(1.41) can be written as the block matrix

$$M^{(dwf)} = \begin{pmatrix} B & -C & 0 & 0 & & & m_f & 0 \\ C^\dagger & B & 0 & -1 & & & 0 & 0 \\ -1 & 0 & \ddots & & \ddots & & & \\ 0 & 0 & & & & & & \\ & & \ddots & & \ddots & & 0 & 0 \\ & & & & & & 0 & -1 \\ 0 & 0 & & & -1 & 0 & B & -C \\ 0 & m_f & & & 0 & 0 & C^\dagger & B \end{pmatrix}. \tag{1.57}$$

It is a potential advantage of this block form that we can permute blocks of rows and columns, leaving the determinant unchanged up to a sign. If $q$ is even, which is always true if $d \geq 4$, then the sign is always positive. We choose the set of permutations to make $M^{(dwf)}$ as block lower triangular as possible, leaving a single non-zero block in the upper right corner. This is done by swapping pairs of block columns and then moving the first block-column on the left all the way to the right. The new matrix $M'^{(dwf)}$ in terms of $2q \times 2q$ blocks is

$$M'^{(dwf)} = \begin{pmatrix} \alpha_1 & & & \beta_{L_s} \\ \beta_1 & \ddots & & \\ & \ddots & \alpha_{L_s-1} & \\ & & \beta_{L_s-1} & \alpha_{L_s} \end{pmatrix} \tag{1.58}$$

where the $\alpha_s$ and $\beta_s$ are block lower triangular

$$\alpha \equiv \alpha_{1,\cdots,L_s-1} = \begin{pmatrix} B & 0 \\ C^\dagger & -1 \end{pmatrix}, \qquad \alpha_{L_s} = \alpha \begin{pmatrix} 1 & 0 \\ 0 & -m_f \end{pmatrix} \tag{1.59}$$

$$\beta \equiv \beta_{1,\cdots,L_s-1} = \begin{pmatrix} -1 & -C \\ 0 & B \end{pmatrix}, \qquad \beta_{L_s} = \begin{pmatrix} -m_f & 0 \\ 0 & 1 \end{pmatrix} \beta. \tag{1.60}$$

We use the technique suggested by Neuberger [15] to simplify the determinant of the nearly lower triangular $M'^{(dwf)}$. First, we factor (1.58) into the product of a lower

triangular and an upper triangular matrix

$$M'^{(dwf)} = \begin{pmatrix} \alpha & & & 0 \\ \beta & \ddots & & \\ & \ddots & \alpha & \\ & & \beta & \alpha_{L_s} \end{pmatrix} \begin{pmatrix} 1 & & & -v_1 \\ & \ddots & & \vdots \\ & & 1 & -v_{L_s-1} \\ & & & (1-v_{L_s}) \end{pmatrix} \tag{1.61}$$

where the $v_s$ are given by

$$\begin{aligned} v_s &= \left(-\alpha^{-1}\beta\right)^s \begin{pmatrix} -m_f & 0 \\ 0 & 1 \end{pmatrix}, \\ v_{L_s} &= \begin{pmatrix} 1 & 0 \\ 0 & -1/m_f \end{pmatrix} \left(-\alpha^{-1}\beta\right)^{L_s} \begin{pmatrix} -m_f & 0 \\ 0 & 1 \end{pmatrix}. \end{aligned} \tag{1.62}$$

As $\alpha$ is block lower triangular, it is straightforward to compute it's inverse in block form. Now the determinant is

$$\begin{aligned} \det M^{(dwf)} &= (\det \alpha)^{L_s-1} \det \alpha_{L_s} \det (1-v_{L_s}) \\ &= (-1)^{qL_s} (\det B)^{L_s} \det \left[ \begin{pmatrix} -m_f & 0 \\ 0 & 1 \end{pmatrix} - T^{-L_s} \begin{pmatrix} 1 & 0 \\ 0 & -m_f \end{pmatrix} \right]. \end{aligned} \tag{1.63}$$

where it simplifies what is to follow if we define the $2q \times 2q$ matrix $T$ and its inverse

$$T \equiv \begin{pmatrix} B^{-1} & -B^{-1}C^\dagger \\ -CB^{-1} & CB^{-1}C^\dagger + B \end{pmatrix} \tag{1.64}$$

$$T^{-1} = \begin{pmatrix} C^\dagger B^{-1} C + B & C^\dagger B^{-1} \\ B^{-1}C & B^{-1} \end{pmatrix}. \tag{1.65}$$

At this point we have already made substantial progress since the dimensionality of the matrices on the right hand side of (1.63) no longer depend on $L_s$.

However, to fully expose the $L_s \to \infty$ limit, we should find a way to raise $T^{-1}$ to an arbitrarily large power. Let $\mathbb{1}$ be the $2q \times 2q$ identity matrix and $\Gamma_5$ be the $2q \times 2q$ block matrix

$$\Gamma_5 \equiv \begin{pmatrix} 1 & 0 \\ 0 & -1 \end{pmatrix}. \tag{1.66}$$

Using these matrices and the identities

$$\begin{pmatrix} 1 & 0 \\ 0 & -m_f \end{pmatrix} = \frac{1}{2}\left[(1-m_f)\mathbb{1} + (1+m_f)\Gamma_5\right] \tag{1.67}$$

$$\begin{pmatrix} -m_f & 0 \\ 0 & 1 \end{pmatrix} = \frac{1}{2}\left[(1-m_f)\mathbb{1} - (1+m_f)\Gamma_5\right] \tag{1.68}$$

we can bring $\det M^{(dwf)}$ into the form

$$\begin{aligned} \det M^{(dwf)} &= (-1)^{qL_s}\left(\det B\right)^{L_s} \det\left(\mathbb{1} + T^{-L_s}\right) \det\Gamma_5 \\ &\quad \times \det\frac{1}{2}\left[-(1+m_f)\mathbb{1} - (1-m_f)\Gamma_5 \tanh\left(-\frac{L_s}{2}\log T\right)\right] \\ &= (-1)^{q(L_s+1)}\left(\det B\right)^{L_s} \det\left(\mathbb{1} + e^{L_s H}\right) \\ &\quad \times \det\left[\frac{(1+m_f)\mathbb{1} + (1-m_f)\Gamma_5 \tanh(\frac{L_s}{2}H)}{2}\right]. \end{aligned} \tag{1.69}$$

where in the second equation we have used $\det\Gamma_5 = (-1)^q$ and defined the $2q \times 2q$ matrix $H \equiv -\log T$.

Finally, we see the $L_s \to \infty$ limit of (1.69) is divergent from the factors $\left(\det B\right)^{L_s}$ and $\det\left(\mathbb{1} + e^{L_s H}\right)$. This should not come as a surprise if we recall that domain wall fermions can be interpreted as a theory of $L_s$ heavy Wilson fermions that mix to create low energy chirally symmetric massless modes. We should remove this bulk divergence if our partition function is to correctly model a single light fermion flavor.

A simple method to remove the contribution of the heavy modes was proposed by Vranas [13, 14]. For $m_f = 1$ the last determinant factor in (1.69) is unity. So, if we divide the partition function for arbitrary $m_f$ by the partition function with fixed $m_f$=1, we will cancel the bulk divergence and render finite the $L_s \to \infty$ limit. The technique used to place the determinant into the denominator is to add Pauli-Villars regulator fields[1] into the action with the same Dirac matrix as the fermion fields except with fixed $m_f$=1. In the path integral over the Pauli-Villars fields, the integration

[1] Pauli-Villars fields, also called *pseudofermions,* commute like bosons yet have the same matrix spin structure as fermions.

is now Gaussian rather than Grassmannian, so the determinant of the Pauli-Villars matrix will appear in the denominator. Explicitly, the proposed partition function is

$$\begin{aligned} Z^{(\mathrm{dwf})} &= \int [\mathcal{D}U] \left[\mathcal{D}\overline{\Psi}\right] [\mathcal{D}\Psi] \left[\mathcal{D}\Phi_{PV}^{\dagger}\right] [\mathcal{D}\Phi_{PV}] \, e^{-\left(S_G + S_F^{(\mathrm{dwf})} + S_{PV}^{(\mathrm{dwf})}\right)} \\ &= \int [\mathcal{D}U] \, \frac{\det M(m_f)}{\det M(m_f=1)} e^{-S_G} \\ &= \int [\mathcal{D}U] \det \left[ \frac{(1+m_f)\mathbb{1} + (1-m_f)\Gamma_5 \tanh(\frac{L_s}{2} H)}{2} \right] e^{-S_G} \end{aligned} \tag{1.70}$$

where

$$S_{PV}^{(\mathrm{dwf})} = \Phi_{PV}^{\dagger} M^{(dwf)}(m_f=1) \Phi_{PV} \tag{1.71}$$

is the Pauli-Villars action defined as in (1.37). As we shall see in chapter 2, it is sometimes convenient to also rewrite the fermionic path integral in terms of pseudofermions as well

$$Z^{(\mathrm{dwf})} = \int [\mathcal{D}U] \left[\mathcal{D}\overline{\Phi}_F\right] [\mathcal{D}\Phi_F] \left[\mathcal{D}\Phi_{PV}^{\dagger}\right] [\mathcal{D}\Phi_{PV}] \, e^{-\left(S_G + S_F^{(\mathrm{dwf})} + S_{PV}^{(\mathrm{dwf})}\right)} \tag{1.72}$$

where the fermionic action is now written as

$$S_F^{(\mathrm{dwf})} = \Phi_F^{\dagger} \left[M^{(dwf)}\right]^{-1} \Phi_F. \tag{1.73}$$

To take the $L_s \to \infty$ limit of (1.70), we recall that the hyperbolic tangent function converges to the sign function

$$\lim_{n\to\infty} \tanh(nx) = \epsilon(x) \equiv \begin{cases} 1, & x > 0 \\ -1, & x < 0 \end{cases}. \tag{1.74}$$

Then the fermion determinant for QCD with exact chiral symmetry is

$$\left. \frac{\det M(m_f)}{\det M(m_f=1)} \right|_{L_s\to\infty} = \det \left[ \frac{(1+m_f)\mathbb{1} + (1-m_f)\Gamma_5 \epsilon(H)}{2} \right]. \tag{1.75}$$

So, we have achieved our goal of finding the contribution to the partition function of domain wall fermions in the $L_s \to \infty$ limit.

As an aside, it is possible to construct a transfer matrix formulation of domain wall fermions analogous to the Hamiltonian formulation of lattice gauge theory. The

crucial difference is that the domain wall Hamiltonian corresponds to evolution along the $s$-direction rather than in time. Due to the trivial gauge links in this direction, it is possible to construct a Hamiltonian that is $s$-independent. The matrix $T$ introduced in (1.64) and its logarithm $H$ are the $s$-independent transfer matrix and Hamiltonian of this formulation. Finally, we note the domain wall fermion transfer matrix formulation described here is just a specific case of the overlap formulation [17, 18, 19].

## 1.5 Effects of finite domain wall separation

In the preceding section, we have described how domain wall fermions restore chiral symmetry in the limit of infinite domain wall separation. However, for numerical simulations we must necessarily work at finite domain separation. For physical quantities defined at large distances, we expect that the effect of the chiral symmetry breaking induced by finite $L_s$ is to shift the bare mass $m_f$ by some small additive piece $m_{\text{res}}$, the residual mass. By examining the non-singlet axial Ward-Takahashi identity, we hope to identify and measure the residual mass in the confined phase of QCD.

The domain wall fermion action (1.37) with degenerate quark masses is invariant under a global $\mathrm{SU}_V(N_f)$ symmetry. Following Furman and Shamir [17], we can define the corresponding $d+1$ dimensional conserved non-singlet vector current as

$$\begin{aligned} \mathcal{J}^a_{\mu=1,\cdots,d}(x,s) &= \overline{\psi}_{x,s}\left(\frac{1-\gamma_\mu}{2}\right)U_\mu(x)\frac{\lambda^a}{2}\psi_{x+\hat{\mu},s} \\ &\quad -\overline{\psi}_{x+\hat{\mu},s}\left(\frac{1+\gamma_\mu}{2}\right)U^\dagger_\mu(x)\frac{\lambda^a}{2}\psi_{x,s} \end{aligned} \tag{1.76}$$

$$\mathcal{J}^a_{d+1}(x,s) = \begin{cases} \overline{\psi}_{x,s}P_-\frac{\lambda^a}{2}\psi_{x,s+1} - \overline{\psi}_{x,s+1}P_+\frac{\lambda^a}{2}\psi_{x,s}, & 0 \le s < L_s-1 \\ \overline{\psi}_{x,L_s-1}P_-\frac{\lambda^a}{2}\psi_{x,0} - \overline{\psi}_{x,0}P_+\frac{\lambda^a}{2}\psi_{x,L_s-1}, & s = L_s-1 \end{cases} \tag{1.77}$$

We can see immediately this current is conserved as its divergence vanishes

$$\sum_{\mu=1}^{d+1}\partial_\mu\mathcal{J}^a_\mu(x,s) = 0. \tag{1.78}$$

However, as the low energy effective theory is $d$ dimensional QCD, we can also define a conserved $d$ dimensional vector current. Towards this end, we move the terms in (1.78) for $\mu = d+1$ to the right hand side to define the continuity equation

$$\sum_{\mu=1}^{d} \partial_\mu \mathcal{J}^a_\mu(x,s) = \begin{cases} -\mathcal{J}^a_{d+1}(x,0) - m_f \mathcal{J}^a_{d+1}(x, L_s-1), & s = 0 \\ -\mathcal{J}^a_{d+1}(x,s) + \mathcal{J}^a_{d+1}(x, s-1), & 0 < s < L_s - 1 \\ m_f \mathcal{J}^a_{d+1}(x, L_s-1) + \mathcal{J}^a_{d+1}(x, L_s-2), & s = L_s - 1 \end{cases} , \tag{1.79}$$

where $\partial_\mu \mathcal{J}^a_\mu(x,s) = \mathcal{J}^a_\mu(x,s) - \mathcal{J}^a_\mu(x-\hat{\mu}, s)$ for $\mu = 1, \cdots, d$. If we define the $d$ dimensional non-singlet vector current as

$$\mathcal{V}^a_\mu(x) = \sum_{s=0}^{L_s-1} \mathcal{J}^a_\mu(x,s) \tag{1.80}$$

then we can see from (1.79) that it is also divergenceless: $\sum_{\mu=1}^{d} \partial_\mu \mathcal{V}^a_\mu(x) = 0$. So, isospin is a symmetry of the low energy effective action of domain wall fermions.

To proceed as above to construct a $d$ dimensional axial vector current is not so straightforward as it cannot be uniquely defined. Clearly, opposite chiral rotations should be applied to the states on opposing walls. Following Furman and Shamir [17] we perform opposite chiral transformations on each half of the fermions in the $s$-direction. Analogous to (1.80), the corresponding $d$ dimensional non-singlet axial vector current is

$$\mathcal{A}^a_\mu(x) = \sum_{s=0}^{L_s-1} \epsilon\left(s - \frac{L_s-1}{2}\right) \mathcal{J}^a_\mu(x,s) \tag{1.81}$$

where our notation assumes, for simplicity, that $L_s$ is even. Unlike the vector current in (1.78), the divergence of the axial vector current has two contributions that do not trivially vanish

$$\sum_{\mu=1}^{d} \partial_\mu \mathcal{A}^a_\mu(x) = 2m_f \mathcal{J}^a_{d+1}(x, L_s-1) + 2\mathcal{J}^a_{d+1}(x, L_s/2). \tag{1.82}$$

When expressed in terms of the fields $q_x, \overline{q}_x$ of (1.51), $\mathcal{J}^a_{d+1}(x, L_s-1)$ takes the familiar form of the pseudoscalar density

$$\mathcal{J}^a_{d+1}(x, L_s-1) = \overline{q}_x \gamma_5 \frac{\lambda^a}{2} q_x. \tag{1.83}$$

Thus, when $m_f \neq 0$ the first term reproduces the correct contribution expected from a naive fermion mass term. Although the second contribution, $\mathcal{J}^a_{d+1}(x, L_s/2)$, does not vanish for finite $L_s$, we present numerical results in section 3.4 that indicate it is exponentially suppressed.

To better understand the consequences of working at finite $L_s$, we will follow the role of $\mathcal{J}^a_{d+1}(x, L_s/2)$ as we derive the Gell-Mann, Oakes, and Renner (GMOR) relation [20] in the domain wall framework [21, 22]. We start with the axial Ward-Takahashi identity

$$\begin{aligned}\sum_{\mu=1}^{d} \partial_\mu \left\langle \mathcal{A}^a_\mu(x)\ \overline{q}_0 \gamma_5 \frac{\lambda^a}{2} q_0 \right\rangle &= 2m_f \left\langle \overline{q}_x \gamma_5 \frac{\lambda^a}{2} q_x\ \overline{q}_0 \gamma_5 \frac{\lambda^a}{2} q_0 \right\rangle \\ &\quad +2 \left\langle \mathcal{J}^a_{d+1}(x, L_s/2)\ \overline{q}_0 \gamma_5 \frac{\lambda^a}{2} q_0 \right\rangle \\ &\quad -\delta_{x,0} \left\langle \overline{q}_0 q_0 \right\rangle \end{aligned} \tag{1.84}$$

where the last term comes from the derivative of the Heavyside function used for time ordering and the zero subscript of $\langle \overline{q}_0 q_0 \rangle$ indicates the contribution to the chiral condensate from a single point, analogous to setting $x$=0 in (1.18) rather than averaging over the whole spacetime volume. The left hand side of (1.84) will vanish when summed over the whole lattice, leaving us with the GMOR relation

$$\langle \overline{q}_0 q_0 \rangle = m_f \chi_{\pi,0} + \Delta \mathcal{J}_5 \tag{1.85}$$

where $\chi_\pi$ is the pion (or pseudoscalar) susceptibility

$$\chi_{\pi,0} \equiv -\frac{2}{4N_c} \sum_x \left\langle \overline{q}_x \gamma_5 \frac{\lambda^a}{2} q_x\ \overline{q}_0 \gamma_5 \frac{\lambda^a}{2} q_0 \right\rangle \tag{1.86}$$

and $\Delta \mathcal{J}_5$ is the mid-plane contribution due to finite $L_s$

$$\Delta \mathcal{J}_5 \equiv -\frac{2}{4N_c} \sum_x \left\langle \mathcal{J}^a_{d+1}(x, L_s/2)\ \overline{q}_0 \gamma_5 \frac{\lambda^a}{2} q_0 \right\rangle. \tag{1.87}$$

As before, the zero subscript $\chi_{\pi,0}$ in (1.86) means this quantity is computed only at a single lattice point, analogous to setting $x$=0 in (1.19).

In the chirally broken phase, both susceptibilities should be dominated in the massless limit by the light Goldstone degrees of freedom localized on the walls. As $\mathcal{J}^a_{d+1}(x, L_s/2)$ is located midway between the two boundaries, its overlap with the boundary states should be exponentially suppressed. So, assuming an infinite lattice volume, we will model $\chi_{\pi,0}$ as

$$\chi_{\pi,0} = \frac{a_{-1}}{m_f + m_{\text{res}}} + a_0 + \mathcal{O}(m_f) \tag{1.88}$$

and $\Delta\mathcal{J}_5$ will also have a pole when $m_f = -m_{\text{res}}$ although we expect that the $c_i$ will be exponentially suppressed in $L_s$

$$\Delta\mathcal{J}_5 = \frac{c_{-1}}{m_f + m_{\text{res}}} + c_0 + \mathcal{O}(m_f). \tag{1.89}$$

Thus, $m_\pi^2 \to 0$ as $m_f \to -m_{\text{res}}$. We also note that the parameters used here are assumed only to be independent of $m_f$ and can vary with $m_0$ and $L_s$ but we imagine performing the following derivation while holding $m_0$ and $L_s$ fixed.

We write the GMOR relation as

$$\frac{\langle \overline{q}_0 q_0 \rangle}{\chi_{\pi,0}} = m_f + \frac{\Delta\mathcal{J}_5}{\chi_{\pi,0}} \tag{1.90}$$

and substitute our parameterizations (1.88) and (1.89) in the right hand side

$$\frac{\langle \overline{q}_0 q_0 \rangle}{\chi_{\pi,0}} = m_f + \frac{c_{-1} + c_0(m_f + m_{\text{res}})}{a_{-1} + a_0(m_f + m_{\text{res}})}. \tag{1.91}$$

As we tune $m_f$ to the pion pole, *i.e.* $m_f \to -m_{\text{res}}$, the left hand side of (1.91) will vanish. On the right hand side, this requires $m_{\text{res}} = c_{-1}/a_{-1}$ which allows us to eliminate $c_{-1}$ as a free parameter in (1.91).

In the continuum identity the slope of $\langle \overline{q}_0 q_0 \rangle / \chi_{\pi,0}$ versus the bare quark mass is always one. However, for domain wall fermions as $m_f \to -m_{\text{res}}$ at fixed $m_0$ and $L_s$

$$\frac{\partial}{\partial m_f}\left(\frac{\langle \overline{q}_0 q_0 \rangle}{\chi_{\pi,0}}\right)\bigg|_{m_f = -m_{\text{res}}, m_0, L_s} = 1 + \frac{c_0 - a_0 m_{\text{res}}}{a_{-1}} \tag{1.92}$$

so the slope is never one except when $c_0 = a_0 m_{\text{res}}$. To clarify this situation, let us eliminate the parameter $c_0$ in favor of $b_0 = c_0 - a_0 m_{\text{res}}$, the parameter which, when

non-zero, indicates the slope of $\langle \overline{q}_0 q_0 \rangle / \chi_{\pi,0}$ is not unity as $m_f \to -m_{\rm res}$. In this new parameterization, we see that (1.89) becomes

$$\Delta \mathcal{J}_5 = m_{\rm res} \chi_{\pi,0} + b_0 \tag{1.93}$$

and the GMOR relation (1.90) becomes implicitly

$$\langle \overline{q}_0 q_0 \rangle = (m_f + m_{\rm res})\, \chi_{\pi,0} + b_0 \tag{1.94}$$

and explicitly

$$\frac{\langle \overline{q}_0 q_0 \rangle}{\chi_{\pi,0}} = (m_f + m_{\rm res}) \left[ 1 + \frac{b_0}{a_{-1} + a_0 \, (m_f + m_{\rm res})} \right]. \tag{1.95}$$

Finally, we recall that the chiral condensate receives contributions from chiral symmetry breaking not just at large distances but from all energy scales up to the lattice cutoff. We should expect that chiral symmetry violations of the GMOR relation due to lattice artifacts will appear in a form that cannot be interpreted as an additional residual mass in the low energy effective Lagrangian. We conjecture that the non-zero $b_0$ is precisely the cumulative contribution due to the chiral symmetry breaking of the heavy modes at the lattice cutoff. As such, we could absorb the heavy contribution into a new definition of the chiral condensate, which we call the "subtracted" chiral condensate

$$\langle \overline{q}_0 q_0 \rangle_{\rm sub} = \langle \overline{q}_0 q_0 \rangle - b_0. \tag{1.96}$$

One potential advantage of including this contribution in the chiral condensate is that it guarantees the slope of the lattice spectral identity will be unity when the spectrum becomes chiral as $m_f \to -m_{\rm res}$ at fixed $m_0$ and $L_s$

$$\frac{\partial}{\partial m_f} \left( \frac{\langle \overline{q}_0 q_0 \rangle_{\rm sub}}{\chi_{\pi,0}} \right) \Bigg|_{m_0, L_s} = 1. \tag{1.97}$$

In chapter 3, we will use the approach of this section to estimate the residual mass for our simulations near the critical temperature of QCD. For a given domain

wall separation, we would like to establish whether the dominant contribution to the effective quark mass comes from the bare input mass, $m_f$, or the residual mixing of the chiral surface states, $m_{\rm res}$. Ideally, to ensure good control over the chiral limit, we would prefer to choose $L_s$ large enough so $m_{\rm res} \ll m_f$. Only then can we be confident that any observed critical behavior, or lack thereof, is a consequence of the chiral symmetry of the QCD Lagrangian.

## 1.6 The QCD finite temperature phase transition

An outstanding success of lattice QCD has been the demonstration of confinement and spontaneously broken chiral symmetry at low temperatures and the existence of a phase transition above some critical temperature, $T_c$. A current goal of lattice theorists is to calculate the physical value for $T_c$, as well as other physically observable consequences of the transition, for comparison with anticipated experimental results from the Relativistic Heavy Ion Collider (RHIC) and other experiments designed to study the thermodynamics of QCD.

In either the quenched limit with infinitely massive quarks or the chiral limit with massless quarks, the finite temperature phase transition is characterized by the behavior of an observable which is not invariant under some symmetry of the action. In the symmetric phase, the observable has a vanishing expectation value because the ground state of the system respects the symmetry of the action. In the broken phase, the observable has, in general, a non-vanishing expectation value because the ground state of the system no longer respects the symmetry. The observable is an order parameter for the transition.

For quenched QCD, the gauge actions (1.23) and (1.25) are globally symmetric under a multiplication of all time-like gauge links originating from a given space-like hyperplane by the same element of the center of the gauge group. For SU($N_c$), the center is $Z_{N_c}$. However, a closed loop of link variables with non-trivial winding around

the temporal direction of the lattice, commonly called a Wilson (or Polyakov) line,

$$W_R(\mathbf{x}) = \frac{1}{\dim(R)} \mathrm{tr} \left[ \prod_{x_4=0}^{L_4-1} U_4(\mathbf{x}, x_4) \right] \tag{1.98}$$

is not invariant under the transformations described above since it involves only one time-like link originating from each space-like hyperplane. The Wilson line observable measures the free energy of a isolated static fermion which couples to the gauge fields in representation $R$ of the gauge group [23, 24, 25, 26]. In the low temperature phase of quenched QCD, the free energy should be infinite and the expectation value of the Wilson line zero. Hence, the Wilson line is the order parameter for the quenched QCD phase transition and the symmetric phase is at low temperature.

Lattice QCD studies have firmly established that the quenched transition is a first order phase transition. This means that a first derivative of the log of the partition function is discontinuous in the transition region. This discontinuity in the energy density is called the latent heat and is the measure of the amount of energy which must be put into the symmetric state to drive it into the broken state.

For QCD with dynamical fermions, the Wilson line is no longer an order parameter because the global $Z_{N_c}$ symmetry of the gauge sector is not a symmetry of the fermion action. The physical interpretation is that once dynamical fermion-antifermion pairs are present in the vacuum, the static fermion can be screened by the vacuum, so the free energy must be finite. In the low temperature phase, since one doesn't expect to see isolated fermions the Wilson line expectation value should still be small. Thus, the Wilson line should undergo rapid evolution through the transition and can serve as an approximate order parameter.

In the limit that the $N_f \geq 2$ dynamical fermions of QCD become massless, the appearance of the $\mathrm{SU}_L(N_f) \otimes \mathrm{SU}_R(N_f)$ global chiral symmetry discussed in sections 1.1 and 1.5 suggests the possibility of a new order parameter for the transition. The chiral condensate (1.18) is not invariant under chiral transformations. So, if the ground state of the system is invariant under chiral transformations then the expectation value for

the chiral condensate must vanish. However, if the chiral symmetry of the action is spontaneously broken then the chiral condensate will, in general, have a non-zero expectation value. Contrary to the quenched theory, the symmetric phase for the massless $N_f \geq 2$ theory occurs at high temperature.

The order of the transition depends strongly on the number of massless quark flavors. For $N_f \geq 3$, renormalization group analysis indicates there are no stable infrared fixed points, a necessary condition for the transition to be second order, *i. e.* the second derivative of the log of the partition function is discontinuous in the critical region [27, 28]. Numerical lattice QCD simulations confirm this conclusion as first order transitions have been observed in the massless limit of QCD with $N_f$=3,4. For $N_f$=2, the order of the transition may be determined by the fate of the anomalously broken $\mathrm{U}_A(1)$ symmetry in the high temperature phase. If the $\mathrm{U}_A(1)$ symmetry remains broken while chiral symmetry is restored, then $N_f$=2 QCD is expected to be in the O(4) universality class, and models in that class have second order phase transitions [29]. However, if $\mathrm{U}_A(1)$ symmetry is effectively restored in the finite temperature phase transition then the universality class changes to $\mathrm{O}(2) \otimes \mathrm{O}(4)$ and, as other models in that class are known to have first order transitions, it is possible that the finite temperature transition for $N_f$=2 QCD will be first order [28, 30, 31].

Earlier attempts to address this question using staggered fermions [32, 33, 34, 35, 36] did not produce conclusive results. While staggered fermions have an exact $\mathrm{U}_V(1) \otimes \mathrm{U}_{A'}(1)$ chiral symmetry, the $\mathrm{U}_{A'}(1)$ is actually an unbroken subgroup of the flavor non-singlet chiral symmetry and not the $\mathrm{U}_A(1)$ of the continuum. At finite lattice spacing, the flavor singlet $\mathrm{U}_A(1)$ is actually broken at the classical level and it becomes quite difficult to disentangle the signal of anomalous symmetry breaking from the explicit breaking due to lattice artifacts.

As $L_s \to \infty$, $\mathrm{U}_A(1)$ is a symmetry of the classical massless domain wall action. The domain wall Dirac operator can have exact zero modes [19] and a well-defined integer index, even for gauge fields at strong coupling. We demonstrated this numer-

ically in earlier studies [37, 38, 39] by observing the effects of fermionic zero modes produced by smooth topological gauge configurations for small bare quark masses and for $L_s \gtrsim 10$. Further, these effects persisted even after the addition of a moderate amount of Gaussian noise to the classical gauge fields. From this we conclude that domain wall fermions are an ideal formulation to study the $U_A(1)$ problem. In preliminary studies [40, 41, 42, 43, 44], we have strong evidence that $U_A(1)$ remains broken in the high temperature phase, but by such a small amount that it may be possible that the breaking is negligible so that the symmetry is effectively restored. It is a primary goal of this work to address whether numerical lattice simulations of $N_f$=2 QCD with domain wall fermions give evidence of a first or second order transition in the massless limit.

In the real world, the fermions of QCD are neither massless nor infinitely massive, so both the Wilson line and the chiral condensate serve only as approximate order parameters. As such, we expect that the values of these observables will undergo a rapid change as we adjust the bare parameters of the theory to move through the transition region. However, the width of the transition region is an important phenomenological number and can be directly computed on the lattice.

In sections 3.2 and 3.3, we will measure the Wilson line and chiral condensate in lattice simulations of $N_f$=2 QCD with two light degenerate flavors of domain wall fermions. We can locate the region of the finite temperature transition by searching for simultaneous rapid changes in both approximate order parameters as we vary the temperature. Once we have located the critical temperature, we will study the behavior of the chiral condensate for small quark masses in the hope that we will see some indication of the order of the phase transition in the chiral limit.

# Chapter 2

# Numerical implementation of QCD with domain wall fermions

## 2.1 General considerations

A naive approach to numerical simulation of lattice QCD follows from our discussion in sections 1.1 and 1.2, particularly equations (1.10) and (1.22), regarding the computation of expectation values. To evaluate the lattice partition function on a computer, we approximate the continuous multidimensional path integral over an infinite lattice volume as a sum over finite volume lattice configurations with a finite precision representation of real numbers

$$Z \to \sum_{\{U\}} e^{-S(U)}, \qquad \langle \mathcal{O}(U) \rangle \to \frac{1}{Z} \sum_{\{U\}} \mathcal{O}(U) e^{-S(U)}. \tag{2.1}$$

Each $U$ is one possible lattice configuration and $\{U\}$ is the set of all representable configurations. After fixing the lattice size and precision, only a countable number of configurations can be represented in the memory of a computer. So, to evaluate the expectation value in (2.1), it is possible to program a computer to generate, one by one, each configuration $U$ that can be represented, compute the observable $\mathcal{O}(U)$

and the Boltzmann weight $e^{-S(U)}$ on each configuration and do the weighted average indicated.

To see this approach as completely intractable, consider a simple Ising model: on each lattice site is a single degree of freedom which can take on one of two possible values, which we can represent as a single bit in the memory of our computer. If $V$ is the total number of sites in a given lattice volume, then the number of representable configurations that our program must evaluate is $2^V$. The time required to compute any expectation value grows exponentially in the size of the configuration. For QCD, the only difference is the counting of representable degrees of freedom per lattice site once the number of bits of memory per lattice site is fixed. So, this method is intractable for all but the smallest lattice volumes.

We recall from the statistical mechanics of systems with many degrees of freedom, the Boltzmann distribution in configuration space is strongly peaked around the minimum of the action. This implies that the naive method above is incredibly inefficient since most of the configurations generated will have vanishingly small weight for expectation values. To surmount this problem, we use *importance sampling*, which creates a sample ensemble of configurations drawn from the set of all representable configurations with a probability given by the Boltzmann weight. Configurations with large weights will appear more frequently in our sample. The number of configurations in the sample should be large enough that expectation values computed on the sample agree, within a given precision, with ones computed on the full set. A computer program could generate configurations at random and compute the weight and expectation values. However, this approach is no better than the naive method above since most configurations will be very unlikely to appear in a sample ensemble. So, an importance sampling method should provide us with an algorithm which only generates configurations with a good chance to be added to the sample.

A classic example of an importance sampling method is the Metropolis algorithm. The algorithm has two parts: the *update process* and the *acceptance test*. The initial

condition for the algorithm is to start at any point in the configuration space, let's call it $U_1$. The algorithm then starts by computing the Boltzmann weight, $w_1$, of the initial configuration and adding it to the sample ensemble. Next, we use the update process to generate a second configuration with known probability $P_u(U_2 \leftarrow U_1)$ and compute its weight, $w_2$. Then we use the acceptance test to decide if the second configuration should be accepted into the sample with probability $P_a(U_2 \leftarrow U_1)$:

$$P_a(U_2 \leftarrow U_1) = \min\left\{1, \frac{P_u(U_1 \leftarrow U_2)\, w_2}{P_u(U_2 \leftarrow U_1)\, w_1}\right\} \tag{2.2}$$

The total probability that the second configuration is accepted given the first configuration is $P(U_2 \leftarrow U_1) = P_a(U_2 \leftarrow U_1)\, P_u(U_2 \leftarrow U_1)$. We then iterate the algorithm by applying the update process and acceptance test to the last configuration accepted until the sample ensemble is sufficiently large.

Two important issues must be addressed when designing update processes for the Metropolis algorithm. The first is whether the algorithm can eventually construct a sample ensemble and the second is how efficiently the algorithm can construct the ensemble. The first issue can be resolved if we establish two properties. The property called *detailed balance*, which guarantees that the Boltzmann distribution of our sample ensemble will converge to the distribution of the full set, requires

$$P(U_j \leftarrow U_i)\, w_i = P(U_i \leftarrow U_j)\, w_j. \tag{2.3}$$

From the preceding paragraph, it is straightforward to verify that the Metropolis algorithm satisfies detailed balance. The second property, called *ergodicity*, requires that the update process of the Metropolis algorithm can reach any point in the configuration space with finite probability in a finite number of steps. This property ensures that no important regions of configuration space are left unsampled provided the algorithm is run long enough. However, it is typically very difficult to determine analytically the efficiency of a given algorithm to construct an ergodic ensemble. In such cases, one attempts to address this issue through numerical studies.

For pure gauge theories on the lattice, a typical update process is to choose a single gauge link, propose a change to that link and compute the difference in the action, $\Delta S$, between the two configurations. Since the gauge action is local, $\Delta S$ is inexpensive to compute. However, to maintain efficiency, some care must be taken in the update process to make sure that the proposed change to the single link is still sufficiently small to allow a reasonable chance of passing the acceptance test. Performing a Metropolis step at each link in the lattice once in succession is commonly called a *sweep*. One potential disadvantage of this approach is that two configurations in the update sequence separated by only a few sweeps will still be related, or "nearby" in configuration space. So, many sweeps are typically required to evolve the sequence between "distant" regions of configuration space.

As discussed in section 1.4, in lattice QCD with dynamical fermions, the Grassmann degrees of freedom are integrated out analytically, leaving a partition function expressed in only in terms of gauge degrees of freedom

$$Z = \int [\mathcal{D}U]\, e^{-S_G + \mathrm{Tr}\log M_F - \mathrm{Tr}\log M_{PV}} \tag{2.4}$$

or, equivalently, in terms of gauge and pseudofermion degrees of freedom

$$Z = \int [\mathcal{D}U] \left[\mathcal{D}\Phi_F^\dagger\right] [\mathcal{D}\Phi_F] \left[\mathcal{D}\Phi_{PV}^\dagger\right] [\mathcal{D}\Phi_{PV}]\, e^{-S_G - \Phi_F^\dagger M_F^{-1}\Phi_F - \Phi_{PV}^\dagger M_{PV}\Phi_{PV}}. \tag{2.5}$$

Local update processes will no longer be efficient in either case since the calculation of $\Delta S_{\text{eff}}$ is no longer local. While solving the sparse linear system $M_F\chi_F = \Phi_F$ is not as computationally demanding as the full diagonalization normally required to compute $\mathrm{Tr}\log M$, both are essentially non-local computations. So, a successful fermionic update process should simultaneously update a large number of degrees of freedom for a given calculation of the solution to $M_F\chi_F = \Phi_F$ without a corresponding large change in the action.

One popular algorithm that accomplishes this is the hybrid Monte Carlo algorithm. The strategy is to treat the gauge degrees of freedom as generalized coordinates

in a Hamiltonian framework of one higher dimension (not to be confused with the extra dimension of domain wall fermions). We introduce conjugate momenta $H_\mu(x)$, which appear in the extended path integral as a trivial bosonic field

$$Z = \int [\mathcal{D}U]\,[\mathcal{D}H]\,e^{-\mathcal{H}} = \int [\mathcal{D}U]\,e^{-S_{\text{eff}}} \tag{2.6}$$

where the Hamiltonian

$$\mathcal{H} = S_{\text{eff}} + \sum_{x,\mu} \text{tr}\left[\frac{1}{2}H_\mu(x)H_\mu(x)\right] \tag{2.7}$$

now serves as the Boltzmann weight for the extended system $(U, H)$. The update process for the momenta merely requires the generation of a Gaussian distributed field, which is always accepted. Hamilton's equations of motion are then used to evolve the system along the classical trajectory. Provided the computational cost of the classical evolution is not prohibitive, the result in a simultaneous update of all the degrees of freedom between calculations of the (hopefully small) change in the Boltzmann weight.

## 2.2 The hybrid Monte Carlo algorithm

The *hybrid Monte Carlo* (HMC) algorithm combines a non-local update process called *hybrid molecular dynamics* (HMD) with the Metropolis acceptance test described in section 2.1 [45]. The full path integral is rewritten in terms of the pseudofermionic fields $\Phi_F$ and $\Phi_{PV}$ as in (2.5). The algorithm starts with the generation of Gaussian distributed momenta $H_\mu(x)$ and the computation of their contribution to the initial Hamiltonian. For the fermionic and Pauli-Villars contributions, pseudofermion fields $\Phi_F$ and $\Phi_{PV}$ are generated for the gauge field configuration using a bosonic heat bath algorithm described below. Then, using Hamilton's equations of motion, the extended system $(U, H)$ is evolved in the presence of the forces due to the fixed pseudofermion background along the classical trajectory for some finite interval of

the microcanonical evolution parameter, $\tau$. Finally, the Hamiltonian is recomputed at the end of the trajectory and the change between endpoints $\Delta\mathcal{H}$ is used as input to a Metropolis acceptance test, which makes the algorithm exact even though the numerical integration only approximately conserves the Hamiltonian. The result is a simultaneous update of all dynamical degrees of freedom between each computation of the Boltzmann weight.

For lattice QCD, after formally integrating out the fermionic (and pseudofermionic) variables, the only degrees of freedom are the gauge fields. The conjugate momenta give the microcanonical evolution of the gauge fields through Hamilton's first equation of motion

$$\frac{\mathrm{d}}{\mathrm{d}\tau}U_\mu(x) = iH_\mu(x)U_\mu(x), \qquad \text{(no sum over } \mu\text{)}. \tag{2.8}$$

The restriction that the gauge links $U_\mu(x)$ remain in the gauge group $\mathrm{SU}(N_c)$ during the evolution constrains the momenta $H_\mu(x)$ to be elements of the Lie algebra of the gauge group, hence traceless and Hermitian. Expectation values will be unaffected by the shift in normalization of the partition function (2.6) due to the inclusion of the Gaussian distributed $H_\mu(x)$.

Hamilton's second equation of motion is derived from the requirement that the Hamiltonian is a constant of the motion

$$\sum_{x,\mu} \mathrm{tr}\left[H_\mu(x)\frac{\mathrm{d}H_\mu(x)}{\mathrm{d}\tau}\right] = -\frac{\mathrm{d}S_{\mathrm{eff}}}{\mathrm{d}\tau}. \tag{2.9}$$

In section 2.4, we will explicitly compute $\mathrm{d}S_{\mathrm{eff}}/\mathrm{d}\tau$ using (2.8) and show it can be written as

$$\frac{\mathrm{d}S_{\mathrm{eff}}}{\mathrm{d}\tau} = \sum_{x,\mu} \mathrm{tr}\left[iH_\mu(x)F_\mu(x)\right] \tag{2.10}$$

where $F_\mu(x)$ is the called the *HMD force*. The restriction that the momenta $H_\mu(x)$ remain in the Lie algebra of the gauge group during the evolution means that only the traceless anti-Hermitian part of the force may influence the momenta. Putting

(2.9) and (2.10) together gives us Hamilton's second equation

$$i\frac{\mathrm{d}H_\mu(x)}{\mathrm{d}\tau} = [F_\mu(x)]_{\mathrm{TA}} \tag{2.11}$$

where the subscript TA means to take the traceless anti-Hermitian part. In section 2.4, we will show that each calculation of the fermionic force will require solving the sparse linear system $M_F^\dagger M_F \chi_F = \Phi_F$.

The HMD update process starts with the initial gauge configuration $U_i$ and as mentioned above, the initial momenta $H_i$ and pseudofermions are generated. This completely defines the initial state of the dynamical variables $(U_i, H_i)$ in the background environment of $\Phi_F$ and $\Phi_{PV}$. The gauge and momentum contributions to the initial Hamiltonian $\mathcal{H}_i$ are computed directly. The pseudofermions are produced by a bosonic heat bath, which consists of generating random complex fields $R_F$ and $R_{PV}$ with a Gaussian distribution proportional to $\exp(-R^*R)$. Defining the pseudofermion fields

$$\Phi_F = M_F^\dagger R_F, \qquad \Phi_{PV} = \left(M_{PV}^{-1}\right)^\dagger R_{PV} \tag{2.12}$$

will give probability distributions proportional to $\exp\left[-\Phi_F \left(M_F^\dagger M_F\right)^{-1} \Phi_F\right]$ and $\exp\left(-\Phi_{PV} M_{PV}^\dagger M_{PV} \Phi_{PV}\right)$. Using the Hermitian matrices $M^\dagger M$ allow for the use of efficient algorithms for solving sparse linear systems. For both Wilson and domain wall fermions, $\det M^\dagger M = \det M^2$ so the algorithm will generate distributions for two degenerate flavors of fermions. Note that the computation of $\Phi_F$ is local whereas the computation of $\Phi_{PV}$ first requires solving the sparse linear system $\left(M_{PV}^\dagger M_{PV}\right)^{-1} \Phi'_{PV} = R_{PV}$ and then computing $\Phi_{PV} = M_{PV}\Phi'_{PV}$. The fermionic and Pauli-Villars contributions to the initial Hamiltonian are then computed using the pseudofermion fields.

The next step in the update process is to evolve $(U_i, H_i)$ by integrating both of Hamilton's equations simultaneously over some finite interval of $[\tau_i, \tau_{i+1}]$ to arrive deterministically at the final state $(U_{i+1}, H_{i+1}) \leftarrow (U_i, H_i)$, all the while holding fixed the pseudofermion fields. To satisfy detailed balance, the evolution must be

*reversible*: starting from the endpoint of the classical trajectory with the momenta reversed, $(U_{i+1}, -H_{i+1})$, and integrating over the interval $[\tau_{i+1}, \tau_i]$ returns us to the starting point, $(U_i, -H_i) \leftarrow (U_{i+1}, -H_{i+1})$. While a continuous trajectory will be trivially reversible, on the computer care must be taken to ensure that integration using a finite difference approximation is also reversible.

For the simulations in chapter 3, the reversible finite difference approximation we used was the *leap frog* method. We choose the trajectory to start at $\tau = 0$ and end at a fixed $\tau$ and divide the interval into $N$ steps of equal length step size $\Delta\tau$. To start the leap frog, we evolve the momenta one half time step using

$$iH_\mu(x, \Delta\tau/2) = iH_\mu(x, 0) + i\frac{\mathrm{d}H_\mu(x,0)}{\mathrm{d}\tau}\frac{\Delta\tau}{2} + \mathcal{O}(\Delta\tau^2). \tag{2.13}$$

We then alternate evolving the gauge field a single time step

$$U_\mu(x, \tau + \Delta\tau) = e^{iH_\mu(x,\tau+\Delta\tau/2)\Delta\tau}U_\mu(x,\tau) + \mathcal{O}(\Delta\tau^3) \tag{2.14}$$

and the momenta a single time step

$$iH_\mu(x, \tau + \Delta\tau/2) = iH_\mu(x, \tau - \Delta\tau/2) + i\frac{\mathrm{d}H_\mu(x,\tau)}{\mathrm{d}\tau}\Delta\tau + \mathcal{O}(\Delta\tau^3). \tag{2.15}$$

We finish the trajectory after evolving the gauge field $N$ times with a final half step evolution of the momenta. We emphasize that each time we evolve the gauge fields we must solve again the linear system $M_F^\dagger M_F \chi_F = \Phi_F$ and recompute the fermionic force needed to evolve the momenta (see section 2.4).

To ensure ergodicity, the number of steps must be of order $\Delta\tau^{-1}$, so the difference between the initial and final Hamiltonians, $\Delta\mathcal{H}$, will be of order $\Delta\tau^2$. $\Delta\mathcal{H}$ is then used in a Metropolis acceptance test at the end of the HMD trajectory to compensate for finite $\Delta\tau$ errors. As the Hamiltonian is an extensive quantity, the step size must be decreased as the volume is increased to maintain a given acceptance. After the acceptance test, the algorithm continues by generating new momenta and pseudofermion fields and evolving along a new classical HMD trajectory. So, as

promised, the HMC algorithm can make simultaneous acceptable changes to all the gauge degrees of freedom and compute changes to the Boltzmann weight each time the fermionic linear system is solved. However, as the lattice volume grows, more solutions of the fermionic system are required to produce independent configurations.

## 2.3 The preconditioned domain wall action

Because of the central role of algorithms for solving sparse linear systems in the evolution of fermionic configurations, we will reformulate the domain wall fermion matrix into a form better suited for more efficient computation. In general, the cost of solving linear systems is proportional to the ratio of the largest eigenvalue $\lambda_{\max}$ to the smallest eigenvalue $\lambda_{\min}$ of the matrix, called the *condition number*. A technique, called *preconditioning*, seeks to transform the given matrix (usually at some cost) into a new matrix with a smaller condition number. If the savings in solving the new system outweigh the cost of transforming the results back into the old system, then the preconditioner is successful. For a general discussion on the importance of preconditioning when solving linear systems, see Golub and Van Loan [46]. For fermionic evolution algorithms, if the preconditioning transformation preserves the determinant, then the cost of the transformation is irrelevant because we can choose to work only with the new system. In the case of the HMC algorithm, preconditioning will help reduce the computational cost by at least a factor of two.

The Wilson fermion matrix (1.31) contains entries which connect only nearest neighbor sites. We introduce a labeling scheme where a lattice site is labeled even if all its nearest neighbor sites are labeled odd and vice-versa. For example, if $\sum_{\mu=1}^{4} x_\mu \mathrm{mod} 2 = 0$ on a given site we label it even ($e$), otherwise we label it odd ($o$). We then rearrange the components of the fermion vectors to list odd ones first

and write the matrix in block form

$$M^{(W)} = \begin{pmatrix} \mathbb{1}_{oo} & -\kappa D_{oe} \\ -\kappa D_{eo} & \mathbb{1}_{ee} \end{pmatrix}. \tag{2.16}$$

Note that we have rescaled the fermion fields by $\sqrt{\kappa}$ where

$$\kappa = \frac{1}{2(m_0 + dr)}, \tag{2.17}$$

which makes the on-diagonal blocks the identity.

DeGrand [47, 48] proposed a preconditioning technique that replaces the Wilson fermion matrix $M^{(W)}$ by a preconditioned matrix $\widetilde{M}^{(W)}$ which preserves the determinant $\det M^{(W)} = \det \widetilde{M}^{(W)}$. He noted that $M^{(W)}$ could be decomposed in block form

$$M^{(W)} = U \widetilde{M}^{(W)} L \tag{2.18}$$

by choosing $U$ and $L$ to be the upper and lower block-triangular parts of $M^{(W)}$. Then the block-diagonal $\widetilde{M}^{(W)}$ is

$$\widetilde{M}^{(W)} = U^{-1} M^{(W)} L^{-1} = \begin{pmatrix} \mathbb{1}_{oo} - \kappa^2 D_{oe} D_{eo} & 0_{oe} \\ 0_{eo} & \mathbb{1}_{ee} \end{pmatrix}. \tag{2.19}$$

We can see that $\det U = \det L = 1$ so the transformation preserves the determinant.

To see that this odd-even technique reduces the condition number, we consider an eigenvalue of $D$, the off-diagonal part of (2.16), where $\lambda_D = 1/(\kappa + \epsilon)$. The corresponding eigenvalue of $M^{(W)}$ is $\lambda_M = \epsilon/(\kappa + \epsilon)$. We can choose $\epsilon \ll \kappa$ so $\lambda_{\min}(M) = \lambda_M \approx \epsilon/\kappa$. For each $\lambda_D$, there is a corresponding eigenvalue $\lambda_D^2$ of the block matrix $D_{oe} D_{eo}$ of (2.19). So, the smallest eigenvalue of the preconditioned matrix is $\lambda_{\min}(\widetilde{M}) = 1 - \kappa^2/(\kappa+\epsilon)^2 \approx 2\epsilon/\kappa$ and the condition number is approximately reduced by half.

One additional advantage of this preconditioning choice is the decoupling of even site fermion degrees of freedom which allows us to integrate them out trivially, adding an irrelevant factor to the overall normalization of the partition function. This reduces

the storage requirements when implementing the action on a computer, since only half of the original components contribute.

In chapter 1, we relied on our experience with Wilson fermions to guide us in constructing and interpreting the physics of domain wall fermions. Here, we can rely on that same experience to guide us in rewriting the domain wall fermion matrix in a form better suited for solving linear systems. The domain wall fermion matrix $D^{\|}_{x,x'}$ in (1.42) will have the same structure as $M^{(W)}$ in (2.16) when the fermion fields are rescaled by $\sqrt{\kappa_5}$ where

$$\kappa_5 = \frac{1}{2\left(rd + 1 - m_0\right)}. \tag{2.20}$$

Before we continue, it is useful to note that the odd-even block matrices on the $d+1$ dimensional lattice will still have a remaining Wilson-like odd-even substructure on each $d$ dimensional plane of fixed $s$ coordinate, which follows from (1.38). Since Wilson fermions have been studied by the lattice community for a long time, it is rather straight forward to implement an efficient Wilson inverter and verify its implementation against the published results of many different groups. So, reusing the same code to apply these Wilson $D_{oe}$ matrices to $d$ dimensional sub-vectors in the domain wall context will require arranging those components in a separate $d$ dimensional odd-even storage order. As a schematic, if the subscripts $o, e$ indicate odd and even blocks on the $d$ dimensional lattice and $O, E$ indicate odd and even blocks on the $d+1$ dimensional lattice then a useful arrangement of vector components is

$$\Psi_{x,s} = \begin{pmatrix} \Psi_O \\ \Psi_E \end{pmatrix} = \begin{pmatrix} \begin{pmatrix} \psi_{o,s=0} \\ \psi_{e,s=1} \\ \vdots \end{pmatrix} \\ \begin{pmatrix} \psi_{e,s=0} \\ \psi_{o,s=1} \\ \vdots \end{pmatrix} \end{pmatrix}. \tag{2.21}$$

With vector components written in this way, $M^{(dwf)}_{x,s;x',s'}$ of (1.41) can be written in

block form

$$M^{(dwf)} = \begin{pmatrix} \mathbb{1}_{OO} & -\kappa_5 D_{OE} \\ -\kappa_5 D_{EO} & \mathbb{1}_{EE} \end{pmatrix}. \tag{2.22}$$

In analogy with (2.19), the preconditioned domain wall fermion matrix, in block diagonal form, is

$$\widetilde{M}^{(\mathrm{dwf})} = U^{-1} M^{(\mathrm{dwf})} L^{-1} = \begin{pmatrix} \mathbb{1}_{OO} - \kappa_5^2 D_{OE} D_{EO} & 0_{OE} \\ 0_{EO} & \mathbb{1}_{EE} \end{pmatrix}. \tag{2.23}$$

It is straightforward to devise a scheme to test the implementation of preconditioning. After implementing the action of $D_{OE}$ and $D_{EO}$ on even and odd vectors, one can simply verify the following is true:

$$U\widetilde{M}^{(\mathrm{dwf})} L\Psi = M^{(dwf)}\Psi. \tag{2.24}$$

for arbitrary $\Psi$. The tests we have performed indicate preconditioning was implemented within machine precision. For the numerical simulations we present in chapter 3, the preconditioned domain wall fermion linear solver typically converged in half as many iterations as the unpreconditioned one.

## 2.4 The hybrid molecular dynamics force term

In section 2.2 we discussed aspects of the HMC algorithm that did not depend on the explicit form of the action. Here we present an explicit derivation of the HMD force $F_\mu(x)$, as defined in (2.10), for which we need to compute the derivatives with respect to the microcanonical evolution parameter $\tau$ of all the terms in the action. We will consider the Wilson plaquette gauge action, (1.23), the plaquette plus rectangle gauge action (1.25) and the preconditioned domain wall action described in section 2.3, including the Pauli-Villars term. The gauge action contributions to the force are well known [45] and are included here only for completeness.

To determine the gauge contribution to the force, we must compute the derivative of the gauge action, which for either action can be written

$$\frac{\mathrm{d}S_G}{\mathrm{d}\tau} = -\frac{\beta}{2N_c}\sum_{x,\mu}\mathrm{tr}\left\{\left[\frac{\mathrm{d}}{\mathrm{d}\tau}U_\mu(x)\right]V_\mu(x) + V_\mu^\dagger(x)\left[\frac{\mathrm{d}}{\mathrm{d}\tau}U_\mu^\dagger(x)\right]\right\}. \tag{2.25}$$

The $V_\mu(x)$ are called staples and are made of sums of $\mathrm{SU}(N_c)$ matrices. We write the staple field as the weighted sum of the plaquette and rectangle staple fields: $V_\mu(x) = c_0 V_\mu^{(P)}(x) + c_1 V_\mu^{(R)}(x)$. For the plaquette field defined in (1.24) the corresponding plaquette staple field is

$$\begin{aligned} V_\mu^{(P)}(x) = \sum_{\nu\neq\mu} \quad & \big[U_\nu(x+\hat{\mu})U_\mu^\dagger(x+\hat{\nu})U_\nu^\dagger(x) \\ & + U_\nu^\dagger(x+\hat{\mu}-\hat{\nu})U_\mu^\dagger(x-\hat{\nu})U_\nu(x-\hat{\nu})\big]. \end{aligned} \tag{2.26}$$

For the rectangle field defined in (1.26) the corresponding rectangle staple field is

$$\begin{aligned} V_\mu^{(R)}(x) = \sum_{\nu\neq\mu} \quad & \big[U_\mu(x+\hat{\mu})U_\nu(x+2\hat{\mu})U_\mu^\dagger(x+\hat{\mu}+\hat{\nu})U_\mu^\dagger(x+\hat{\nu})U_\nu^\dagger(x) \\ & + U_\mu(x+\hat{\mu})U_\nu^\dagger(x+2\hat{\mu}-\hat{\nu})U_\mu^\dagger(x+\hat{\mu}-\hat{\nu})U_\mu^\dagger(x-\hat{\nu})U_\nu(x-\hat{\nu}) \\ & + U_\nu(x+\hat{\mu})U_\nu(x+\hat{\mu}+\hat{\nu})U_\mu^\dagger(x+2\hat{\nu})U_\nu^\dagger(x+\hat{\nu})U_\nu^\dagger(x) \\ & + U_\nu^\dagger(x+\hat{\mu}-\hat{\nu})U_\nu^\dagger(x+\hat{\mu}-2\hat{\nu})U_\mu^\dagger(x-2\hat{\nu})U_\nu(x-2\hat{\nu})U_\nu(x-\hat{\nu}) \\ & + U_\nu(x+\hat{\mu})U_\mu^\dagger(x+\hat{\nu})U_\mu^\dagger(x-\hat{\mu}+\hat{\nu})U_\nu^\dagger(x-\hat{\mu})U_\mu(x-\hat{\mu}) \\ & + U_\nu^\dagger(x+\hat{\mu}-\hat{\nu})U_\mu^\dagger(x-\hat{\nu})U_\mu^\dagger(x-\hat{\mu}-\hat{\nu})U_\nu(x-\hat{\mu}-\hat{\nu})U_\mu(x-\hat{\mu})\big]. \end{aligned} \tag{2.27}$$

The expression (2.25) is valid for either gauge action considered, as the plaquette action result is given by setting $c_1 = 0$.

To identify $F_\mu^{(G)}(x)$, whose traceless anti-Hermitian part will be the pure gauge contribution to the HMD force, we substitute Hamilton's first equation of motion (2.8) into the derivative of the gauge action (2.25)

$$\frac{\mathrm{d}S_G}{\mathrm{d}\tau} = -\frac{\beta}{2N_c}\sum_{x,\mu}\mathrm{tr}\left\{iH_\mu(x)\left[U_\mu(x)V_\mu(x) - V_\mu^\dagger(x)U_\mu^\dagger(x)\right]\right\}. \tag{2.28}$$

By comparing this relation with Hamilton's second equation of motion in (2.10) and (2.11), we choose the $F_\mu^{(G)}$ to implement in our numerical simulations to be

$$F_\mu^{(G)} = -\frac{\beta}{N_c} U_\mu(x) V_\mu(x), \tag{2.29}$$

which has the same traceless, anti-Hermitian part as the expression in square brackets above. We will make similar simplifying choices for the numerical implementation of the other HMD forces.

It will be convenient as we compute the domain wall fermion force term to express the result at each step as two terms related by Hermitian conjugation. This will be easier if we define

$$g(\pm\mu)_{x,s;x',s'} \equiv (1 \mp \gamma_\mu)\delta_{x\pm\hat{\mu},x'}\delta_{s,s'} \tag{2.30}$$

and

$$G_{x,s;x',s'} = \left[1 - (1+m_f)\delta_{0,s'}\right] P_+ \delta_{x,x'}\delta_{s+1,s'} + \sum_\mu g(+\mu)_{x,s;x',s'} U_\mu(x) \tag{2.31}$$

then we can write the preconditioned domain wall fermion matrix which acts only on odd sites as

$$\widetilde{M} = 1_{OO} - \kappa_5^2 D_{OE} D_{EO} \tag{2.32}$$

where

$$D_{x,s;x',s'} = G_{x,s;x',s'} + \gamma_5 \mathcal{R}_{s,s''} G^\dagger_{x,s'';x',s'''} \gamma_5 \mathcal{R}_{s''',s'} \tag{2.33}$$

and $\mathcal{R}_{s,s'} = \delta_{s,L_s-1-s'}$ is the reflection operator along the extra direction. Now, it is easy to verify the Hermiticity relations $D^\dagger = \gamma_5 \mathcal{R} D \gamma_5 \mathcal{R}$ and $\widetilde{M}^\dagger = \gamma_5 \mathcal{R} \widetilde{M} \gamma_5 \mathcal{R}$.

As with the gauge part, we must compute the derivatives with respect to micro-canonical time $\tau$ of the fermion and Pauli-Villars parts of the domain wall action, both expressed in terms of pseudofermions. At first, we work with only the fermionic part, $S_F$, of the domain wall action so we suppress the $F$ and $PV$ subscripts used in sections 2.1 and 2.2 until later in this section when we consider the Pauli-Villars part. An efficient iterative method is used to solve $\widetilde{M}^\dagger \widetilde{M} \chi = \Phi$, in our case based on

the conjugate gradient algorithm [49, 46]. The derivative of $S_F$ can then be written in terms of the solution $\chi$ as

$$\frac{\mathrm{d}S_F}{\mathrm{d}\tau} = -\chi^\dagger \left[\frac{\mathrm{d}}{\mathrm{d}\tau}\left(\widetilde{M}^\dagger \widetilde{M}\right)\right]\chi. \tag{2.34}$$

Using (2.33), the derivative of $\widetilde{M}$ can be written

$$\frac{\mathrm{d}\widetilde{M}}{\mathrm{d}\tau} = -\kappa_5^2 \left[D_{OE}\frac{\mathrm{d}G_{EO}}{\mathrm{d}\tau} + \frac{\mathrm{d}G_{OE}}{\mathrm{d}\tau}D_{EO} + D_{OE}\gamma_5\mathcal{R}\frac{\mathrm{d}G_{EO}^\dagger}{\mathrm{d}\tau}\gamma_5\mathcal{R} + \gamma_5\mathcal{R}\frac{\mathrm{d}G_{OE}^\dagger}{\mathrm{d}\tau}\gamma_5\mathcal{R}D_{EO}\right]. \tag{2.35}$$

If we define another quantity

$$K \equiv -\kappa_5^2\left[D_{OE}\frac{\mathrm{d}G_{EO}}{\mathrm{d}\tau} + \frac{\mathrm{d}G_{OE}}{\mathrm{d}\tau}D_{EO}\right], \tag{2.36}$$

then the derivative (2.35) can be rewritten

$$\frac{\mathrm{d}\widetilde{M}}{\mathrm{d}\tau} = K + \gamma_5\mathcal{R}K^\dagger\gamma_5\mathcal{R} \tag{2.37}$$

after using the Hermiticity relations and noting $(\gamma_5\mathcal{R})^2 = \mathbb{1}$. From here, it is not difficult to show that

$$\frac{\mathrm{d}S_F}{\mathrm{d}\tau} = -\chi^\dagger\left[\left(\gamma_5\mathcal{R}K\gamma_5\mathcal{R}\widetilde{M} + \gamma_5\mathcal{R}\widetilde{M}\gamma_5\mathcal{R}K\right) + \text{h.c.}\right]\chi, \tag{2.38}$$

accomplishing our goal of expressing the derivative as two terms related by Hermitian conjugation.

The next step is to arrange the derivative calculations using (2.8) so that $iH_\mu(x)$ appears on the left. We start again from (2.31)

$$\frac{\mathrm{d}}{\mathrm{d}\tau}G_{x,s;x',s'} = \sum_\mu iH_\mu(x)g(+\mu)_{x,s;x',s'}U_\mu(x). \tag{2.39}$$

While $G$ depends explicitly on the bare mass $m_f$, the derivative does not as there are no gauge fields in the extra direction. This result is then substituted into (2.36), recalling that $K$ is defined only when both sets of indices are odd

$$\begin{aligned} K_{x,s;x',s'} &= -\kappa_5^2\sum_\mu \left[D_{x,s;x'',s''}iH_\mu(x'')g(+\mu)_{x'',s'';x',s'}U_\mu(x'')\right. \\ &\quad \left. + iH_\mu(x)g(+\mu)_{x,s;x'',s''}U_\mu(x)D_{x'',s'';x',s'}\right]. \end{aligned} \tag{2.40}$$

Finally, we substitute into the derivative of the fermionic action, and use the invariance of the trace under cyclic permutation to move the conjugate momenta to the left

$$\begin{aligned}\frac{\mathrm{d}S_F}{\mathrm{d}\tau} &= +\kappa_5^2 \sum_{x,\mu} \mathrm{tr}_{\mathrm{color}}(iH(x,\mu) \\ &\quad \times \{U_\mu(x)\ \mathrm{tr}_{s,\mathrm{spin}} \quad \left[g(+\mu)\left(\chi\chi^\dagger \widetilde{M}^\dagger D + D\chi\chi^\dagger \widetilde{M}^\dagger\right)\right. \\ &\qquad\qquad \left. + g^\dagger(-\mu)\left(\widetilde{M}\chi\chi^\dagger D^\dagger + D^\dagger \widetilde{M}\chi\chi^\dagger\right)\right] \\ &\quad - \mathrm{h.c.}\}).\end{aligned} \tag{2.41}$$

As with the pure gauge contribution, we compare this relation with Hamilton's second equation in (2.10) and (2.11) and choose $F_\mu^{(F)}(x)$ to have the same traceless, anti-Hermitian part as the expression in the curly braces but in a form convenient for numerical simulation.

We construct some vectors which are defined on half of the sites of the lattice

$$\rho_E = \quad D_{EO}\chi_O \tag{2.42}$$

$$\psi_O = \quad -\kappa_5^2 \widetilde{M}_{OO}\chi_O \tag{2.43}$$

$$\sigma_E = \quad D_{EO}^\dagger \psi_O \quad = -\kappa_5^2 D_{EO}^\dagger \widetilde{M}_{OO}\chi_O. \tag{2.44}$$

Now we can write the fermionic contribution to the force

$$F_\mu^{(F)}(x) = -2U_\mu(x)\ \mathrm{tr}_{s,\mathrm{spin}}\left[g(+\mu)\left(\chi\sigma^\dagger + \rho\psi^\dagger\right) + g^\dagger(-\mu)\left(\psi\rho^\dagger + \sigma\chi^\dagger\right)\right]. \tag{2.45}$$

We can make one further simplification by defining two vectors which extend over the whole lattice

$$v = \begin{pmatrix} \rho_E \\ \chi_O \end{pmatrix} \qquad w = \begin{pmatrix} \sigma_E \\ \psi_O \end{pmatrix}. \tag{2.46}$$

Finally, in terms of the vectors $v$ and $w$

$$F_\mu^{(F)}(x) = -2U_\mu(x) \sum_s \mathrm{tr}_{\mathrm{spin}}\left[(1-\gamma_\mu)v_{x+\hat{\mu},s} w_{x,s}^\dagger + (1+\gamma_\mu) w_{x+\hat{\mu},s} v_{x,s}^\dagger\right]. \tag{2.47}$$

With the absence of gauge fields in the $s$-direction, it is not surprising that this fermionic force is identical in form to the force due to $L_s$ flavors of Wilson fermions.

This implies that all of the special properties of domain wall fermions, at this level, are encoded at the start when finding the solution $\chi_O$ of the fermionic system.

The derivative of the Pauli-Villars part of the domain wall action is

$$\frac{\mathrm{d}S_{PV}}{\mathrm{d}\tau} = \Phi_{PV}^{\dagger}\left[\frac{\mathrm{d}}{\mathrm{d}\tau}\left(\widetilde{M}_{PV}^{\dagger}\widetilde{M}_{PV}\right)\right]\Phi_{PV}. \tag{2.48}$$

Note the crucial difference in sign relative to the derivative of the fermion action (2.34). The construction of the Pauli-Villars contribution to the HMD force mirrors the construction for the fermionic part provided we set the solution $\chi_{PV}$ to be the pseudofermion field generated by the heat bath, $\chi_{PV} = \Phi_{PV}$, set $m_f$=1 and keep track of the overall change in sign. Using $\chi_{PV}$ in place of $\chi$ we get

$$F_{\mu}^{(PV)}(x) = -\left.F_{\mu}^{(F)}(x)\right|_{m_f=1,\chi=\chi_{PV}}. \tag{2.49}$$

Now that all three force contributions are known, (2.11) can be written

$$i\frac{\mathrm{d}}{\mathrm{d}\tau}H_{\mu}(x) = \left[F_{\mu}^{(G)}(x) + F_{\mu}^{(F)}(x) + F_{\mu}^{PV}(x)\right]_{\mathrm{TA}}. \tag{2.50}$$

We again emphasize that only the traceless, anti-Hermitian part of $F_{\mu}(x)$ contributes to the molecular dynamics evolution.

With any large coding project, it is important to devise testing strategies to verify that the code is consistent with the analytic description. For the dynamical domain wall action, this process is quite simple and straight forward, provided one starts with an accurate implementation of the Wilson fermion matrix acting on a vector, some kind of linear solver, and the Wilson HMD force term. Before we implemented the domain wall action in the physics software environment of the QCDSP machines at Columbia, we ran several dynamical Wilson fermion simulations which were in good statistical agreement with the published results of other groups.

Since our linear solver, based on the conjugate gradient (CG) algorithm, solves the problem $\widetilde{M}^{\dagger}\widetilde{M}\chi = \Phi$, testing it simply requires choosing many different $\Phi$ sources,

solving each one for the corresponding $\chi$ solutions and then applying $\widetilde{M}^\dagger\widetilde{M}$ to $\chi$ and comparing the result to the original. This defines a quantity called the *true residual*

$$r = \frac{\left|\Phi - \widetilde{M}^\dagger\widetilde{M}\chi\right|}{|\Phi|} \tag{2.51}$$

where we use the vector 2-norm: $|\Phi| = \sqrt{\Phi^\dagger\Phi}$. However, running the CG algorithm for a sufficient number of iterations for $r$ to be smaller than some predetermined stopping condition only verifies that some non-singular linear system was solved.

To check that the linear system solved was actually involved the domain wall fermion matrix $\widetilde{M}^{\dagger(\mathrm{dwf})}\widetilde{M}^{(\mathrm{dwf})}$ acting on a vector, we compared the results of the solution run on a free lattice configuration, $U_\mu(x) \to \mathbb{1}$, to the analytic solution computed by Vranas [14]. We then extended our check to non-trivial gauge configurations by applying a random gauge transformation, $\Lambda(x) \in \mathrm{SU}(N_c)$, to the free lattice configuration, $U_\mu(x) \to \Lambda^\dagger(x)\Lambda(x+\hat{\mu})$, and verified that the true residual was invariant under gauge transformation

$$r = \frac{\left|\Lambda\Phi_0 - \widetilde{M}^\dagger_\Lambda\widetilde{M}_\Lambda\Lambda\chi_0\right|}{|\Lambda\Phi_0|} \tag{2.52}$$

where $\Phi_0, \chi_0$ are the free field source and solution verified by analytic calculation and $\widetilde{M}_\Lambda$ indicates the matrix is applied using the gauge transformed links. If the domain wall fermion matrix is properly implemented, then the true residual is a gauge-invariant quantity. When starting with a properly implemented Wilson fermion matrix, the gauge invariance test should not fail if the free field test passed, since the gauge fields only enter the domain wall matrix through the Wilson portion of the code. These tests passed within finite precision limits of the QCDSP machine.

The only difference between the force terms of the fermionic (2.47) and Pauli-Villars (2.49) parts of the domain wall action and the force term of $L_s$ independent flavors of Wilson fermions is in the computation of the input solution $\chi$. So, starting from an accurate implementation of dynamical Wilson fermions that supports multiple independent flavors makes the implementation of dynamical domain wall

fermions straightforward. In essence, once $\chi$ has been computed by the linear solver, $s$ is treated as a Wilson flavor index. As a final check, we also verified that the domain wall force terms transform properly under random gauge transformations.

After these series of analytic tests of the numerical implementation, it would have been nice to run an actual simulation and do a statistical comparison with published results. Since the simulations described here are the first of domain wall fermions in dynamical QCD, there are no previous published results. However, there were still two significant statistical tests which were run. First, we simulated dynamical domain wall fermions at $m_f$=1 on $8^3 \times 32$ volumes at $\beta$=5.7 and verified the results were consistent with quenched QCD. This check is not as trivial as it may seem, as the two parts of the domain wall force do not exactly cancel trajectory by trajectory since different pseudofermion fields are used for the fermionic and Pauli-Villars parts. Instead, the cancellation of forces happens stochastically, yielding quenched results in the limit of a large number of trajectories. Second, Vranas performed dynamical domain wall simulations of $N_f$=2 QCD on $2^4$ volumes [50] and found the results were in good statistical agreement with dynamical simulations done directly in the overlap formalism.

Perhaps the best test of the whole implementation of the CG solver and domain wall force working together within the context of the HMC algorithm comes from an application of Liouville's theorem by Creutz [51] within the classical framework of molecular dynamics. If we integrate out all of the fermion (or pseudofermion) fields, we can write the molecular dynamics partition function as a path integral over gauge fields and conjugate momenta

$$Z_{\mathrm{HMD}} = \int [\mathcal{D}U'] \, [\mathcal{D}H'] \, e^{-\mathcal{H}'} = \int [\mathcal{D}U] \, [\mathcal{D}H] \, e^{-\mathcal{H}} e^{\mathcal{H}-\mathcal{H}'}. \tag{2.53}$$

Since the HMD evolution is purely classical, the area preserving property of Liouville's theorem guarantees that the integration measures are equal: $[\mathcal{D}U'] \, [\mathcal{D}H'] = [\mathcal{D}U] \, [\mathcal{D}H]$. Dividing both sides by the partition function, $Z_{\mathrm{HMD}}$, we get the expec-

tation values

$$\langle \exp\left(-\Delta\mathcal{H}\right)\rangle = 1 \qquad (\Delta\mathcal{H} \equiv \mathcal{H}' - \mathcal{H}) \tag{2.54}$$

and, by Jensen's inequality,

$$\langle \Delta\mathcal{H}\rangle \geq 0. \tag{2.55}$$

Because $\Delta\mathcal{H}$ is computed as part of the Metropolis acceptance test of the HMC algorithm, it should be straightforward to calculate these observables in any actual simulation.

In our experience, satisfying these identities seems to be the most stringent check of the implementation of the HMC algorithm. If the force term is inconsistent with the Hamiltonian as implemented then Liouville's theorem will not hold because the evolution is no longer classical and area preserving with respect to the given Hamiltonian. However, the code necessary to compute the change in the Hamiltonian need not share any components with the force term except for the linear solver. Once the CG solver has been sufficiently tested, checking the Hamiltonian part of the code is simple, so these identities provide a demanding statistical test of the overall evolution, and in particular the HMD forces.

In chapter 3, the description of our simulations will include the observable (2.54). All of the runs, taken as a whole, agree with the prediction (2.54) within statistical error, from which we conclude that the domain wall HMC algorithm was correctly implemented.

# Chapter 3

# Simulations of $N_f$=2 QCD

## 3.1 The deconfinement phase transition

We are motivated to study the thermodynamics of $N_f$=2 QCD with degenerate light quarks for two reasons. First, it is an approximation to $N_f$=6 QCD with the six quarks at their physical masses. Recall from section 1.6 the discussion of the quenched limit of QCD, where dynamical quark effects are altogether eliminated by taking the bare quark masses to infinity. Similarly, the dynamics of the heavier quarks (*top, bottom*, $\cdots$) will be marginal in the Euclidean path integral and hence will have little effect on the character of the transition region. So, $N_f$=2 QCD is the most natural starting point for studying the role of dynamical quark effects in QCD thermodynamics.

At first glance, this theory, corresponding to a world where the *up* and *down* quark masses are degenerate and the rest are much heavier, is a reasonable approximation of our world. However, on closer inspection, the *up* and *down* quark masses are not exactly degenerate and the *strange* quark mass is only an order of magnitude heavier. So it will be important to perform the typically more computationally demanding $N_f$=3 QCD simulations with non-degenerate quarks to understand the full physical theory in detail. But, one should first study completely (if possible) the simpler $N_f$=2

theory before looking for (perhaps) subtle differences by turning on the dynamics of the heavier quark flavors.

A second motivation for this study is simply that $N_f$=2 QCD is an interesting theory in its own right. With massless quarks, the theory minimally has $\mathrm{SU}_L(2) \otimes \mathrm{SU}_R(2)$ chiral symmetry and the chiral condensate, $\langle \overline{q}q \rangle$, is an exact order parameter. This chiral symmetry group is expected to be in the O(4) universality class and other models in that class are known to have second order phase transitions, so there is a possibility that the chiral transition of $N_f$=2 massless QCD may be second order [28]. However, if the anomalously broken $\mathrm{U}_A(1)$ symmetry is effectively restored along with chiral symmetry at the transition, then the larger symmetry is expected to be in the $\mathrm{O}(2) \otimes \mathrm{O}(4)$ universality class and as other models in that class are known to have first order phase transitions there is the possibility that the chiral transition could be first order [28, 30, 31].

Before embarking on a large numerical project with a new fermion formulation, we note what is already known about QCD thermodynamics using other formulations, as all fermion formulations should give the same answer in the continuum limit. On $24^3 \times 4$ volumes in quenched QCD, there is a first order deconfinement phase transition at $\beta_c$=5.6925 [52]. Along with other quenched simulations, this corresponds in physical units to a critical temperature $T_c \simeq 270$ MeV [53].

For $N_f$=2 QCD with staggered fermions on $16^3 \times 4$ volumes, the finite temperature phase transition occurs at $\beta_c$=5.265 for $m$=0.01 and $\beta_c$=5.291 for $m$=0.025 [54, 55] which suggests that $\beta_c \approx 5.25$ in the chiral limit, approximately 150 MeV. At these quark masses, there is no evidence for a first order phase transition. Other $N_f$=2 dynamical simulations with different actions have critical temperatures in physical units in the range $T_c \simeq$ (170–190) MeV [53].

At finite lattice spacing the chiral symmetry of staggered fermions is only a one dimensional subgroup of the continuum symmetry and the vector flavor symmetry is

explicitly broken. Consequently, QCD with staggered fermions at accessible lattice spacings is a theory with one physically light pion and two unphysically heavy pions in the range 500–600 MeV. This may obscure the true nature of the transition until the lattice spacing is reduced or the action is improved.

In section 3.2, we will locate the transition region of $N_f$=2 QCD with moderately light degenerate quarks in small $8^3 \times 4$ volumes. Using the chiral condensate we will show strong evidence for a chiral phase transition in the massless quark limit. However, the small volumes used will make it difficult to establish detailed properties of the transition region. Thus, in section 3.3 we will focus in on the transition region in larger $16^3 \times 4$ volumes with somewhat lighter quarks in the hope of seeing an indication of the order of the transition.

Implicit throughout the preceding discussion is the assumption that the domain wall fermion formulation provides us with the nearly exact chiral symmetry needed to observe the critical phenomena related to spontaneous chiral symmetry breaking. In section 3.4, we will perform the analysis of the GMOR relation outlined in section 1.5 as a quantitative measure of the effectiveness of the domain wall method for producing nearly massless fermions on the lattice.

## 3.2 Locating the transition in $8^3 \times 4$ volumes

In the Euclidean path integral formulation, the temporal extent of the lattice $L_t$ is related to the inverse temperature $T^{-1}$ through the lattice spacing: $L_t = (aT)^{-1}$. If we hold $L_t$ fixed, then the determination of the temperature $T_c$ of the chiral phase transition requires, in general, searching in the space of the four parameters $(\beta, m_0, L_s, m_f)$ that determine the lattice spacing. The problem of searching this space is made simpler as we are only interested in the location of the transition in the chiral limit, as $m_f \to 0$ and $L_s \to \infty$, over an appropriate range of $m_0$. In the massless limit, the location is specified by the critical coupling, $\beta_c(m_0)$.

We first studied the behavior of both the Wilson line and chiral condensate in $8^3 \times 4$ volumes [40, 41, 43, 42, 56, 50]. Choosing the spatial extent of the lattice $L$ to be much larger than the temporal extent, $L \gg L_t$, is essential to eliminating the finite volume effects that obscure the character of the transition. However, past experience and this work will demonstrate that searching in small volumes with moderately heavy quarks gives a surprisingly good estimate of $\beta_c$. Further simulations at larger spatial volumes and smaller masses can refine the estimate of $\beta_c$ and reveal the character of the transition.

At very small lattice spacings, when the gauge fields are near the identity, the condition for bound domain wall states is essentially the free condition (1.49). For a large range of $m_0$, one light flavor will be localized on the domain wall defect. Of course, to use the HMC algorithm described in section 2.2, we must square the determinant which gives us two degenerate flavors. However, $m_0$ also determines the maximum four-momentum a bound surface state may have, see (1.49) for the condition in the free case, and is the mass scale of the heavy Wilson doubler states that are not localized on the defect. So, at coarser lattice spacing, these scales become relevant and the bare couplings and masses will have $m_0$-dependent contributions which should cause shifts in $\beta_c$. By locating $\beta_c$ for several $m_0$, we hope to establish that this parameter will not have to be fine-tuned on coarse lattices for the domain wall method to work, but some care must be taken in choosing a value to ensure the simulation represents the correct number of light flavors with a sufficiently large phase space for the light degrees of freedom.

Consideration of the existing numerical studies of QCD thermodynamics with quenched and dynamical $N_f$=2 staggered fermions provides us with a rough estimate of the location of $\beta_c$. For quenched $L_t = 4$ thermodynamics, corresponding to $m_f = 1$ in our parameter space, $\beta_c \approx 5.7$ and for dynamical staggered fermions in the chiral limit, similar to $m_f = 0$ and $L_s \to \infty$, $\beta_c \approx 5.25$. Since we are interested in the thermodynamics of domain wall fermions near the chiral limit, if we choose $m_f$

sufficiently small and $L_s$ sufficiently large then for some reasonable range of $m_0$ we should expect to find $\beta_c$ in the vicinity of the chiral staggered value.

To perform a fully dynamical search of the parameter space requires starting a new simulation each time any one of the basic run parameters $(L, L_t, \beta, m_0, L_s, m_f)$ is changed. Although the process of analyzing any given simulation is interesting in its own right, the sheer number of simulations included in this work prevent us from providing that level of detail. So, we encourage the reader to refer to the extensive tables and figures provided for details of any particular evolution.

Our search strategy for $8^3 \times 4$ volumes was to fix $m_f$=0.1, $L_s$=12 and for several values of $m_0$ from 1.15 to 2.4, we scan in $\beta$ from weak to strong coupling over the range $\beta$ = 5.95 – 4.65 until crossover behavior was observed in $\langle \overline{q}q \rangle$ and $\langle |W_3| \rangle$. The run parameters for the simulations are listed in tables 1 – 8. There were no difficulties with the CG algorithm failing to converge, characteristic of the "exceptional configuration" problem in dynamical Wilson fermions. When the even-odd preconditioned domain wall Dirac operator was used, as described in section 2.3, 100–130 CG iterations were typically needed per HMD step in the confined phase and 40–70 were needed in the deconfined phase. Simulations took three to five days to complete 800 HMC trajectories when run on a six Gflops portion of the QCDSP computer at Columbia. In some cases, when preconditioning was not used, two and a half times the number of CG iterations were needed per HMD step.

As the deconfined phase exists at weaker coupling than the confined phase, the gauge configurations are more ordered, *i. e.* closer to the identity configuration. So, the initial configuration for each simulation was deliberately chosen to be as far as possible from the anticipated state after thermalization. For simulations where a deconfined thermal state was expected, the initial lattice was disordered, while an initial ordered lattice was used where a confined thermal state was expected. This way, the thermalization time scale could be estimated by observing the system tunneling from the wrong phase through the transition into the correct phase.

The evolutions of $\langle \overline{q}q \rangle$ and $\langle |W_3| \rangle$ are shown in figures 1 – 16. The vertical dashed line indicates that data points to the left are considered part of thermalization and were not used to compute averages and autocorrelated errors. The figures clearly show that the short (microcanonical) time fluctuations are much larger in the confined phase than in the deconfined phase. Note that the data show a tendency for the thermalization time and the scale of large time fluctuations to increase towards the crossover region. This is an encouraging sign that correlation lengths are increasing towards the center of the crossover region, suggesting the long range order typical of phase transitions.

The averages and autocorrelated errors of $\langle \overline{q}q \rangle$ and $\langle |W_3| \rangle$ are plotted versus $\beta$ for $m_0 = 1.15$ – $1.8$ in figure 17 and $m_0 = 1.9$ – $2.4$ in figure 18. For $m_0 \gtrsim 1.65$ there is a clear indication of simultaneous rapid change in $\langle \overline{q}q \rangle$ and $\langle |W_3| \rangle$ versus $\beta$, indicative of a potential phase transition smoothed out by the moderately light quark mass and small volume. The reader should be careful to note the change in scale for $\langle \overline{q}q \rangle$ between the two figures. For $m_0 \lesssim 1.4$, there is still a crossover signal in $\langle |W_3| \rangle$, suspiciously close to the transition region for quenched QCD, but any signal in $\langle \overline{q}q \rangle$ is nearly gone.

Once we have identified the crossover region, we can estimate the location of $\beta_c$ through a fit of the approximate order parameters to the ansatz

$$f(\beta) = c_0 \left\{ c_1 + \tanh \left[ c_2 \left( \beta - \beta_c \right) \right] \right\} . \tag{3.1}$$

The results of the fits are in tables 9 and 10, plots of the fit curves versus the data are also shown in figures 17 and 18, and a plot of $\beta_c$ versus $m_0$ is in figure 19.

Although the purpose of the ansatz (3.1) is to estimate the inflection point $\beta_c$, the other parameters of the fit can be used to quantitatively describe what our eyes have already told us by looking at the figures. After extracting the overall scale factor $c_0$ we can compare $c_1$ and $c_2$ between the various fits. When $\mathrm{sign}(c_0) c_1 = 1$ then the fit describes an approximate order parameter that goes exactly to zero deep in the

the symmetric phase. $c_0c_2$ is the slope of the fit curve at the inflection point, so $c_2$ indicates the relative rate of crossover between the two phases. Examining table 9, we see from $c_1$ that the Wilson line is a good approximate order parameter and from $c_2$ that there is a tendency for the transition to broaden as $m_0$ increases.

In table 10 we see more interesting behavior. First, we note in figure 17 that the $\beta$-dependence of $\langle\overline{q}q\rangle$ for $m_0 \lesssim 1.4$ is not well modeled by (3.1). The tendency of $|c_0|$ to increase with increasing $m_0$ is expected since this is just the change in the overlap between our effective quark fields (1.51) and the actual light fermion modes suggested by (1.50). The vanishing of this overlap as $m_0 \lesssim 1.4$ is our first indication that any light fermion modes are, on average, no longer localized to the domain wall defect. Next, we note that $|c1| \gg 1$ for $m_0 \lesssim 1.4$ which indicates that $\langle\overline{q}q\rangle$ is no longer approaching zero in the symmetric phase and again suggests the phase space for light fermions on the defect is nearly gone. We conclude that domain wall fermions are unreliable for $N_f$=2 and $L_t$=4 thermodynamics with $m_0 \lesssim 1.4$. Because the fit ansatz is only intended to give a qualitative description of the data, we expect that $\chi^2/N_{\rm dof} \lesssim 10$ indicates a reasonable agreement between the data and the ansatz.

Finally, for $c_2$ we see the same tendency for the transition to broaden towards larger $m_0$. We expect that for some $m_0 > 2.0$ the simulations should behave like $N_f$=8 QCD but our data do not indicate any sharp crossover from $N_f$=2 QCD to $N_f$=8 QCD for $m_0 \leq 2.4$. One interpretation is that the simulations are $N_f$=2 with the shift in $\beta_c$ due to the change in the amount of phase space available to the light fermions as $m_0$ varies, in analogy to the free field condition (1.49). A related interpretation is that as the phase space for the two light modes decreases while the modes themselves become heavy for $m_0 \gtrsim 2.0$ the phase space for the eight doubler modes is increasing while the doubler modes become light, so that $m_0$ smoothly interpolates between two flavor and eight flavor thermodynamics.

Although the rapid crossovers seen in $8^3\times4$ volumes with $L_s$=12 and $m_f$=0.1 are indicative of a phase transition, the dynamical quarks are likely too heavy to expect

good chiral behavior. Furthermore, it is difficult at this point to quantify the residual chiral symmetry breaking effects due to finite $L_s$. We can strengthen our evidence for the existence of the phase transition by performing a dynamical extrapolation to the massless quark limit: $L_s \to \infty, m_f \to 0$. Thus, if we study the order parameter $\langle \overline{q} q \rangle$ outside the transition region and demonstrate that it is zero in the symmetric phase and non-zero in the broken phase then we are reassured that the rapid cross over is strong evidence for a phase transition in the chiral limit.

We choose $m_0$=1.9 to study the separate phases for several reasons. First, $m_0$=1.9 is sufficiently far from the region $m_0 \lesssim 1.4$ where the light surface states of domain wall fermions vanishes. Second, choosing $m_0$¡2 guarantees that at low momentum only a single light surface mode is bound to the domain wall so ensuring the low momentum phase space of an $N_f$=2 theory after squaring the determinant. Finally, although not strictly necessary, the value of $\beta_c$ is similar to the value for $N_f$=2 staggered fermions [57, 55].

To study the confining (broken) phase in an $8^3 \times 4$ volume with $m_0$=1.9, we choose $\beta$=5.2 as a good compromise between the desire to work at as weak a coupling as possible to suppress the residual chiral chiral symmetry breaking effects of finite $L_s$ and the need to be far enough from the crossover region that the results will be unaffected by the presence of a nearby phase transition. To perform the chiral extrapolation, we varied the bare quark mass $m_f$ over the range 0.02 to 0.18 and the extent of the extra dimension $L_s$ over the range 4 to 40. The run parameters and results are summarized in table 11.

Focusing on the chiral condensate, we expect from perturbation theory that $\langle \overline{q} q \rangle$ will be linear in the dynamical quark mass, $m_f$. In figure 20, we show constrained fits to both a linear ansatz and a quadratic ansatz for $L_s = 8, 16$ and $m_f = 0.02$ – 0.18. By examining the $\chi^2/N_{\rm dof}$ for each constrained fit in table 12 we can see that the data tend to be more linear in $m_f$ as $L_s$ increases.

For $m_f = 0.02, 0.1$ there are sufficient data to extrapolate $\langle \overline{q}q \rangle$ to $L_s \to \infty$ limit using an exponential ansatz. The results of these fits are shown in table 13 and figure 21. We can see that the fit of the data to the ansatz is reasonable. One might worry that the $\chi^2/N_{\rm dof}$ are somewhat large but it is likely that the true autocorrelated errors are underestimated due to the rather short length of evolutions. Using the values of $\langle \overline{q}q \rangle$ as $m_f \to 0$ from the fits in table 12, we can also extrapolate to $L_s \to \infty$ and we find

$$\lim_{L_s \to \infty} \left[ \lim_{m_f \to 0} \langle \overline{q}q \rangle \, (\beta = 5.2) \right] = 0.0061(1). \tag{3.2}$$

Checking to see if the order of limits changes the extrapolated value we take the $L_s \to \infty$ limits for $m_f = 0.02, 0.1$ and do an unconstrained linear extrapolation to $m_f \to 0$ and find

$$\lim_{m_f \to 0} \left[ \lim_{L_s \to \infty} \langle \overline{q}q \rangle \, (\beta = 5.2) \right] = 0.0061(1). \tag{3.3}$$

Thus, we conclude that there is a broken phase for $\beta \lesssim 5.2$ indicated by the $\langle \overline{q}q \rangle$ order parameter in the chiral limit.

To study the deconfined (symmetric) phase in $8^3 \times 4$ volumes with $m_0$=1.9, we choose to simulate with $\beta$=5.45. As before, we desire to run at as weak a coupling as is reasonable, but it is important not to go too deep into the symmetric phase as our physical volume will become too small and too hot to yield useful results. As before we varied $m_f$ over 0.02 – 0.18 and $L_s$ over 4 – 32. The run parameters and results are summarized in table 14. In figure 22, we show constrained fits for a linear and quadratic ansatz for $L_s$=8, $m_f$ = 0.02 – 0.18 and a fit to a linear ansatz for $L_s$=16 over the same range of $m_f$. We see immediately that the data appear much more linear than in the broken phase. This may occur because the rate of exponential suppression of chiral mixing of the domain wall states increases at weaker coupling. Another possibility is that the rate of exponential suppression may be larger in the symmetric phase due to the smoother gauge fields. This remains a question open for further study. Results of the fits are in table 15, where we have also included fits of the $L_s$=16 data constrained be zero at $m_f$=0.

As in the $\beta = 5.2$ study, we also fit exponential extrapolations to $L_s \to \infty$, see table 16 and following the same double limit procedure above, if we do not constrain the $L_s \to \infty, m_f \to 0$ limit of $\langle \overline{q}q \rangle$ to be zero, we get the extrapolated values

$$\lim_{L_s \to \infty} \left[ \lim_{m_f \to 0} \langle \overline{q}q \rangle \, (\beta = 5.45) \right] = 0.00010(5). \tag{3.4}$$

$$\lim_{m_f \to 0} \left[ \lim_{L_s \to \infty} \langle \overline{q}q \rangle \, (\beta = 5.45) \right] = 0.00011(5). \tag{3.5}$$

Furthermore, if we constrain the $L_s \to \infty, m_f \to 0$ limit of $\langle \overline{q}q \rangle$ to be zero, the quality of the fits does not change significantly. Thus, we conclude that our observations are explained by a deconfining chiral phase transition with $\langle \overline{q}q \rangle$ as the order parameter for that transition in the chiral limit.

## 3.3 The transition region in $16^3 \times 4$ volumes

In section 3.2, we provided strong evidence of a chiral phase transition for $N_f$=2 domain wall fermions in the massless limit: $m_f \to 0$, $L_s \to \infty$. After having bracketed the transition region in smaller spatial volumes, we would like to characterize the order of the phase transition. Working in large spatial volumes with light quarks is essential to observing the long range correlations typical of true critical behavior. We chose to increase the volume from $8^3 \times 4$ to $16^3 \times 4$. To make the quarks lighter, we chose a larger $L_s$=24 and a smaller $m_f$=0.02.

Recalling from QCD with staggered fermions that $\beta_c$ decreased slightly as the quark mass is decreased, we first ran simulations in $8^3 \times 4$ volumes to map out the shift in $\beta_c$. Further, having simulations in the transition region in two different spatial volumes will allow us to study systematic errors due to finite spatial volumes. The simulations were run at $\beta = 5.2$, 5.275, 5.325 and 5.45 with $m_0$=1.9. Table 17 contains the other run parameters for these simulations. As before, there were no difficulties with convergence of the CG algorithm. 300–450 CG iterations were typically needed per HMD step in the broken phase and transition region and 100–120 CG iterations

were needed in the symmetric phase. Simulations in the broken phase took about thirty days to complete 800 HMC trajectories when run on a six Gflops partition of the QCDSP computer.

The evolutions of $\langle\overline{q}q\rangle$ and $\langle|W_3|\rangle$ are shown in figures 24 and 25. The vertical dashed line indicates that data to the left are considered part of thermalization and were not used to compute averages and autocorrelated error estimates. Even more dramatically than in section 3.2, the short time fluctuations of $\langle\overline{q}q\rangle$ are much larger in the broken phase than the symmetric phase and the longer time correlations are clearly visible at $\beta$=5.325. In figure 26 we show $\langle\overline{q}q\rangle$ and $\langle|W_3|\rangle$ *vs.* $\beta$ and we see that $\beta$=5.325 is clearly in the middle of the transition region.

For $16^3\times 4$ volumes, we chose $\beta$ = 5.25 – 5.35, spaced at 0.025 intervals. Table 18 contains the other run parameters. Both ordered and disordered starts were run for each set of run parameters until observables measured on last three hundred trajectories of each simulation were in good statistical agreement. There were no difficulties with CG convergence. 260–300 CG iterations were typically needed per HMD step, with more iterations required in the middle of the transition region ($\beta\sim$ 5.325) than on the edges. To complete 800 HMC trajectories on a 25 Gflops partition of the QCDSP computer would take between 48 and 72 days.

The evolutions of $\langle\overline{q}q\rangle$ and $\langle|W_3|\rangle$ are shown in figures 27 and 28. Since two evolutions appear in each panel of the figure, separate vertical lines are used to indicate the start of the last 300 trajectories for each evolution in the panel. The evolutions show no convincing evidence for a two-state signal indicative of a first order phase transition.

The summary plots which display $\langle\overline{q}q\rangle$ and $\langle|W_3|\rangle$ versus $\beta$ are shown in figures 33 and 34. The most obvious feature of the transition for domain wall fermions is that it does not appear particularly steep. For comparison, we have also plotted $N_f$=2 staggered fermion data [55]. Based on the different symmetries of the two fermion

formulations, the staggered data show the transition when one pion is light and two are heavy whereas the DWF data show the transition for three degenerate pions.

Comparing the $8^3$ and $16^3$ volumes, we also see that the larger volume did reduce the short distance fluctuation in the signal. However, the point in the middle of the transition region, $\beta = 5.325$, does not show signs of the critical fluctuations indicative of a second order transition nor does it show the two state signal of a first order phase transition. Based on the broadness of the transition region and the absence of critical fluctuations, we believe that the domain wall states are still too heavy to reveal any critical behavior present in the massless theory.

To bolster our claim, we performed an $8^3 \times 32$ zero temperature scale setting calculation, with $\beta$=5.325, $m_0$=1.9, $L_s$=24, $m_f$=0.02 [58]. We found that $m_\rho$=1.18(3) and $m_\pi$=0.654(3) in lattice units. Using $m_\rho$ to set the lattice scale, $\beta_c$=5.325 corresponds to $T_c = 163(4)$ MeV and $m_\pi = 427(11)$ MeV in physical units. By comparison, for staggered fermions near $T_c$ for $L_t = 4$, one pion has a mass of $m_\pi \sim 230$ MeV and the other two are $m_{\pi_2} \sim 600$ MeV [57, 55]. This leads to several possible explanations for the difference in the widths of the crossover region for staggered and domain wall fermions. One possibility is that the width may depend on the difference in the pion spectrum: one light and two heavy pions for staggered *vs.* three moderately heavy pions for domain wall fermions.

We scanned through the domain wall crossover region by changing $\beta$ holding other parameters, particularly $m_f$ and $L_s$, fixed. We expect that additive renormalizations of the bare quark mass, $m_{\text{res}}$ in the discussion of section 1.5, will be smaller at weaker coupling. The mass of the domain wall pions suggest $m_{\text{res}} \gtrsim m_f$ so it is possible that the effective bare quark mass, $m_{\text{eff}} = m_f + m_{\text{res}}$ may also be rapidly changing through the transition region, leading to qualitatively different behavior than staggered fermions, where the effective bare mass did not change through the transition region. This will be discussed further in section 3.4.

Besides the relatively heavy domain wall quark masses to account for the broadening of the crossover region relative to staggered fermions, a final possibility is that the staggered lattice spacing evolves rapidly as a function of bare coupling in the transition region, implying the crossover behavior for domain wall and staggered would be similar if shown in physical units. The dependence of the staggered lattice spacing on the bare parameters in the transition region was extensively studied by Blum, *et al.* [59]. Summary plots which display the staggered chiral condensate $\langle\overline{\chi}\chi\rangle$ and Wilson line $\langle|W_3|\rangle$ *vs.* temperature $T$ in MeV are shown in figures 35 and 36.

As we ran only a single zero temperature domain wall scale setting calculation in the transition region, there are insufficient data to make a non-perturbative determination of the functional dependence of the lattice spacing on the bare parameters, as was done for staggered fermions. Close to the continuum limit, it would only be necessary to determine the lattice spacing for one set of bare parameters as the lattice spacings at other bare parameters are given by the asymptotic scaling relation for two flavors of massless fermions

$$a\Lambda_{\rm LAT} = \left(8\pi^2\beta/29\right)^{345/841} \exp\left(-4\pi^2\beta/29\right) \tag{3.6}$$

where $\Lambda_{\rm LAT}$ is the lattice scale parameter which must be determined by a scale setting calculation. The relation (3.6) is the result of a two loop perturbative calculation and only contains terms which are independent of renormalization scheme. However, the value of the parameter $\Lambda$ will depend upon the renormalization scheme

Solving (3.6) for $\Lambda_{\rm LAT}$ in our $8^3 \times 32$ scale setting calculation at $\beta$=5.325 mentioned above, we find $\Lambda_{\rm LAT}$=1.388(2) MeV[1]. Holding $\Lambda_{\rm LAT}$ fixed, we can estimate the temperature at other couplings holding the other bare parameters fixed. Although the effective bare quark mass will change as we change the coupling, as noted above, we emphasize that $m_\rho$ is typically less sensitive to small changes in the quark mass

[1]The difference between this $\Lambda_{\rm LAT}$ and the more familiar $\Lambda_{\overline{\rm MS}} \sim 200$ MeV is merely due to large scheme-dependent factors.

than $m_\pi$ so we expect that this may not be a large source of systematic error. Using this method, we also plot the domain wall chiral condensate $\langle\overline{q}q\rangle$ and Wilson line $\langle|W_3|\rangle$ *vs.* temperature $T$ in MeV in figures 35 and 36. Plotting both the staggered and domain wall data *vs.* temperature has not resolved the difference between the widths of the crossover regions for the two formulations, assuming that the violations of the scaling relation (3.6) are not large due to the relatively strong couplings. We will examine this issue below where we have two scale setting calculations at different couplings to estimate the size of the scaling violations.

After realizing that the pion mass was too heavy to reveal critical phenomena, we could, in principle, merely increase $L_s$ until we achieve the desired pion mass. Unfortunately, the $16^3 \times 4, L_s = 24$ calculation is essentially the largest scale study we were able to conduct in a reasonable amount of time. So, we decided to pursue improvements to our lattice action which we hoped would reduce the pion mass significantly for roughly the same computational effort.

Encouraged by published quenched results which indicated that replacing the standard Wilson gauge action (1.23) with the improved rectangle action (1.25) can reduce the quenched pion mass [60, 58], we located the $N_f$=2, $L_t$=4 transition region for this action in $8^3 \times 4$ volumes with $c_1$=-0.331, $m_0$=1.9, $L_s$=24, $m_f$=0.02 [42, 56]. The choice of $c_1 = -0.331$ stems from early work by Iwasaki [61, 62]. Although the rationale of his approach probably has little relevance to this work, choosing this value eliminates the need for costly study of the effects of varying $c_1$. Simulating with the additional term in the gauge action did not significantly increase the computational cost relative to the standard action because the cost is dominated by the CG algorithm. Table 19 contains the other run parameters for these simulations.

The evolutions of $\langle\overline{q}q\rangle$ and $\langle|W_3|\rangle$ are shown in figures 29 and 30. As before, data to the left of the vertical dashed line in each panel were considered thermalization and not used to compute averages and autocorrelated errors. Ordered and disordered starts were run at each $\beta$ until the averages of observables agreed within errors for at

least the last 100 trajectories. As with domain wall fermions with the Wilson gauge action, the short distance fluctuations of $\langle \overline{q}q \rangle$ are diminished in the symmetric phase.

Following the $8^3 \times 4$ study to locate the transition region, we performed a detailed study of the transition region in $16^3 \times 4$ volumes. Table 20 contains the run parameters for these simulations. The evolutions of $\langle \overline{q}q \rangle$ and $\langle |W_3| \rangle$ are shown in figures 31 and 32. The summary plot which display $\langle \overline{q}q \rangle$ versus $\beta$ is shown in figure 37 for both $8^3 \times 4$ and $16^3 \times 4$ volumes. Contrary to the observed decrease in the pion mass for quenched domain wall fermions with the Iwasaki gauge action at zero temperature, the broadening the transition region at finite temperature again indicates a moderately heavy pion for dynamical domain wall fermions with Iwasaki gauge action ($c_1$=-0.331) as was the case with the Wilson gauge action ($c_1$=0).

We performed $8^3 \times 32$ zero temperature scale setting calculations in the transition region, with $\beta$=1.9 and 2.0, $c_1$=-0.331, $m_0$=1.9, $L_s$=24 and $m_f$=0.02 [58]. For $\beta$=1.9, which appears to be in the central part of the transition region, the dimensionless lattice meson masses are $m_\rho$=1.16(2) and $m_\pi$=0.604(3) and, using $m_\rho$ to determine the lattice spacing give the physical temperature $T$= 166(3) MeV and physical pion mass $m_\pi^{(\mathrm{phys})}$= 400(7) MeV. This confirms our suspicion that the improved gauge action (1.25) does not significantly improve the chiral behavior of dynamical domain wall fermions at strong coupling.

We used the same asymptotic scaling technique as before to extrapolate the lattice spacing as a function of the bare coupling $\beta$ and find $\Lambda_{\mathrm{LAT}}$=98.0(1) MeV. We can now directly compare the transition regions of the two domain wall QCD actions. In figures 39 and 40 we show the chiral condensate $\langle \overline{q}q \rangle$ and the Wilson line $\langle |W_3| \rangle$ for the standard Wilson gauge action ($c_1$=0) and the Iwasaki gauge action ($c_1$=-0.331). While the relative offset between the two curves may be due to uncertainties in the overall temperature scale of the scaling functions for each data set, superficially it appears that the rectangle improvement in the gauge action did not reduce the width of the transition region.

For the $8^3 \times 32$ zero temperature scale setting calculations with $\beta$=2.0, $c_1$=-0.331, $m_0$=1.9, $L_s$=24 and $m_f$=0.02 [58], the dimensionless lattice meson masses are $m_\rho$=0.95(3) and $m_\pi$=0.475(7) and, using $m_\rho$ to set the scale gives a physical temperature $T$=202(6) MeV. Note that $m_\pi/m_\rho$=0.5, within errors, for both $\beta$=1.9 and $\beta$=2.0 simulations. Using (3.6) to extrapolate the scale from $\beta$=1.9 gives a physical temperature of $T_{\rm ext}$=186 MeV. Violations of asymptotic scaling are around eight percent for a five percent change in $\beta$. So, determining the scale from the asymptotic scaling relation (3.6) tends to make the transition region appear narrower than it would be if a non-perturbative scaling relation were used.

While there were many interesting indications that observations of true critical behavior might be possible on $L_t = 4$ lattices with domain wall fermions, it is clear from the size of the pion mass in physical units that $L_s = 24$ is too small to suppress the large chiral symmetry breaking effects at strong coupling. In section 3.4, we will address the issue of exactly how large an $L_s$ is needed to substantially reduce the mass of the dynamical pions in the broken phase and transition region. However, we can also tell from our preceding discussion that chiral symmetry breaking effects are much smaller in the symmetric phase. Not only does the symmetric phase occur at weaker coupling, but reduced average CG iterations per HMC step and the increased rate of exponential decay as $L_s \to \infty$ for $\langle \overline{q}q \rangle$ seen in section 3.2 are strong indications that $L_s = 24$ or even $L_s = 16$ may be sufficient for simulations in the chirally symmetric phase of QCD on $L_t = 4$ lattices.

## 3.4 Effects of finite $L_s$ in the confined phase

One of the primary advantages of using domain wall fermions to study two flavor QCD thermodynamics is the extra parameter $L_s$ which allows us to control chiral symmetry breaking. In section 3.1 we concluded that the mass of the pion state indicated that the amount of chiral symmetry breaking for domain wall fermions with $L_s = 24$ was,

at best, only moderately better than existing calculations, which are computationally less demanding by an order of magnitude. See figure 2 of Karsch's LATTICE 99 review talk [53].

In defense of the domain wall method, it is important to note that it is currently not possible to simulate in the $(aT_c)^{-1}$=4 region of the parameter space with *three* light pions close to their physical mass scale for any of the standard fermion actions. So, the relevant questions are why is the pion so heavy for $L_s$=24 and how large do we need to make $L_s$ to reduce all three pions to their physical range. After addressing these questions, we will have established a framework to study what improvements are possible to reduce chiral symmetry breaking without increasing $L_s$. The framework we propose is the Gell-Mann, Oakes, and Renner relation (1.85) discussed in section 1.5.

In conjunction with the low temperature phase study of the chiral condensate in $8^3 \times 4$ volumes with $\beta$=5.2 and $m_0$=1.9, described in section 3.2, we also measured $\langle \overline{q} q \rangle$ and $\chi_\pi$ at the dynamical mass and various valence masses for several values of $L_s$. Tables 21 and 22 summarize these observables.

In figure 41, we show the mid-plane contribution to the axial current, $\Delta J_5 = \langle \overline{q} q \rangle - m_f \chi_\pi$, from (1.85). Since the GMOR relation (1.85) holds configuration by configuration, we could define a $\Delta J_5$ for each configuration. However, in our simulations we only measured the chiral condensate averaged over the spacetime volume $\langle \overline{q} q \rangle$ and not the contribution from a single point $\langle \overline{q}_0 q_0 \rangle$ required in (1.85). However, the expectation values of two condensates will agree in the ensemble average, $\langle \overline{q} q \rangle \approx \langle \overline{q}_0 q_0 \rangle$, our definition of $\Delta J_5$ is valid as the difference of two expectation values. We used the jackknife method to estimate the error of $\Delta J_5$. The long dashed line in the figure is the fit $\Delta J_5 = 0.0096(2) \exp\left[-0.0190(8) L_s\right]$ over the range $L_s \in [16, 40]$ with $\chi^2$/dof=6.5/2. Although the $\chi^2$ of the fit is a little high, we see that the points appear to scatter along the straight line on the log scale. So, our data are consistent with chiral symmetry restoration in the $L_s \to \infty$ limit.

We can decompose the effects of finite $\Delta J_5$ by extracting the additive mass renormalization $m_{\rm res}$ and the chiral condensate subtraction $b_0$ using the valence data in tables 21 and 21 and the ansatz

$$\langle \overline{q} q \rangle = (m_f + m_{\rm res})\, \chi_\pi + b_0 \tag{3.7}$$

from (1.85) and (1.95). We simultaneously fit $\langle \overline{q} q \rangle$ and $\chi_\pi$ over $m_f^{(\rm val)} \in [0.02, 0.14]$ for each $L_s$. To perform this fit, we must further assume $\chi_\pi$ can be parameterized as in (1.88). We then fit $m_{\rm res}$ and $b_0$ to a decreasing exponential in $L_s$. The whole fitting procedure is run under a jackknife loop. The fit did not account for correlations between data points because there were insufficient data to accurately determine the correlation matrix. Our previous experience with this fit ansatz using quenched data [22] suggests that including the effects of correlations does not change the answer significantly.

The results are in table 23, all errors quoted are jackknife errors. In figure 42, we show the $L_s$-dependence of $m_{\rm res}$ and $-b_0$ using ten jackknife blocks. The exponential fits shown, with jackknife errors, are

$$-b_0 = 0.0106(8) \exp\left[-0.016(3) L_s\right], \quad \chi^2/\text{dof} = 0.19(11) \tag{3.8}$$

$$m_{\rm res} = 0.18(1) \exp\left[-0.026(3) L_s\right], \quad \chi^2/\text{dof} = 0.08(9) \tag{3.9}$$

The fitting range is $L_s \in [10, 40]$ and there are four degrees of freedom. Although the rate of exponential decay is slow, again we note that our data are consistent with chiral symmetry restoration in the $L_s \to \infty$ limit. If we use the asymptotic scaling relation (3.6) to extrapolate the lattice spacing from the $8^3 \times 32$, $\beta$=5.325 scale setting calculation described in section 3.3, we get $a^{-1} \approx 550$ MeV with an unknown systematic error due to violations of asymptotic scaling. So, in physical units, the bare lattice quark mass is $m_f^{(\rm phys)} \approx 10$ MeV and the bare residual quark mass at $L_s$=24 is $m_{\rm res}^{(\rm phys)} \approx 50$ MeV.

In table 24, we show the valence GMOR parameters $m_{\rm res}$ and $b_0$ for the scale setting calculations [58] which supported the transition region study in section 3.1.

In the first column, "W" implies the Wilson gauge action (1.23) and "R" implies the rectangle action (1.25) with the choice $c_1 = -0.331$. As before, there were insufficient data to accurately estimate the correlation matrix, so it was not included in the fit. From the $8^3 \times 32$ scale setting calculations described in section 3.3, we know that the lattice spacing for domain wall fermions with the Wilson gauge action at $\beta = 5.325$ is $a^{-1}$=652(17) MeV. Using the lattice spacing, we express the dynamical bare lattice quark mass as $m_f^{(\text{phys})}$=13.0(3) MeV, in physical units, and the bare residual quark mass as $m_{\text{res}}^{(\text{phys})}$=37(2) MeV. When compared with the $\beta$=5.2 simulations above, we find clear evidence supporting the perturbative expectation that chiral symmetry breaking effects are smaller at weaker coupling, for a fixed $L_s$=24.

Now, we can estimate whether a fourfold increase in $L_s$ to $L_s$=96 would be sufficient to reduce the pion masses to a physically interesting scale. First, we will imagine that a zero temperature calculation would be done on $8^3 \times 32$ with $\beta$=5.325, $m_0$=1.9 and $L_s$=96. A conservative estimate of the exponential decay of the residual mass at $\beta = 5.325$ is $m_{\text{res}} \propto \exp(-0.03 L_s)$ since this agrees with the observed rate at $\beta$=5.2 within error. With this decay rate, the bare lattice would be $m_{\text{res}} \approx 0.007$ at $L_s$=96. Choosing the bare lattice quark mass of $m_f$=0.01 gives $m_f \gtrsim m_{\text{res}}$ and will reduce the possibility of large changes in the effective bare mass while scanning through the transition region. In [58], the dynamical bare quark mass dependence of the pion mass was determined to be $m_\pi^2 \propto 5.38 m_f$ when $L_s$=24. Assuming the same slope will be found when $L_s$=96 and that the pion mass vanishes (in an infinite volume) at $m_f \approx -0.007$, then the dimensionless pion mass will be $m_\pi \approx 0.3$. Using the lattice spacing found at $L_s$=24 and $m_f$=0.02, the physical pion mass should be $m_\pi^{(\text{phys})} \approx 200$ MeV at $L_s$=96, a physically interesting scale.

The GMOR relation does provide a useful framework to study the chiral symmetry breaking effects of finite domain wall separation. However, one must be careful when choosing a parameterization of $\Delta J_5$ that the physical assumptions remain valid throughout the region of coupling space of interest. Since our assumption was based

on the existence of a pion pole due to spontaneous chiral symmetry breaking, the method described here is only applicable in the confined phase.

# Concluding remarks

We have established that domain wall fermions preserve the full chiral and flavor symmetries of QCD. However, these features come at a substantial cost: one and sometimes two orders of magnitude increase in computational effort. So, it is important to carefully choose problems where the role of chiral symmetry is crucial to determining the correct answer to the problem and similar quality results could not be obtained by simply redirecting the increased computational effort into working at smaller lattice spacings using less demanding formulations, like staggered or Wilson fermions.

The problem we chose to study is the finite temperature phase transition and quark-gluon plasma phase of $N_f$=2 QCD. This is a particularly challenging problem because the finite temperature calculations are usually performed at stronger couplings than comparable calculations at zero temperature. This is also a particularly challenging problem for the domain wall fermion formulation as the suppression of chiral symmetry breaking effects at stronger couplings requires larger values of $L_s$.

From this work it seems clear that domain wall fermions work as advertised. The hybrid Monte Carlo (HMC) and conjugate gradient (CG) algorithms worked without any difficulty beyond the linear increase in computational cost proportional to $L_s$. The only negative aspect of this work was that the computational resources were not four times larger, the amount necessary to simulate on $16^{\times}4$ lattices with dynamical pions close to their physical masses.

Despite this limitation, several important physical results were reported here. On $8^3 \times 4$ volumes, extrapolations to the chiral limit, $m_f \to 0$ and $L_s \to \infty$, on either side of the crossover region give a clear evidence of the existence of a finite temperature phase transition that restores chiral symmetry in the chiral limit.

For the first time ever [53], we performed simulations on $16^3 \times 4$ volumes with three dynamical pions whose masses were on the order of 400 MeV. Unfortunately, simulations with 400 MeV pions are not sufficiently close to the chiral limit to exhibit convincing evidence of the order of the chiral transition. Of course, even reducing the mass of the dynamical pions to 200 MeV may not be sufficient to uncover evidence of the chiral transition. However, pions are not massless in nature, so the width of the crossover region with dynamical pions near their physical value is certainly of phenomenological interest.

Finally, from our study of the GMOR relation, we can determine the residual chiral symmetry breaking effects of domain wall fermions at finite $L_s$. Using the GMOR relation, we found these effects were characterized in terms of a residual mass $m_{\text{res}}$ which decreases exponentially in $L_s$. In the transition region, for $L_s$=24 and $m_f$=0.02 the effective bare quark mass was dominated by finite $L_s$ effects that were too large to allow dynamical pions near the physical pion mass. However, we argued quite conservatively that a fourfold increase in $L_s$ with $m_f$=0.01 should be sufficient for the effective bare quark mass to be dominated by $m_f$ in the transition region and allow for the masses of the three dynamical pions should be near their physical values.

We believe the full characterization of the $L_t = 4$ transition region will be completely accessible to the next generation of supercomputers, even without substantial improvement of the domain wall action or algorithms. However, many exciting questions about the high temperature phase, like the equation of state [63], can still be addressed using the current generation of supercomputers.

# Bibliography


[1] I. Montvay and G. Münster, "Quantum Fields on a Lattice," *Cambridge, UK: Univ. Pr. (1994). (Cambridge monographs on mathematical physics).*

[2] H. J. Rothe, "Lattice Gauge Theories: An introduction," 2nd Ed., *Singapore, Singapore: World Scientific (1997).*

[3] K. G. Wilson, "Confinement of quarks," Phys. Rev. **D10**, 2445 (1974).

[4] K. G. Wilson, "Monte Carlo calculations for the lattice gauge theory," in *Recent Developments in Gauge Theories. Proceedings, Nato Advanced Study Institute, Cargese, France, August 26 - September 8, 1979,* ed. G. 't Hooft *et al.,* Plenum Press, New York, 1980, p. 363, (Nato Advanced Study Institutes Series: Series B, Physics, 59), Print-79-1032 (CORNELL).

[5] H. B. Nielsen and M. Ninomiya, "Absence of neutrinos on a lattice. 1. Proof by homotopy theory," Nucl. Phys. **B185**, 20 (1981), Erratum–ibid. **B195**, 541 (1982).

[6] H. B. Nielsen and M. Ninomiya, "Absence of neutrinos on a lattice. 2. Intuitive topological proof," Nucl. Phys. **B193**, 173 (1981).

[7] K. G. Wilson, "Quarks and strings on a lattice," in *New Phenomena in Subnuclear Physics. Part A. Proceedings of the First Half of the 1975 International School of Subnuclear Physics, Erice, Sicily, July 11 - August 1, 1975*, ed. A. Zichichi, Plenum Press, New York, 1977, p. 69, CLNS-321.

[8] D. B. Kaplan, "A method for simulating chiral fermions on the lattice," Phys. Lett. **B288**, 342 (1992) [hep-lat/9206013].

[9] D. B. Kaplan, "Chiral fermions on the lattice," Nucl. Phys. Proc. Suppl. **30**, 597 (1993).

[10] S. A. Frolov and A. A. Slavnov, "An invariant regularization of the Standard Model," Phys. Lett. **B309**, 344 (1993).

[11] R. Narayanan and H. Neuberger, "Infinitely many regulator fields for chiral fermions," Phys. Lett. **B302**, 62 (1993) [hep-lat/9212019].

[12] Y. Shamir, "Chiral fermions from lattice boundaries," Nucl. Phys. **B406**, 90 (1993) [hep-lat/9303005].

[13] P. M. Vranas, "Domain wall fermions and Monte Carlo simulations of vector theories," Nucl. Phys. Proc. Suppl. **53**, 278 (1997) [hep-lat/9608078].

[14] P. M. Vranas, "Chiral symmetry restoration in the Schwinger model with domain wall fermions," Phys. Rev. **D57**, 1415 (1998) [hep-lat/9705023].

[15] H. Neuberger, "Vector-like gauge theories with almost massless fermions on the lattice," Phys. Rev. **D57**, 5417 (1998) [hep-lat/9710089].

[16] Y. Kikukawa and A. Yamada, "Weak coupling expansion of massless QCD with a Ginsparg-Wilson fermion and axial U(1) anomaly," Phys. Lett. **B448**, 265 (1999) [hep-lat/9806013].

[17] V. Furman and Y. Shamir, "Axial symmetries in lattice QCD with Kaplan fermions," Nucl. Phys. **B439**, 54 (1995) [hep-lat/9405004].

[18] R. Narayanan and H. Neuberger, "Chiral determinant as an overlap of two vacua," Nucl. Phys. **B412**, 574 (1994) [hep-lat/9307006].

[19] R. Narayanan and H. Neuberger, "A construction of lattice chiral gauge theories," Nucl. Phys. **B443**, 305 (1995) [hep-th/9411108].

[20] M. Gell-Mann, R. J. Oakes and B. Renner, "Behavior of current divergences under SU(3) × SU(3)," Phys. Rev. **175**, 2195 (1968).

[21] G. T. Fleming *et al.*, "The domain wall fermion chiral condensate in quenched QCD," Nucl. Phys. Proc. Suppl. **73**, 207 (1999) [hep-lat/9811013].

[22] G. T. Fleming, "How well do domain wall fermions realize chiral symmetry?," Nucl. Phys. Proc. Suppl. **83**, 363 (2000) [hep-lat/9909140].

[23] A. M. Polyakov, "Thermal properties of gauge fields and quark liberation," Phys. Lett. **72B**, 477 (1978).

[24] L. Susskind, "Lattice models of quark confinement at high temperature," Phys. Rev. **D20**, 2610 (1979).

[25] L. McLerran and B. Svetitsky, "A Monte Carlo study of SU(2) Yang-Mills theory at finite temperature," Phys. Lett. **98B**, 195 (1981).

[26] J. Kuti, J. Polonyi and K. Szlachanyi, "Monte Carlo study of SU(2) gauge theory at finite temperature," Phys. Lett. **98B**, 199 (1981).

[27] A. J. Paterson, "Coleman-Weinberg symmetry breaking in the chiral SU($N$) × SU($N$) linear sigma model," Nucl. Phys. **B190**, 188 (1981).

[28] R. D. Pisarski and F. Wilczek, "Remarks on the chiral phase transition in chromodynamics," Phys. Rev. **D29**, 338 (1984).

[29] B. Svetitsky, "Symmetry aspects of finite temperature confinement transitions," Phys. Rept. **132**, 1 (1986).

[30] F. Wilczek, "Application of the renormalization group to a second order QCD phase transition," Int. J. Mod. Phys. **A7**, 3911 (1992).

[31] K. Rajagopal and F. Wilczek, "Static and dynamic critical phenomena at a second order QCD phase transition," Nucl. Phys. **B399**, 395 (1993) [hep-ph/9210253].

[32] S. Chandrasekharan, "Critical Behavior at the QCD Phase Transition," Ph.D. Thesis, Columbia University, New York, 1996, UMI-96-16699.

[33] S. Gottlieb *et al.*, "Thermodynamics of lattice QCD with two light quark flavours on a $16^3 \times 8$ lattice. II," Phys. Rev. **D55**, 6852 (1997) [hep-lat/9612020].

[34] C. Bernard *et al.*, "Which chiral symmetry is restored in high temperature QCD?," Phys. Rev. Lett. **78**, 598 (1997) [hep-lat/9611031].

[35] J. B. Kogut, J. F. Lagae and D. K. Sinclair, "Topology, fermionic zero modes and flavor singlet correlators in finite temperature QCD," Phys. Rev. **D58**, 054504 (1998) [hep-lat/9801020].

[36] S. Chandrasekharan, D. Chen, N. H. Christ, W. Lee, R. D. Mawhinney and P. M. Vranas, "Anomalous chiral symmetry breaking above the QCD phase transition," Phys. Rev. Lett. **82**, 2463 (1999) [hep-lat/9807018].

[37] P. Chen *et al.*, "Domain wall fermion zero modes on classical topological backgrounds," Phys. Rev. **D59**, 054508 (1999) [hep-lat/9807029].

[38] A. L. Kaehler *et al.*, "The anomaly and topology in quenched QCD above $T_c$," Nucl. Phys. Proc. Suppl. **73**, 405 (1999).

[39] A. L. Kaehler, "Anomalous Effects in Lattice QCD with Staggered Fermions," Ph.D. Thesis, Columbia University, New York, 1999.

[40] P. M. Vranas *et al.*, "Dynamical QCD thermodynamics with domain wall fermions," Nucl. Phys. Proc. Suppl. **73**, 456 (1999) [hep-lat/9809159].

[41] N. H. Christ *et al.*, "Toward the chiral limit of QCD: quenched and dynamical domain wall fermions," [hep-lat/9812011].

[42] G. T. Fleming, "Dynamical lattice QCD thermodynamics with domain wall fermions," Nucl. Phys. **A663-664**, 979 (2000) [hep-ph/9910453].

[43] P. M. Vranas, "Dynamical lattice QCD thermodynamics and the $U_A(1)$ symmetry with domain wall fermions," to appear in the Proceedings of the American Physical Society (APS) Meeting of the Division of Particles and Fields (DPF 99), Los Angeles, CA, 5-9 Jan 1999, [hep-lat/9903024].

[44] P. M. Vranas, "Domain wall fermions in vector theories," [hep-lat/0001006].

[45] S. Gottlieb, W. Liu, D. Toussaint, R. L. Renken and R. L. Sugar, "Hybrid molecular dynamics algorithms for the numerical simulation of quantum chromodynamics," Phys. Rev. **D35**, 2531 (1987).

[46] G. H. Golub and C. F. Van Loan, "Matrix Computations," 3rd Ed., *Baltimore, MD, USA: John Hopkins Univ. Pr. (1996).*

[47] T. A. DeGrand, "A conditioning technique for matrix inversion for Wilson fermions," Comput. Phys. Commun. **52**, 161 (1988).

[48] T. A. DeGrand and P. Rossi, "Conditioning techniques for dynamical fermions," Comput. Phys. Commun. **60**, 211 (1990).

[49] M. R. Hestenes and E. Stiefel, "Methods of conjugate gradients for solving linear systems," J. Res. Nat. Bur. Stand. **49**, 409 (1952).

[50] P. Chen *et al.*, "The finite temperature QCD phase transition with domain wall fermions," [hep-lat/0006010].

[51] M. Creutz, "Global Monte Carlo algorithms for many fermion systems," Phys. Rev. **D38**, 1228 (1988).

[52] F. R. Brown, N. H. Christ, Y. F. Deng, M. S. Gao and T. J. Woch, "Nature of the deconfining phase transition in SU(3) lattice gauge theory," Phys. Rev. Lett. **61**, 2058 (1988).

[53] F. Karsch, "Lattice QCD at finite temperature and density," Nucl. Phys. Proc. Suppl. **83**, 14 (2000). [hep-lat/9909006].

[54] A. G. Vaccarino, "The flavor dependence of the QCD finite temperature phase transition," Nucl. Phys. Proc. Suppl. **20**, 263 (1991).

[55] A. G. Vaccarino, "Numerical Studies of the QCD Finite Temperature Phase Transition with Two and Three Flavors of Light Quarks," Ph. D. Thesis, Columbia University, New York, 1991, UMI-92-09900.

[56] P. M. Vranas "The finite temperature QCD phase transition with domain wall fermions," Nucl. Phys. Proc. Suppl. **83**, 414 (2000) [hep-lat/9911002].

[57] F. R. Brown *et al.*, "On the existence of a phase transition for QCD with three light quarks," Phys. Rev. Lett. **65**, 2491 (1990).

[58] L. Wu [RIKEN-BNL-CU Collaboration], "QCD hadron spectrum with domain wall fermions," Nucl. Phys. Proc. Suppl. **83**, 224 (2000) [hep-lat/9909117].

[59] T. Blum, L. Karkkainen, D. Toussaint and S. Gottlieb, "The beta function and equation of state for QCD with two flavors of quarks," Phys. Rev. **D51**, 5153 (1995) [hep-lat/9410014].

[60] C. I. Malureanu, "Domain Wall Fermion Quenched Spectroscopy," Ph. D. Thesis, Columbia University, New York, 1999.

[61] Y. Iwasaki, "Renormalization group analysis of lattice theories and improved lattice action. 2. Four-dimensional non-Abelian SU($N$) gauge model," UTHEP-118.

[62] Y. Iwasaki, "Renormalization group analysis of lattice theories and improved lattice action: Two-dimensional nonlinear O($N$) sigma model," Nucl. Phys. **B258**, 141 (1985).

[63] G. T. Fleming, "Thermodynamics of free domain wall and overlap fermions," [hep-lat/0011069].

# Tables

Table 1: Run parameters for $\beta_c(m_0 = 1.15)$ search

vol: $8^3 \times 4$, $m_0 = 1.15$, $L_s = 12$, $m_f = 0.1$

HMC traj. len: $\frac{1}{50} \times 25$, CG stop cond: $10^{-6}$

| $\beta$ | start | # traj | acc. | $\langle e^{-\Delta H} \rangle$ | plaq. | $\langle \lvert W_3 \rvert \rangle$ | $\langle \overline{q} q \rangle$ |
|---|---|---|---|---|---|---|---|
| 5.45 | O | 100-800 | 0.87 | 0.99(1) | 0.470(1) | 0.0168(6) | 0.00276(1) |
| 5.55 | O | 200-800 | 0.87 | 0.98(1) | 0.4933(6) | 0.023(1) | 0.002916(6) |
| 5.65 | O | 300-800 | 0.87 | 1.00(2) | 0.5218(9) | 0.054(6) | 0.00305(2) |
| 5.75 | D | 300-800 | 0.86 | 0.986(9) | 0.5571(7) | 0.196(7) | 0.002875(7) |
| 5.85 | D | 300-800 | 0.85 | 1.00(1) | 0.5719(7) | 0.234(3) | 0.002881(3) |
| 5.95 | D | 200-800 | 0.87 | 0.99(1) | 0.5857(5) | 0.262(2) | 0.002898(3) |

Table 2: Run parameters for $\beta_c(m_0 = 1.4)$ search

vol: $8^3 \times 4$, $m_0 = 1.4$, $L_s = 12$, $m_f = 0.1$

HMC traj. len: $\frac{1}{50} \times 25$, CG stop cond: $10^{-6}$

| $\beta$ | start | # traj | acc. | $\langle e^{-\Delta H} \rangle$ | plaq. | $\langle \lvert W_3 \rvert \rangle$ | $\langle \overline{q} q \rangle$ |
|---|---|---|---|---|---|---|---|
| 5.35 | O | 100-800 | 0.87 | 1.01(1) | 0.4435(7) | 0.0189(8) | 0.00497(1) |
| 5.45 | O | 100-800 | 0.86 | 0.99(1) | 0.4630(7) | 0.0215(8) | 0.00522(1) |
| 5.55 | O | 300-800 | 0.86 | 1.00(1) | 0.487(1) | 0.032(3) | 0.00539(3) |
| 5.65 | D | 400-800 | 0.86 | 1.00(2) | 0.540(2) | 0.180(6) | 0.00457(4) |
| 5.75 | D | 300-800 | 0.85 | 0.99(1) | 0.5598(8) | 0.224(3) | 0.00445(1) |
| 5.85 | D | 200-800 | 0.89 | 1.011(8) | 0.5744(3) | 0.254(3) | 0.004409(5) |

Table 3: Run parameters for $\beta_c(m_0 = 1.65)$ search

vol: $8^3 \times 4$, $m_0 = 1.65$, $L_s = 12$, $m_f = 0.1$

HMC traj. len: $\frac{1}{50} \times 25$, CG stop cond: $10^{-6}$

| $\beta$ | start | # traj | acc. | $\langle e^{-\Delta H} \rangle$ | plaq. | $\langle \lvert W_3 \rvert \rangle$ | $\langle \overline{q} q \rangle$ |
|---|---|---|---|---|---|---|---|
| 5.25 | O | 200-800 | 0.82 | 0.97(2) | 0.4289(5) | 0.027(2) | 0.01000(2) |
| 5.35 | O | 400-800 | 0.68 | 0.98(4) | 0.451(3) | 0.035(4) | 0.01000(9) |
| 5.45 | D | 400-800 | 0.74 | 1.09(5) | 0.4769(8) | 0.049(7) | 0.00985(7) |
| 5.55 | D | 600-1200 | 0.80 | 1.00(3) | 0.531(1) | 0.175(7) | 0.00718(7) |
| 5.65 | D | 400-800 | 0.79 | 0.96(2) | 0.5507(9) | 0.216(4) | 0.00677(2) |
| 5.75 | D | 200-800 | 0.88 | 0.989(7) | 0.5663(4) | 0.243(3) | 0.00658(1) |

Table 4: Run parameters for $\beta_c(m_0 = 1.8)$ search

vol: $8^3 \times 4$, $m_0 = 1.8$, $L_s = 12$, $m_f = 0.1$

HMC traj. len: $\frac{1}{50} \times 25$, CG stop cond: $10^{-6}$

| $\beta$ | start | # traj | acc. | $\langle e^{-\Delta H} \rangle$ | plaq. | $\langle \lvert W_3 \rvert \rangle$ | $\langle \overline{q} q \rangle$ |
|---|---|---|---|---|---|---|---|
| 5.15 | O | 200-800 | 0.83 | 1.02(2) | 0.4191(8) | 0.029(1) | 0.01485(5) |
| 5.25 | O | 400-800 | 0.66 | 0.97(5) | 0.4381(6) | 0.038(2) | 0.01458(5) |
| 5.35 | O | 400-800 | 0.63 | 0.97(5) | 0.471(2) | 0.052(3) | 0.0134(2) |
| 5.45 | O | 400-800 | 0.76 | 1.01(3) | 0.515(2) | 0.161(4) | 0.0097(1) |
| 5.55 | D | 400-800 | 0.79 | 1.05(5) | 0.540(1) | 0.200(9) | 0.0088(1) |
| 5.65 | D | 200-800 | 0.89 | 1.01(2) | 0.5570(5) | 0.242(4) | 0.00828(2) |

Table 5: Run parameters for $\beta_c(m_0 = 1.9)$ search

vol: $8^3 \times 4$, $m_0 = 1.9$, $L_s = 12$, $m_f = 0.1$

CG stop cond: $10^{-6}$

| $\beta$ | start | traj. len. | # traj | acc. | $\langle e^{-\Delta H} \rangle$ | plaq. | $\langle \lvert W_3 \rvert \rangle$ | $\langle \overline{q}q \rangle$ |
|---|---|---|---|---|---|---|---|---|
| 5.0 | O | $\frac{1}{40} \times 20$ | 200-800 | 0.37 | 0.8(1) | 0.4002(8) | 0.032(2) | 0.01919(5) |
| 5.2 | O | $\frac{1}{40} \times 20$ | 400-800 | 0.43 | 1.2(3) | 0.437(1) | 0.032(2) | 0.01838(4) |
| 5.25 | O | $\frac{1}{50} \times 25$ | 400-800 | 0.65 | 1.10(9) | 0.452(1) | 0.049(6) | 0.0174(2) |
| 5.35 | D | $\frac{1}{50} \times 25$ | 600-1200 | 0.69 | 0.95(5) | 0.493(2) | 0.107(9) | 0.0135(4) |
| 5.45 | D | $\frac{1}{50} \times 25$ | 600-1200 | 0.74 | 1.01(4) | 0.528(1) | 0.197(4) | 0.01039(7) |
| 5.55 | D | $\frac{1}{50} \times 25$ | 400-830 | 0.82 | 1.00(1) | 0.5463(5) | 0.227(6) | 0.00974(4) |
| 5.65 | D | $\frac{1}{50} \times 25$ | 400-800 | 0.88 | 1.03(1) | 0.5613(8) | 0.248(5) | 0.00943(4) |

Table 6: Run parameters for $\beta_c(m_0 = 2.0)$ search

vol: $8^3 \times 4$, $m_0 = 2.0$, $L_s = 12$, $m_f = 0.1$

HMC traj. len: $\frac{1}{50} \times 25$, CG stop cond: $10^{-6}$

| $\beta$ | start | # traj | acc. | $\langle e^{-\Delta H} \rangle$ | plaq. | $\langle \lvert W_3 \rvert \rangle$ | $\langle \overline{q}q \rangle$ |
|---|---|---|---|---|---|---|---|
| 5.05 | O | 200-800 | 0.77 | 0.99(3) | 0.4192(8) | 0.035(1) | 0.02324(8) |
| 5.15 | O | 200-800 | 0.75 | 0.98(3) | 0.442(1) | 0.042(3) | 0.0215(2) |
| 5.25 | O | 200-1200 | 0.79 | 1.03(1) | 0.474(1) | 0.080(7) | 0.0181(3) |
| 5.35 | D | 200-800 | 0.83 | 1.00(2) | 0.5130(7) | 0.173(6) | 0.0130(2) |
| 5.45 | D | 200-800 | 0.87 | 1.02(2) | 0.5349(5) | 0.203(3) | 0.01157(4) |
| 5.55 | D | 200-800 | 0.85 | 1.01(1) | 0.5503(4) | 0.235(3) | 0.01099(2) |

Table 7: Run parameters for $\beta_c(m_0 = 2.15)$ search

vol: $8^3 \times 4$, $m_0 = 2.15$, $L_s = 12$, $m_f = 0.1$

HMC traj. len: $\frac{1}{50} \times 25$, CG stop cond: $10^{-6}$

| $\beta$ | start | # traj | acc. | $\langle e^{-\Delta H} \rangle$ | plaq. | $\langle \lvert W_3 \rvert \rangle$ | $\langle \overline{q} q \rangle$ |
|---|---|---|---|---|---|---|---|
| 4.85 | O | 200-800 | 0.69 | 0.95(3) | 0.4004(8) | 0.034(2) | 0.0323(2) |
| 4.95 | O | 200-800 | 0.72 | 0.97(3) | 0.419(2) | 0.040(2) | 0.0302(3) |
| 5.05 | O | 200-800 | 0.48 | 0.92(4) | 0.443(2) | 0.052(3) | 0.0272(5) |
| 5.15 | O | 200-1200 | 0.62 | 1.01(3) | 0.480(3) | 0.12(1) | 0.0203(7) |
| 5.25 | O | 400-800 | 0.70 | 0.97(5) | 0.5105(4) | 0.185(2) | 0.01559(8) |
| 5.35 | D | 400-800 | 0.69 | 1.01(4) | 0.529(1) | 0.216(6) | 0.0141(1) |
| 5.45 | D | 400-800 | 0.71 | 1.00(3) | 0.5453(7) | 0.230(4) | 0.01330(5) |

Table 8: Run parameters for $\beta_c(m_0 = 2.4)$ search

vol: $8^3 \times 4$, $m_0 = 2.4$, $L_s = 12$, $m_f = 0.1$

HMC traj. len: $\frac{1}{50} \times 25$, CG stop cond: $10^{-6}$

| $\beta$ | start | # traj | acc. | $\langle e^{-\Delta H} \rangle$ | plaq. | $\langle \lvert W_3 \rvert \rangle$ | $\langle \overline{q} q \rangle$ |
|---|---|---|---|---|---|---|---|
| 4.65 | O | 100-800 | 0.63 | 1.02(5) | 0.3953(6) | 0.046(3) | 0.0484(3) |
| 4.75 | O | 200-800 | 0.68 | 0.99(5) | 0.4156(9) | 0.054(3) | 0.0442(3) |
| 4.85 | O | 300-800 | 0.70 | 0.94(4) | 0.439(2) | 0.069(5) | 0.0380(6) |
| 4.95 | O | 200-800 | 0.77 | 1.02(4) | 0.4779(6) | 0.155(4) | 0.0257(2) |
| 5.05 | D | 200-800 | 0.80 | 1.01(2) | 0.4987(9) | 0.190(2) | 0.0220(2) |
| 5.15 | D | 200-800 | 0.84 | 1.01(3) | 0.5170(5) | 0.221(3) | 0.01962(7) |

Table 9: Fit of $\langle |W_3| \rangle = c_0 \{c_1 + \tanh[c_2(\beta - \beta_c)]\}$: $8^3 \times 4, L_s = 12, m_f = 0.1$

| $m_0$ | $\beta_c$ | $c_o$ | $c_1$ | $c_2$ | $N_{\rm dof}$ | $\chi^2/N_{\rm dof}$ |
|---|---|---|---|---|---|---|
| 1.15 | 5.722(5) | 0.122(1) | 1.126(7) | 9.8(5) | 2 | 14.50 |
| 1.4 | 5.627(4) | 0.110(1) | 1.180(7) | 17(1) | 2 | 21.39 |
| 1.65 | 5.524(6) | 0.107(2) | 1.24(2) | 10(1) | 2 | 9.60 |
| 1.8 | 5.431(4) | 0.105(2) | 1.29(1) | 11.7(8) | 2 | 11.07 |
| 1.9 | 5.386(6) | 0.107(3) | 1.27(2) | 9.9(8) | 3 | 2.61 |
| 2.0 | 5.327(7) | 0.107(3) | 1.27(3) | 6.7(6) | 2 | 10.33 |
| 2.15 | 5.179(6) | 0.098(2) | 1.35(3) | 8.3(6) | 3 | 1.13 |
| 2.4 | 4.934(7) | 0.091(4) | 1.46(5) | 7.2(6) | 2 | 14.02 |

Table 10: Fit of $\langle \overline{q}q \rangle = c_0 \{c_1 + \tanh[c_2(\beta - \beta_c)]\}$: $8^3 \times 4, L_s = 12, m_f = 0.1$

| $m_0$ | $\beta_c$ | $c_o$ | $c_1$ | $c_2$ | $N_{\rm dof}$ | $\chi^2/N_{\rm dof}$ |
|---|---|---|---|---|---|---|
| 1.65 | 5.524(6) | -0.00170(1) | -4.89(3) | 18(2) | 2 | 38.28 |
| 1.8 | 5.398(4) | -0.00331(5) | -3.50(3) | 10.6(7) | 2 | 4.90 |
| 1.9 | 5.330(3) | -0.00488(3) | -2.94(2) | 9.1(2) | 3 | 2.85 |
| 2.0 | 5.256(5) | -0.00648(9) | -2.67(3) | 7.5(3) | 2 | 7.12 |
| 2.15 | 5.103(6) | -0.0099(1) | -2.32(2) | 6.5(3) | 3 | 3.36 |
| 2.4 | 4.864(4) | -0.0154(3) | -2.24(3) | 6.9(3) | 2 | 14.96 |

Table 11: Run parameters for $8^3 \times 4, \beta = 5.2, m_0 = 1.9$ confined phase study

| $m_f$ | $L_s$ | traj. len. | # traj. | acc. | $\langle e^{-\Delta H} \rangle$ | plaq. | $\langle \lvert W_3 \rvert \rangle$ | $\langle \overline{q}q \rangle$ |
|---|---|---|---|---|---|---|---|---|
| 0.02 | 4 | $\frac{1}{64} \times 32$ | 200-800 | 0.94 | 1.002(8) | 0.500(3) | 0.16(1) | 0.0250(7) |
| | 6 | $\frac{1}{64} \times 32$ | 200-800 | 0.92 | 1.00(1) | 0.468(2) | 0.080(4) | 0.0167(3) |
| | 8 | $\frac{1}{64} \times 32$ | 400-800 | 0.89 | 0.98(1) | 0.456(2) | 0.061(2) | 0.0133(2) |
| | 10 | $\frac{1}{64} \times 32$ | 200-2000 | 0.86 | 0.995(8) | 0.4460(9) | 0.048(2) | 0.0124(1) |
| | 12 | $\frac{1}{64} \times 32$ | 200-2000 | 0.84 | 1.01(1) | 0.4428(6) | 0.048(2) | 0.01123(7) |
| | 16 | $\frac{1}{64} \times 32$ | 550-2000 | 0.75 | 0.98(2) | 0.4388(9) | 0.049(2) | 0.00987(9) |
| | 24 | $\frac{1}{100} \times 50$ | 350-2000 | 0.73 | 0.95(2) | 0.4359(7) | 0.047(3) | 0.0088(1) |
| | 32 | $\frac{1}{100} \times 50$ | 300-2000 | 0.72 | 1.03(2) | 0.4317(7) | 0.045(2) | 0.00835(7) |
| | 40 | $\frac{1}{128} \times 64$ | 300-1350 | 0.73 | 1.02(3) | 0.4342(6) | 0.044(2) | 0.00772(8) |
| 0.06 | 8 | $\frac{1}{50} \times 25$ | 200-950 | 0.83 | 0.98(1) | 0.450(1) | 0.046(3) | 0.0176(2) |
| | 16 | $\frac{1}{64} \times 32$ | 200-820 | 0.84 | 0.99(2) | 0.4361(8) | 0.045(3) | 0.0135(1) |
| 0.1 | 4 | $\frac{1}{40} \times 20$ | 300-800 | 0.82 | 1.00(2) | 0.463(2) | 0.058(3) | 0.0375(4) |
| | 6 | $\frac{1}{50} \times 25$ | 300-800 | 0.89 | 1.00(2) | 0.454(3) | 0.048(5) | 0.0246(4) |
| | 8 | $\frac{1}{40} \times 20$ | 300-800 | 0.57 | 0.89(5) | 0.4437(8) | 0.040(3) | 0.02109(7) |
| | 10 | $\frac{1}{50} \times 25$ | 200-800 | 0.83 | 1.00(3) | 0.4405(6) | 0.036(2) | 0.01927(9) |
| | 12 | $\frac{1}{40} \times 20$ | 400-800 | 0.43 | 1.2(3) | 0.437(1) | 0.032(2) | 0.01838(4) |
| | 16 | $\frac{1}{64} \times 32$ | 200-800 | 0.80 | 0.98(2) | 0.435(2) | 0.035(2) | 0.01709(9) |
| | 24 | $\frac{1}{64} \times 32$ | 200-800 | 0.72 | 0.94(2) | 0.433(1) | 0.033(2) | 0.01596(7) |
| | 32 | $\frac{1}{100} \times 50$ | 200-800 | 0.82 | 0.99(2) | 0.4305(5) | 0.037(2) | 0.01547(7) |
| | 40 | $\frac{1}{100} \times 50$ | 200-800 | 0.78 | 1.00(5) | 0.432(1) | 0.035(2) | 0.01524(5) |
| 0.14 | 8 | $\frac{1}{40} \times 20$ | 200-860 | 0.63 | 1.03(6) | 0.4433(7) | 0.033(5) | 0.0241(1) |
| | 16 | $\frac{1}{64} \times 32$ | 200-800 | 0.85 | 1.03(2) | 0.433(1) | 0.030(1) | 0.02017(6) |
| 0.18 | 8 | $\frac{1}{40} \times 20$ | 200-1200 | 0.70 | 1.02(3) | 0.4410(7) | 0.030(1) | 0.02686(7) |
| | 16 | $\frac{1}{64} \times 32$ | 200-800 | 0.84 | 0.98(2) | 0.432(1) | 0.033(1) | 0.02309(5) |

Table 12: Fit of $\langle\overline{q}q\rangle = c_0 + c_1 m_f + c_2 m_f^2$, $8^3 \times 4, \beta = 5.2, m_0 = 1.9$

| $L_s$ | fit range | $c_0$ | $c_1$ | $c_2$ | $N_{\rm dof}$ | $\chi^2/N_{\rm dof}$ |
|---|---|---|---|---|---|---|
| 8 | 0.02–0.1 | 0.0117(2) | 0.095(2) | — | 1 | 3.67 |
| | 0.02–0.14 | 0.0122(2) | 0.088(2) | — | 2 | 9.89 |
| | 0.02–0.18 | 0.0130(1) | 0.0781(9) | — | 3 | 20.48 |
| | 0.02–0.14 | 0.0111(3) | 0.118(7) | -0.18(4) | 1 | 0.23 |
| | 0.02–0.18 | 0.0112(3)[a] | 0.114(5) | -0.15(2) | 2 | 0.37 |
| 10 | 0.02–0.1 | 0.0107(2)[a] | 0.086(2) | — | 0 | — |
| 12 | 0.02–0.1 | 0.00944(9)[a] | 0.089(1) | — | 0 | — |
| 16 | 0.02–0.1 | 0.0081(1) | 0.090(2) | — | 1 | 0.24 |
| | 0.02–0.14 | 0.00830(9) | 0.0855(9) | — | 2 | 6.68 |
| | 0.02–0.18 | 0.00857(8) | 0.0815(6) | — | 3 | 16.38 |
| | 0.02–0.14 | 0.0079(2) | 0.101(5) | -0.10(3) | 1 | 0.73 |
| | 0.02–0.18 | 0.0079(1)[a] | 0.100(3) | -0.09(1) | 2 | 0.43 |
| 24 | 0.02–0.1 | 0.0069(1)[a] | 0.090(2) | — | 0 | — |
| 32 | 0.02–0.1 | 0.00656(9)[a] | 0.089(1) | — | 0 | — |
| 40 | 0.02–0.1 | 0.00584(9)[a] | 0.094(1) | — | 0 | — |
| $\infty$[b] | 0.02–0.1 | 0.0060(1) | 0.092(1) | — | 0 | — |

[a] Shown in figure 21 and used as input to fits in table 13.

[b] Used fitted values from table 13 as input.

Table 13: Fit of $\langle\overline{q}q\rangle = c_0 + c_1 \exp(-c_2 L_s)$, $8^3 \times 4, \beta = 5.2, m_0 = 1.9$

| $m_f$ | fit range | $c_0$ | $c_1$ | $c_2$ | $N_{\rm dof}$ | $\chi^2/N_{\rm dof}$ |
|---|---|---|---|---|---|---|
| 0.0[a] | 8–40 | 0.0059(1) | 0.014(1) | 0.11(1) | 4 | 6.62 |
| | 10–40 | 0.0060(1) | 0.016(2) | 0.13(1) | 3 | 7.90 |
| | 12–40 | 0.0058(2) | 0.012(2) | 0.10(1) | 2 | 9.41 |
| | 16–40 | 0.003(4) | 0.007(3) | 0.02(2) | 1 | 3.16 |
| 0.02 | 8–40 | 0.00779(8)[b] | 0.014(1) | 0.116(8) | 4 | 5.55 |
| | 10–40 | 0.00780(9) | 0.014(1) | 0.118(9) | 3 | 7.37 |
| | 12–40 | 0.0076(1) | 0.011(1) | 0.10(1) | 2 | 7.74 |
| | 16–40 | 0.0065(9) | 0.0064(4) | 0.04(2) | 1 | 4.67 |
| 0.1 | 8–40 | 0.01527(4) | 0.0188(8) | 0.149(5) | 4 | 5.14 |
| | 10–40 | 0.01514(6)[b] | 0.013(1) | 0.119(8) | 3 | 0.41 |
| | 12–40 | 0.01513(7) | 0.013(1) | 0.117(9) | 2 | 0.56 |
| | 16–40 | 0.0151(1) | 0.010(3) | 0.101(2) | 1 | 0.03 |

[a] Used fitted values from table 12 as input.

[b] Used as input to fits in table 12.

Table 14: Run parameters for $8^3 \times 4, \beta = 5.45, m_0 = 1.9$ deconfined phase study

| $m_f$ | $L_s$ | traj. len. | # traj. | acc. | $\left\langle e^{-\Delta H} \right\rangle$ | plaq. | $\langle \lvert W_3 \rvert \rangle$ | $\langle \overline{q} q \rangle$ |
|---|---|---|---|---|---|---|---|---|
| 0.02 | 8 | $\frac{1}{64} \times 32$ | 200-800 | 0.91 | 1.005(7) | 0.5376(7) | 0.226(4) | 0.00415(6) |
| | 10 | $\frac{1}{64} \times 32$ | 200-1000 | 0.91 | 0.992(8) | 0.5328(6) | 0.207(4) | 0.00319(5) |
| | 12 | $\frac{1}{64} \times 32$ | 200-800 | 0.95 | 1.009(9) | 0.5300(4) | 0.202(5) | 0.00270(3) |
| | 16 | $\frac{1}{64} \times 32$ | 200-800 | 0.90 | 1.02(1) | 0.5266(8) | 0.199(4) | 0.00237(6) |
| | 24 | $\frac{1}{64} \times 32$ | 400-1200 | 0.86 | 0.98(2) | 0.5257(7) | 0.187(3) | 0.00216(6) |
| | 32 | $\frac{1}{100} \times 50$ | 400-800 | 0.94 | 1.00(2) | 0.524(2) | 0.180(5) | 0.00209(5) |
| 0.06 | 8 | $\frac{1}{50} \times 25$ | 200-1000 | 0.86 | 0.99(3) | 0.536(1) | 0.217(3) | 0.0080(1) |
| | 10 | $\frac{1}{64} \times 32$ | 200-1000 | 0.92 | 0.994(7) | 0.5313(6) | 0.203(4) | 0.00704(5) |
| | 12 | $\frac{1}{64} \times 32$ | 200-1000 | 0.89 | 1.013(8) | 0.5286(8) | 0.195(4) | 0.00666(5) |
| | 16 | $\frac{1}{64} \times 32$ | 400-800 | 0.76 | 1.02(4) | 0.525(2) | 0.192(4) | 0.00637(7) |
| | 24 | $\frac{1}{64} \times 32$ | 300-1000 | 0.84 | 1.00(1) | 0.521(2) | 0.174(6) | 0.00617(9) |
| | 32 | $\frac{1}{64} \times 32$ | 500-1000 | 0.80 | 1.00(2) | 0.525(2) | 0.189(3) | 0.00592(4) |
| 0.1 | 8 | $\frac{1}{50} \times 25$ | 300-800 | 0.83 | 0.98(2) | 0.5336(6) | 0.211(4) | 0.01174(4) |
| | 10 | $\frac{1}{50} \times 25$ | 300-990 | 0.88 | 0.99(1) | 0.5310(9) | 0.200(2) | 0.01075(5) |
| | 12 | $\frac{1}{50} \times 25$ | 600-1200 | 0.74 | 1.01(4) | 0.528(1) | 0.197(4) | 0.01838(4) |
| | 16 | $\frac{1}{64} \times 32$ | 400-800 | 0.79 | 1.01(3) | 0.523(1) | 0.170(5) | 0.0103(1) |
| | 24 | $\frac{1}{64} \times 32$ | 400-2000 | 0.86 | 0.991(8) | 0.512(1) | 0.170(8) | 0.0102(1) |
| | 32 | $\frac{1}{64} \times 32$ | 300-1000 | 0.81 | 0.98(2) | 0.519(1) | 0.159(5) | 0.01011(9) |
| 0.14 | 8 | $\frac{1}{50} \times 25$ | 200-800 | 0.83 | 1.01(1) | 0.533(1) | 0.210(3) | 0.01531(9) |
| | 16 | $\frac{1}{64} \times 32$ | 600-1200 | 0.76 | 0.98(2) | 0.520(1) | 0.159(9) | 0.0143(1) |
| 0.18 | 8 | $\frac{1}{50} \times 25$ | 400-800 | 0.81 | 1.03(2) | 0.5314(6) | 0.202(4) | 0.01884(5) |
| | 16 | $\frac{1}{64} \times 32$ | 600-1200 | 0.78 | 0.94(2) | 0.515(1) | 0.141(8) | 0.0182(2) |

Table 15: Fit of $\langle \overline{q}q \rangle = c_0 + c_1 m_f + c_2 m_f^2$, $8^3 \times 4, \beta = 5.45, m_0 = 1.9$

| $L_s$ | fit range | $c_0$ | $c_1$ | $c_2$ | $N_{\rm dof}$ | $\chi^2/N_{\rm dof}$ |
|---|---|---|---|---|---|---|
| 8 | 0.02–0.1 | 0.00227(7) | 0.0948(9) | — | 1 | 0.62 |
| | 0.02–0.18 | 0.00219(9)[a] | 0.099(2) | -0.037(9) | 2 | 0.10 |
| | | 0.00246(6) | 0.0915(5) | — | 3 | 5.80 |
| 10 | 0.02–0.1 | 0.00131(6)[a] | 0.0947(9) | — | 1 | 1.23 |
| 12 | 0.02–0.1 | 0.00077(4)[a] | 0.0968(8) | — | 1 | 3.85 |
| 16 | 0.02–0.1 | 0.00039(8) | 0.100(2) | — | 1 | 0.09 |
| | | — | 0.1060(8) | — | 2 | 12.86 |
| | 0.02–0.18 | 0.0004(1) | 0.100(3) | -0.01(2) | 2 | 0.02 |
| | | 0.00040(6)[a] | 0.0992(8) | — | 3 | 0.07 |
| | | — | 0.111(1) | -0.06(1) | 3 | 4.81 |
| 24 | 0.02–0.1 | 0.00016(8)[a] | 0.100(2) | — | 1 | 0.01 |
| | | — | 0.103(1) | -0.07(3) | 1 | 0.83 |
| | | — | 0.103(1) | — | 2 | 2.20 |
| 32 | 0.02–0.1 | — | 0.100(5) | — | 2 | 3.99 |
| | | 0.00006(6)[a] | 0.099(1) | — | 1 | 7.11 |
| | | — | 0.099(2) | 0.02(2) | 1 | 7.40 |
| $\infty$[b] | 0.02–0.1 | — | 0.1012(4) | — | 2 | 6.90 |
| | | 0.00011(5) | 0.0995(8) | — | 1 | 8.45 |

[a] Shown in figure 23 and used as input to fits in table 16.

[b] Used fitted values from table 16 as input.

Table 16: Fit of $\langle \overline{q}q \rangle = c_0 + c_1 \exp(-c_2 L_s)$, $8^3 \times 4, \beta = 5.45, m_0 = 1.9$

| $m_f$ | fit range | $c_0$ | $c_1$ | $c_2$ | $N_{\rm dof}$ | $\chi^2/N_{\rm dof}$ |
|---|---|---|---|---|---|---|
| 0.0[a] | 8–32 | 0.00010(5) | 0.019(3) | 0.27(2) | 3 | 0.76 |
| | | — | 0.015(2) | 0.24(1) | 4 | 1.64 |
| | 10–32 | 0.00013(5) | 0.02(1) | 0.30(4) | 2 | 1.45 |
| | | — | 0.011(3) | 0.22(2) | 3 | 1.74 |
| | 12–32 | — | 0.005(2) | 0.15(3) | 2 | 0.22 |
| | | 0.00014(5) | 0.03(5) | 0.3(1) | 1 | 4.32 |
| 0.02 | 8–32 | 0.00213(4)[b] | 0.025(4) | 0.31(2) | 3 | 1.07 |
| | 10–32 | 0.00212(4) | 0.018(6) | 0.28(4) | 2 | 1.24 |
| | 12–32 | 0.00208(6) | 0.005(3) | 0.18(6) | 1 | 0.10 |
| 0.06 | 8–32 | 0.00599(4)[b] | 0.015(3) | 0.26(2) | 3 | 4.84 |
| | 10–32 | 0.00591(6) | 0.005(1) | 0.15(3) | 2 | 2.05 |
| | 12–32 | 0.00598(5) | 0.01(1) | 0.24(7) | 1 | 8.04 |
| 0.1 | 8–32 | 0.01016(6)[b] | 0.08(3) | 0.48(6) | 3 | 0.42 |
| | 10–32 | 0.01015(7) | 0.04(7) | 0.4(2) | 2 | 0.58 |
| | 12–32 | 0.0101(1) | 0.002(6) | 0.2(3) | 1 | 0.30 |

[a] Used fitted values from table 15 as input.

[b] Used as input to fits in table 15.

Table 17: Run parameters for transition study: $8^3 \times 4, m_0 = 1.9, L_s = 24, m_f = 0.02$

| $\beta$ | start | traj. len. | # traj. | acc. | $\langle e^{-\Delta H} \rangle$ | plaq. | $\langle \lvert W_3 \rvert \rangle$ | $\langle \overline{q}q \rangle$ |
|---|---|---|---|---|---|---|---|---|
| 5.2 | O | $\frac{1}{100} \times 50$ | 300–2000 | 0.72 | 0.95(2) | 0.4359(6) | 0.046(2) | 0.0087(1) |
| 5.275 | O | $\frac{1}{100} \times 50$ | 200–1000 | 0.83 | 1.01(2) | 0.459(1) | 0.068(4) | 0.0069(2) |
| 5.325 | D | $\frac{1}{100} \times 50$ | 200–1150 | 0.89 | 1.01(1) | 0.480(3) | 0.10(1) | 0.0050(4) |
| 5.45 | D | $\frac{1}{64} \times 32$ | 400–1200 | 0.86 | 0.98(2) | 0.5257(7) | 0.187(3) | 0.00216(6) |

Table 18: Run parameters for transition study: $16^3 \times 4, m_0 = 1.9, L_s = 24, m_f = 0.02$

HMC traj. len: $\frac{1}{128} \times 64$, CG stop cond: $10^{-6}$

| $\beta$ | start | # traj. | acc. | $\langle e^{-\Delta H} \rangle$ | plaq. | $\langle \lvert W_3 \rvert \rangle$ | $\langle \overline{q}q \rangle$ |
|---|---|---|---|---|---|---|---|
| 5.25 | D | 140–440 | 0.69 | 1.01(6) | 0.4465(2) | 0.046(2) | 0.0087(1) |
| | O | 350–650 | 0.74 | 0.99(5) | 0.4475(3) | 0.051(2) | 0.00814(4) |
| 5.275 | D | 360–660 | 0.70 | 0.92(5) | 0.4565(5) | 0.062(2) | 0.00737(4) |
| | O | 470–770 | 0.71 | 0.93(5) | 0.4561(3) | 0.061(2) | 0.00747(4) |
| 5.3 | D | 1100–1400 | 0.72 | 1.05(4) | 0.4656(8) | 0.074(2) | 0.0066(1) |
| | O | 720–1020 | 0.75 | 1.06(4) | 0.4683(6) | 0.077(2) | 0.00629(7) |
| 5.325 | D | 490–790 | 0.82 | 1.00(3) | 0.4800(6) | 0.096(2) | 0.00506(6) |
| | O | 670–970 | 0.77 | 0.96(3) | 0.480(1) | 0.102(4) | 0.0049(3) |
| 5.35 | D | 650–950 | 0.86 | 1.04(3) | 0.4924(9) | 0.124(3) | 0.0037(1) |
| | O | 200–500 | 0.84 | 1.03(3) | 0.4928(4) | 0.127(2) | 0.00366(5) |

Table 19: Run parameters for $8^3 \times 4$ improved gauge action transition study

vol: $8^3 \times 4$, $c_1 = -0.331$, $m_0 = 1.9$, $L_s = 24$, $m_f = 0.02$

HMC traj. len: $\frac{1}{100} \times 50$, CG stop cond: $10^{-6}$

| $\beta$ | start | # traj. | acc. | $\langle e^{-\Delta H} \rangle$ | plaq. | $\langle \lvert W_3 \rvert \rangle$ | $\langle \overline{q} q \rangle$ |
|---|---|---|---|---|---|---|---|
| 1.7 | D | 70–170 | 0.77 | 1.00(5) | 0.424(1) | 0.032(2) | 0.01067(9) |
| | O | 70–170 | 0.76 | 0.96(4) | 0.423(1) | 0.034(2) | 0.0104(2) |
| 1.8 | D | 100–200 | 0.86 | 1.07(5) | 0.4620(9) | 0.037(2) | 0.0097(2) |
| | O | 100–200 | 0.78 | 0.93(4) | 0.462(1) | 0.033(4) | 0.0096(2) |
| 1.9 | D | 130–230 | 0.88 | 0.98(5) | 0.507(2) | 0.057(3) | 0.0066(2) |
| | O | 130–230 | 0.89 | 1.11(6) | 0.5075(9) | 0.064(5) | 0.0064(2) |
| 2.0 | D | 160–260 | 0.93 | 0.98(3) | 0.5500(8) | 0.123(6) | 0.0028(1) |
| | O | 160–260 | 0.96 | 0.99(3) | 0.5502(9) | 0.128(3) | 0.00245(5) |
| 2.1 | D | 200–400 | 0.94 | 0.98(1) | 0.5824(6) | 0.17(1) | 0.0021(2) |
| | O | 200–400 | 0.94 | 0.99(3) | 0.5806(7) | 0.17(1) | 0.0023(2) |
| 2.2 | D | 140–240 | 0.95 | 1.01(1) | 0.6054(4) | 0.20(2) | 0.00191(3) |
| | O | 140–240 | 0.93 | 0.99(1) | 0.6064(5) | 0.212(9) | 0.00187(1) |

Table 20: Run parameters for $16^3 \times 4$ improved gauge action transition study

vol: $16^3 \times 4$, $c_1 = -0.331$, $m_0 = 1.9$, $L_s = 24$, $m_f = 0.02$

HMC traj. len: $\frac{1}{128} \times 64$, CG stop cond: $10^{-6}$

| $\beta$ | start | # traj. | acc. | $\langle e^{-\Delta H} \rangle$ | plaq. | $\langle \lvert W_3 \rvert \rangle$ | $\langle \overline{q} q \rangle$ |
|---|---|---|---|---|---|---|---|
| 1.85 | D | 150–270 | 0.75 | 1.0(1) | 0.4848(4) | 0.044(1) | 0.00843(6) |
| | O | 160–300 | 0.73 | 1.09(9) | 0.4861(4) | 0.044(2) | 0.00823(7) |
| 1.9 | D | 200–300 | 0.71 | 0.96(6) | 0.5079(7) | 0.063(2) | 0.0064(1) |
| | O | 200–300 | 0.78 | 0.99(3) | 0.5095(3) | 0.0658(8) | 0.00598(7) |
| 1.95 | D | 220–520 | 0.76 | 1.00(2) | 0.5313(3) | 0.098(2) | 0.00378(5) |
| | O | 150–450 | 0.83 | 1.04(4) | 0.5321(3) | 0.107(2) | 0.00362(4) |
| 2.0 | D | 200–300 | 0.93 | 1.08(3) | 0.5506(3) | 0.1242(6) | 0.00260(7) |
| | O | 200–300 | 0.90 | 1.05(3) | 0.5505(3) | 0.127(2) | 0.00260(5) |

Table 21: Valence $\langle \overline{q}q \rangle$ and $\chi_\pi$: $8^3 \times 4, \beta = 5.2, m_0 = 1.9, L_s = 10\text{–}16, m_f = 0.02$

| | | $\langle \overline{q}q \rangle$ | | | $\chi_\pi$ | | |
|---|---|---|---|---|---|---|---|
| $L_s^{(\mathrm{dyn})}$ | $m_f^{(\mathrm{val})}$ | # traj | # meas | avg | # traj | # meas | avg |
| 10 | 0.02 | 200–2000 | 1800 | 0.0124(1) | 800–2000 | 240 | 0.130(1) |
| | 0.06 | | 360 | 0.0156(1) | | | 0.1202(7) |
| | 0.1 | | | 0.0186(1) | | | 0.1130(6) |
| | 0.14 | | | 0.0215(1) | | | 0.1071(5) |
| | 0.18 | | | 0.02432(9) | | | 0.1022(4) |
| | 0.22 | | | 0.02695(8) | | | 0.0979(4) |
| 12 | 0.02 | 200–2000 | 1800 | 0.01123(7) | 800–2000 | 240 | 0.129(1) |
| | 0.06 | | 360 | 0.01448(8) | | | 0.1193(7) |
| | 0.1 | | | 0.01759(7) | | | 0.1120(6) |
| | 0.14 | | | 0.02056(6) | | | 0.1061(4) |
| | 0.18 | | | 0.02338(5) | | | 0.1012(4) |
| | 0.22 | | | 0.02608(5) | | | 0.0970(3) |
| 16 | 0.02 | 550–2000 | 1450 | 0.00987(9) | 800–2000 | 240 | 0.134(1) |
| | 0.06 | | 290 | 0.01318(8) | | | 0.123(1) |
| | 0.1 | | | 0.01639(7) | | | 0.1146(8) |
| | 0.14 | | | 0.01945(6) | | | 0.1082(7) |
| | 0.18 | | | 0.02236(6) | | | 0.1029(6) |
| | 0.22 | | | 0.02513(5) | | | 0.0985(5) |

Table 22: Valence $\langle \overline{q}q \rangle$ and $\chi_\pi$: $8^3 \times 4, \beta = 5.2, m_0 = 1.9, L_s = 24\text{–}40, m_f = 0.02$

| | | $\langle \overline{q}q \rangle$ | | | $\chi_\pi$ | | |
|---|---|---|---|---|---|---|---|
| $L_s^{(\mathrm{dyn})}$ | $m_f^{(\mathrm{val})}$ | # traj | # meas | avg | # traj | # meas | avg |
| 24 | 0.02 | 350–2000 | 1650 | 0.0088(1) | 800–2000 | 240 | 0.141(2) |
| | 0.06 | | 330 | 0.0122(1) | | | 0.127(1) |
| | 0.1 | | | 0.01550(9) | | | 0.1177(9) |
| | 0.14 | | | 0.01863(8) | | | 0.1108(7) |
| | 0.18 | | | 0.02161(7) | | | 0.1052(5) |
| | 0.22 | | | 0.02443(5) | | | 0.1005(4) |
| 32 | 0.02 | 300–2000 | 1700 | 0.00835(7) | 800–2000 | 240 | 0.155(3) |
| | 0.06 | | 340 | 0.01169(8) | | | 0.135(2) |
| | 0.1 | | | 0.01504(8) | | | 0.123(2) |
| | 0.14 | | | 0.01822(7) | | | 0.114(1) |
| | 0.18 | | | 0.02124(6) | | | 0.108(1) |
| | 0.22 | | | 0.02410(6) | | | 0.103(1) |
| 40 | 0.02 | 300–1350 | 1050 | 0.00772(8) | 300–1350 | 210 | 0.157(3) |
| | 0.06 | | 210 | 0.0113(1) | | | 0.135(2) |
| | 0.1 | | | 0.0147(1) | | | 0.123(1) |
| | 0.14 | | | 0.01799(7) | | | 0.114(1) |
| | 0.18 | | | 0.02106(6) | | | 0.1075(9) |
| | 0.22 | | | 0.02396(6) | | | 0.1022(7) |

Table 23: Valence $m_{\rm res}$ and $b_0$: $8^3 \times 4, \beta = 5.2, m_0 = 1.9, m_f = 0.02$

| $L_s$ | jknf blks | $m_{\rm res}$ | $-b_0$ | $\chi^2$/dof |
|---|---|---|---|---|
| 10 | 10 | 0.149(5) | 0.0094(5) | 0.75(42) |
| | 15 | 0.149(5) | 0.0094(5) | 0.78(41) |
| | 20 | 0.149(4) | 0.0094(4) | 0.78(44) |
| 12 | 10 | 0.129(2) | 0.0080(2) | 1.63(44) |
| | 15 | 0.129(2) | 0.0080(4) | 1.68(59) |
| | 20 | 0.129(2) | 0.0080(3) | 1.70(70) |
| 16 | 10 | 0.113(3) | 0.0080(4) | 1.14(45) |
| | 15 | 0.113(3) | 0.0080(4) | 1.20(37) |
| | 20 | 0.113(4) | 0.0080(5) | 1.21(46) |
| 24 | 10 | 0.095(2) | 0.0075(3) | 1.52(74) |
| | 15 | 0.095(3) | 0.0075(3) | 1.57(68) |
| | 20 | 0.095(3) | 0.0075(3) | 1.61(73) |
| 32 | 10 | 0.078(2) | 0.0068(5) | 0.71(38) |
| | 15 | 0.078(2) | 0.0069(4) | 0.72(39) |
| | 20 | 0.078(2) | 0.0069(4) | 0.72(42) |
| 40 | 10 | 0.059(3) | 0.0048(3) | 1.70(93) |
| | 15 | 0.059(2) | 0.0048(3) | 1.74(1.47) |
| | 20 | 0.060(2) | 0.0048(3) | 1.74(1.56) |

Table 24: Valence $m_{\rm res}$ and $b_0$ for scale setting simulations, $m_0 = 1.9$

| gauge action | Vol | $\beta$ | $L_s$ | $m_f$ | jknf blks | $m_{\rm res}$ | $-b_0$ | $\chi^2$/dof |
|---|---|---|---|---|---|---|---|---|
| W | 8×32 | 5.325 | 24 | 0.02 | 10 | 0.057(2) | 0.0045(2) | 8.4(3.9) |
| | | | | | 20 | 0.057(2) | 0.0046(2) | 8.8(3.9) |
| | | | | 0.06 | 10 | 0.059(3) | 0.0045(3) | 2.1(6) |
| | | | | | 20 | 0.059(2) | 0.0045(2) | 2.2(1.0) |
| R | 8×32 | 1.9 | 24 | 0.02 | 10 | 0.038(2) | 0.0027(1) | 8.6(2.2) |
| | | | | | 20 | 0.038(2) | 0.0027(2) | 9.1(2.8) |
| | | 2.0 | 24 | 0.02 | 10 | 0.016(2) | 0.0014(2) | 6.8(2.6) |
| | | | | | 20 | 0.016(3) | 0.0015(4) | 7.0(5.1) |
| | | | | 0.06 | 10 | 0.017(2) | 0.0015(3) | 1.6(8) |
| | | | | | 20 | 0.017(2) | 0.0015(3) | 1.6(8) |

# Figures

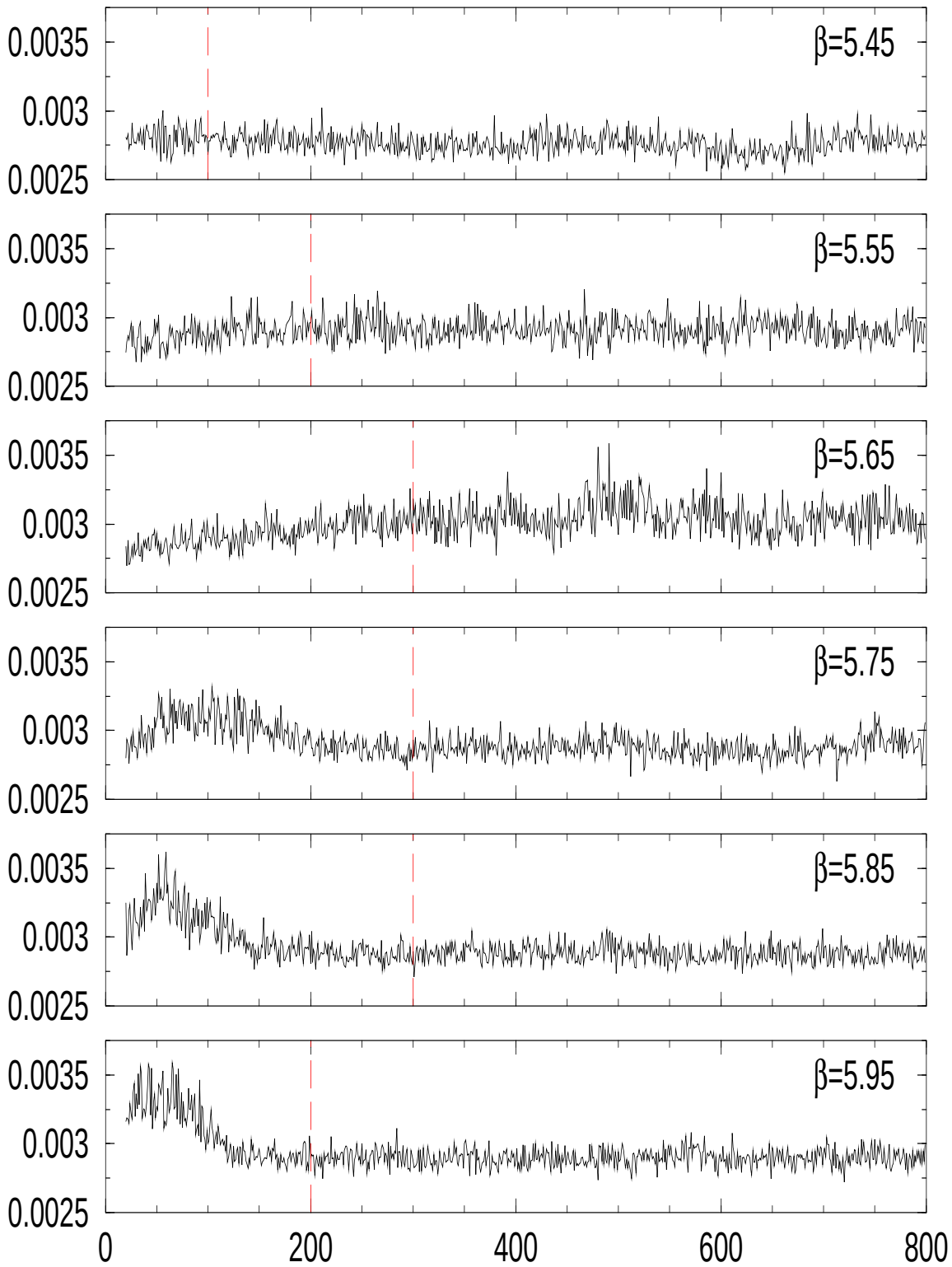


Figure 1: $\langle \overline{q}q \rangle$ evol: $8^3 \times 4, m_0 = 1.15, L_s = 12, m_f = 0.1$

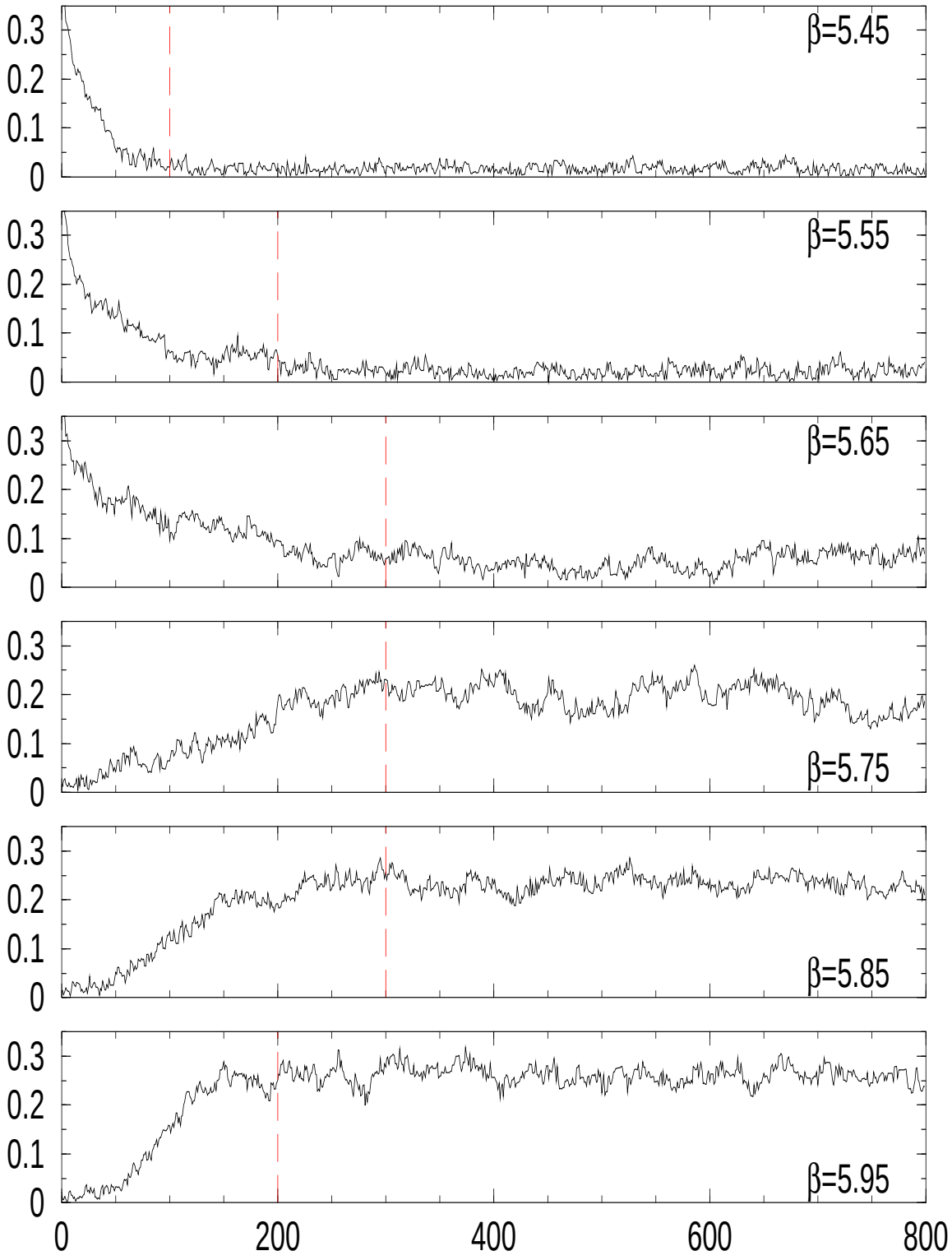


Figure 2: $\langle |W_3| \rangle$ evol: $8^3 \times 4, m_0 = 1.15, L_s = 12, m_f = 0.1$

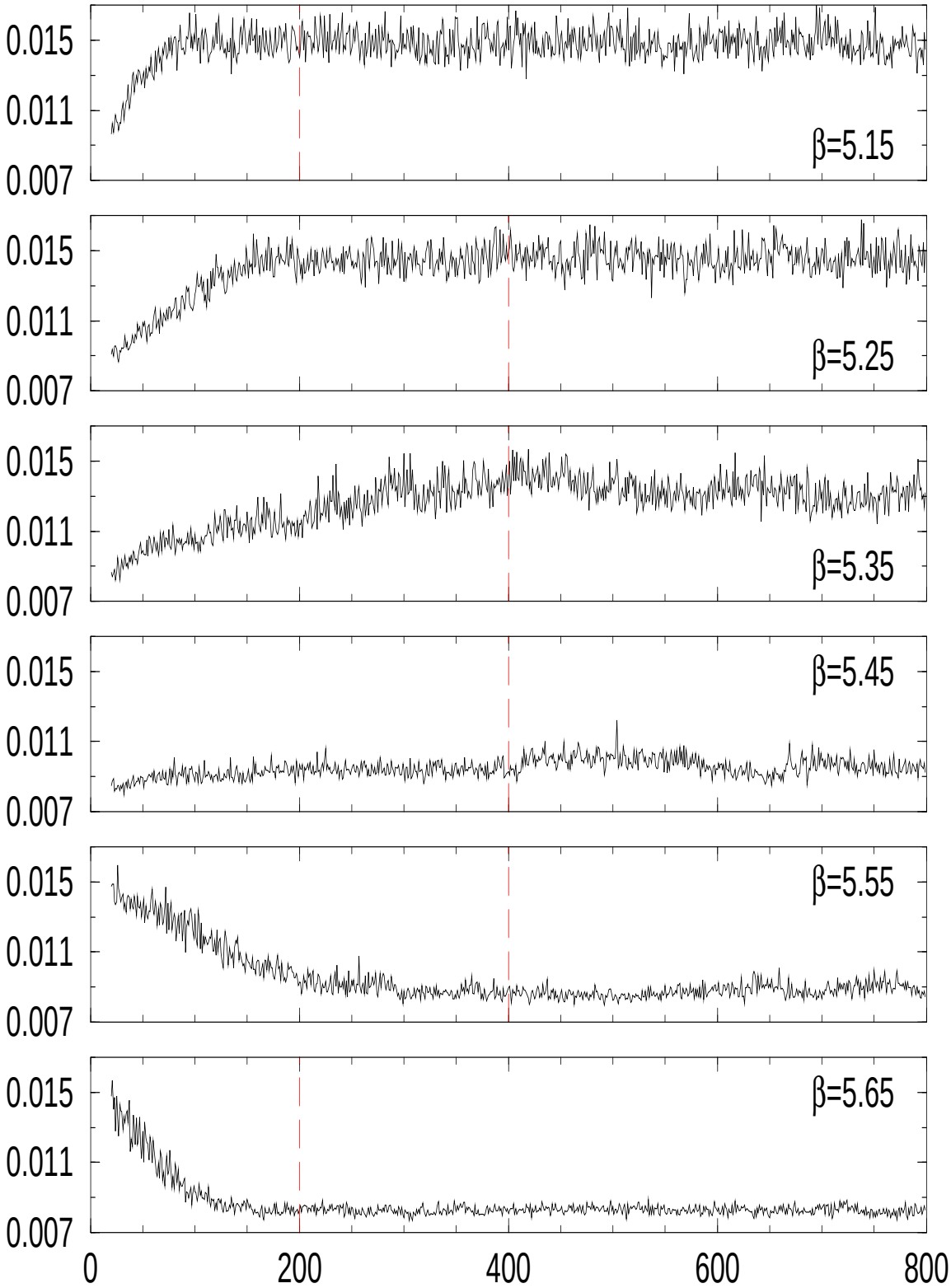


Figure 3: $\langle \overline{q}q \rangle$ evol: $8^3 \times 4, m_0 = 1.4, L_s = 12, m_f = 0.1$

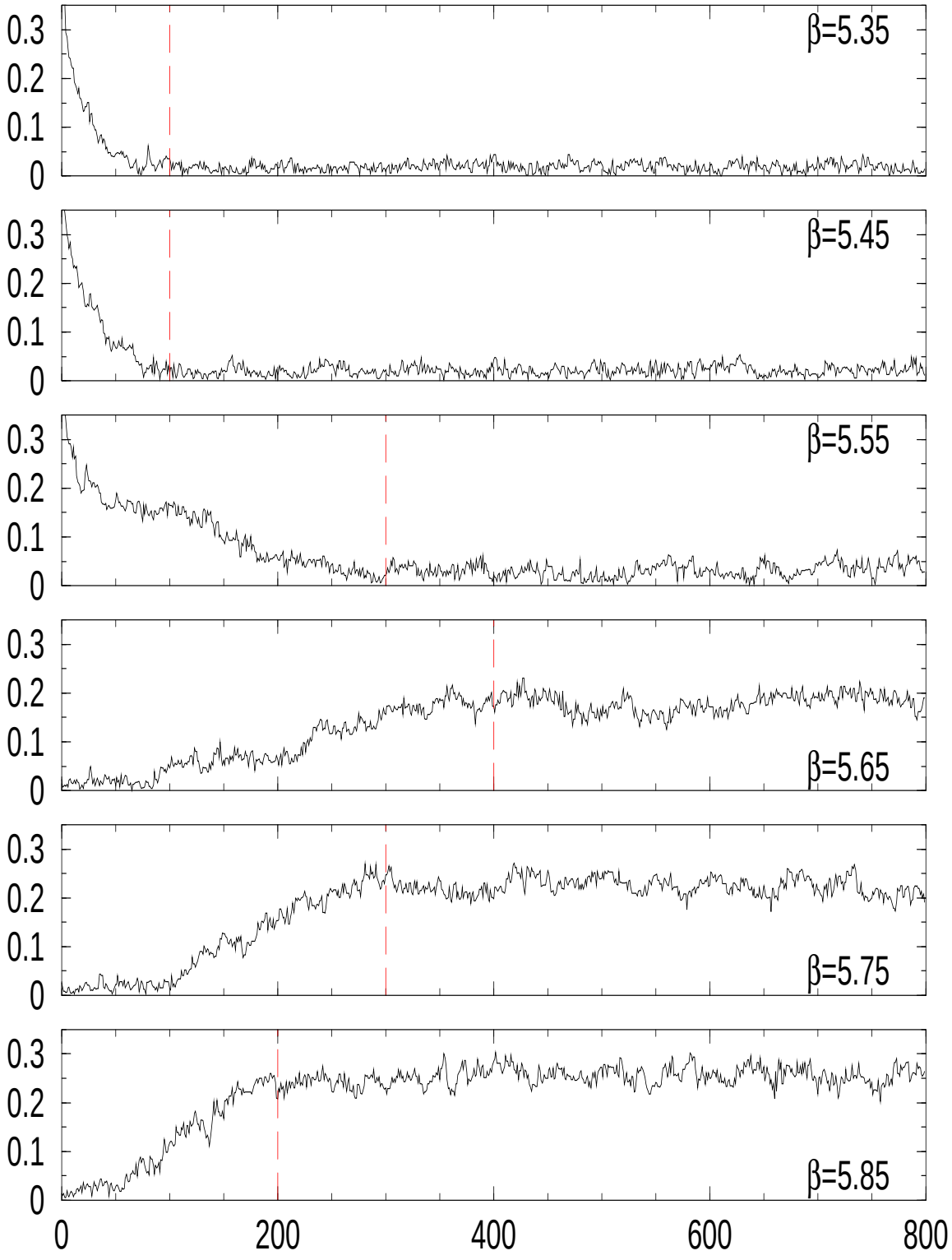


Figure 4: $\langle |W_3| \rangle$ evol: $8^3 \times 4, m_0 = 1.4, L_s = 12, m_f = 0.1$

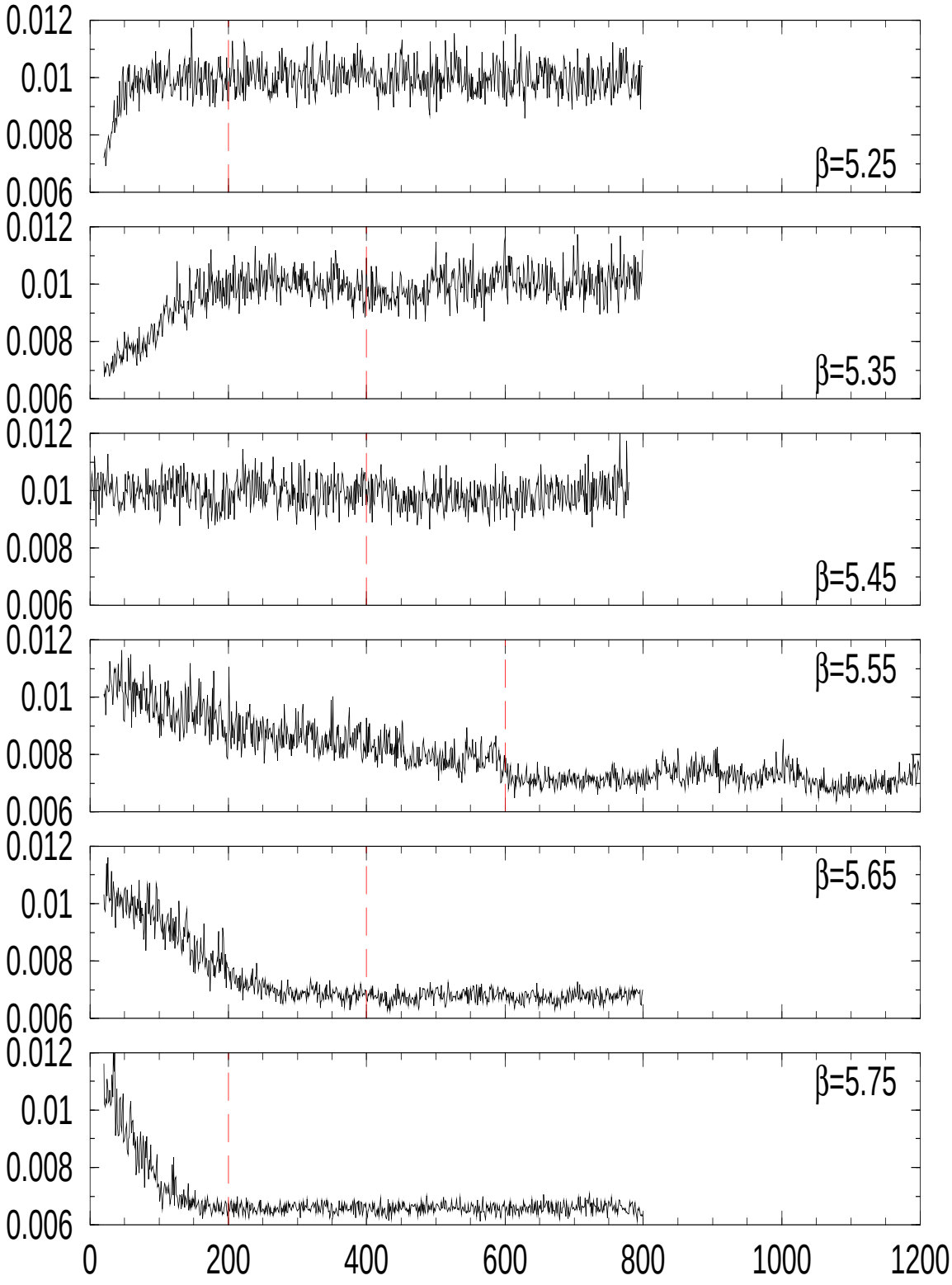


Figure 5: $\langle \overline{q}q \rangle$ evol: $8^3 \times 4, m_0 = 1.65, L_s = 12, m_f = 0.1$

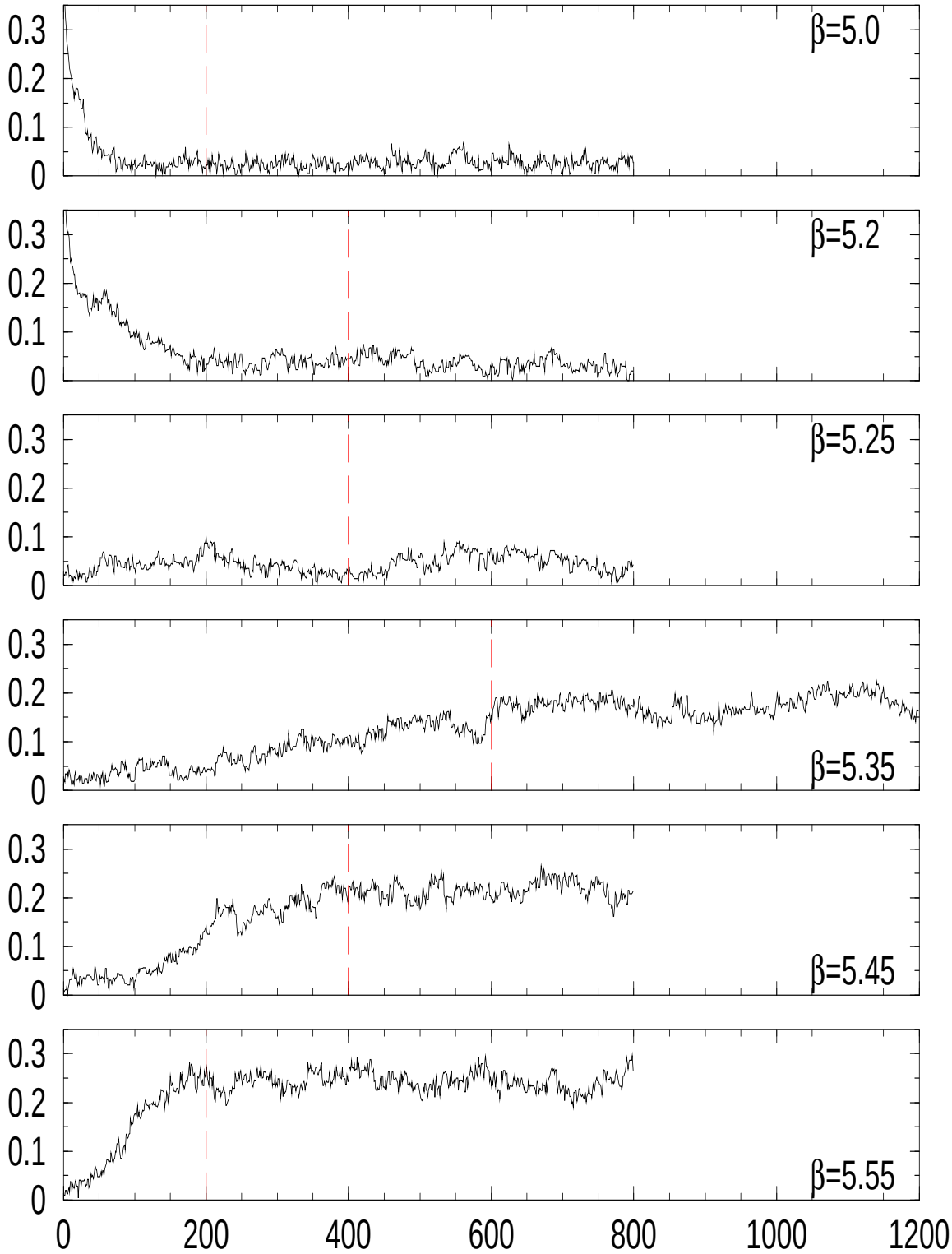


Figure 6: $\langle |W_3| \rangle$ evol: $8^3 \times 4, m_0 = 1.65, L_s = 12, m_f = 0.1$

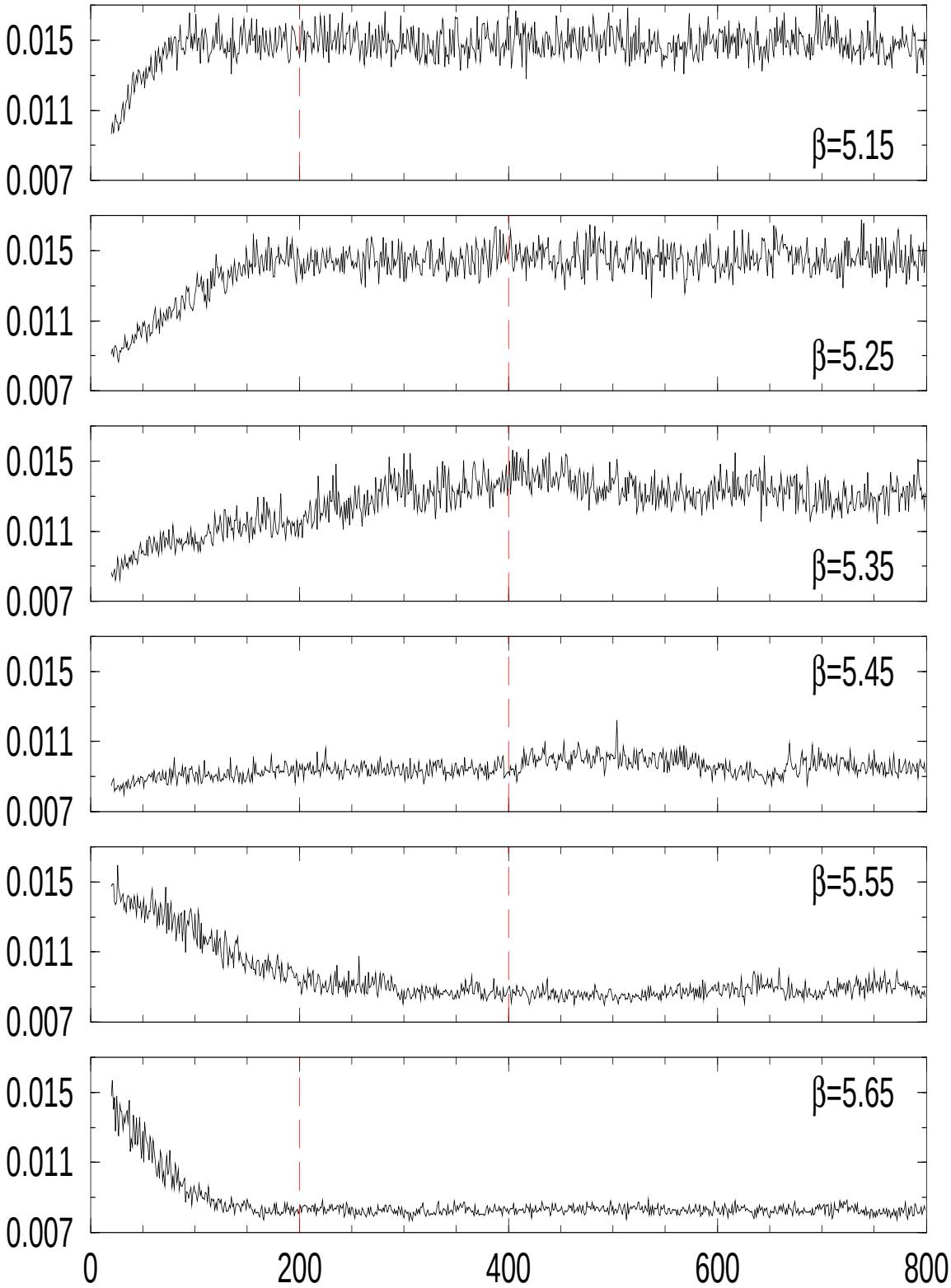


Figure 7: $\langle \overline{q}q \rangle$ evol: $8^3 \times 4, m_0 = 1.8, L_s = 12, m_f = 0.1$

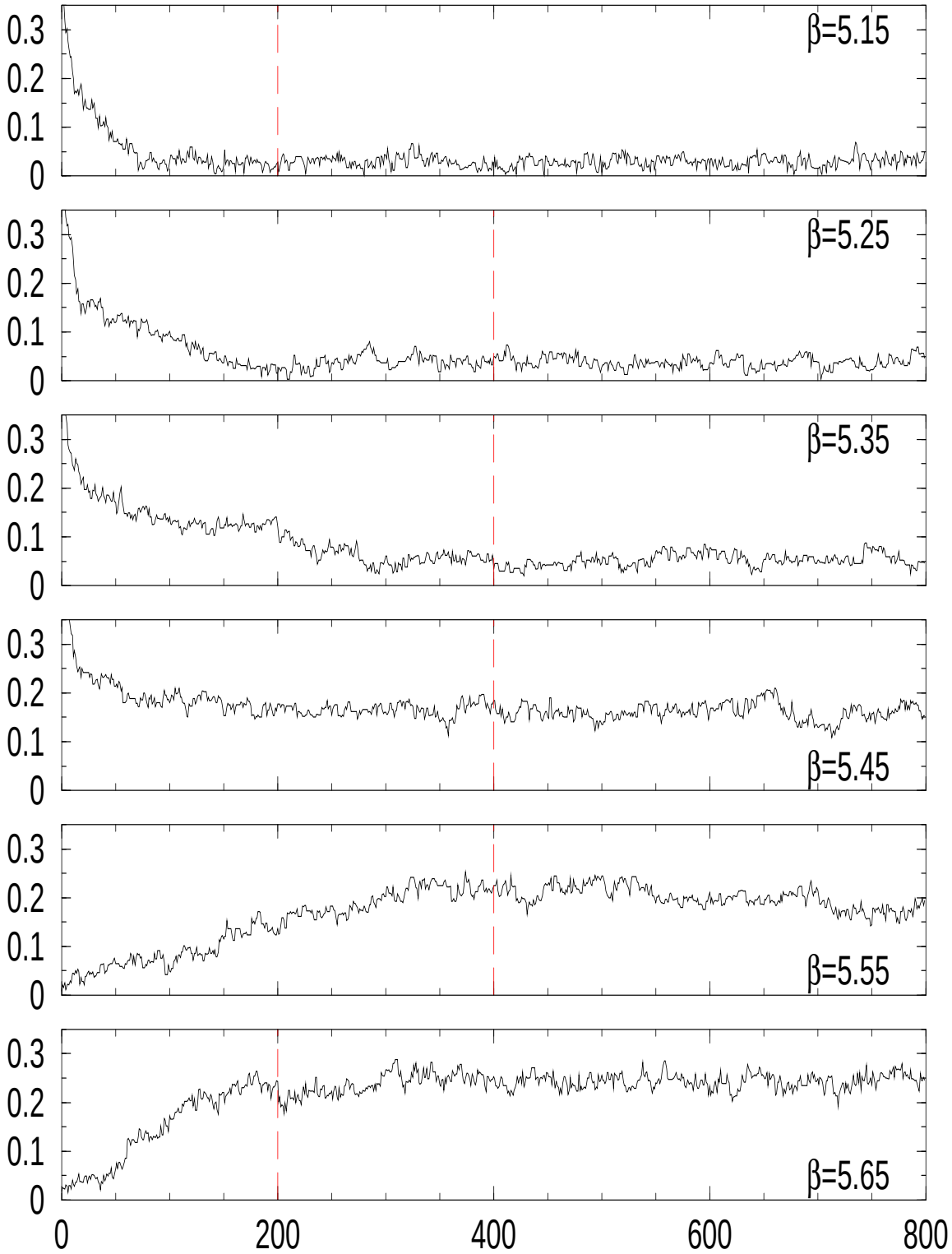


Figure 8: $\langle |W_3| \rangle$ evol: $8^3 \times 4, m_0 = 1.8, L_s = 12, m_f = 0.1$

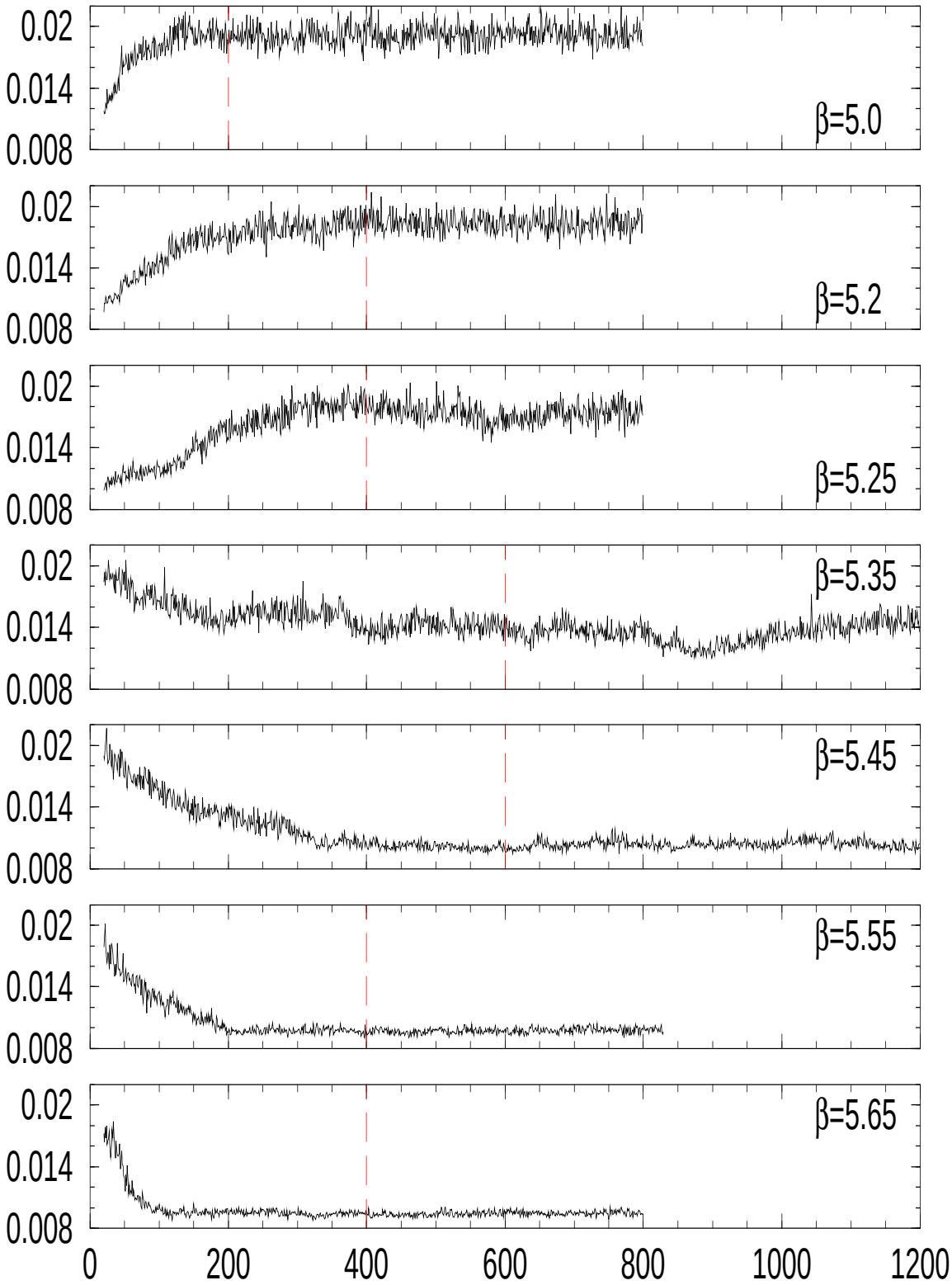


Figure 9: $\langle \overline{q}q \rangle$ evol: $8^3 \times 4, m_0 = 1.9, L_s = 12, m_f = 0.1$

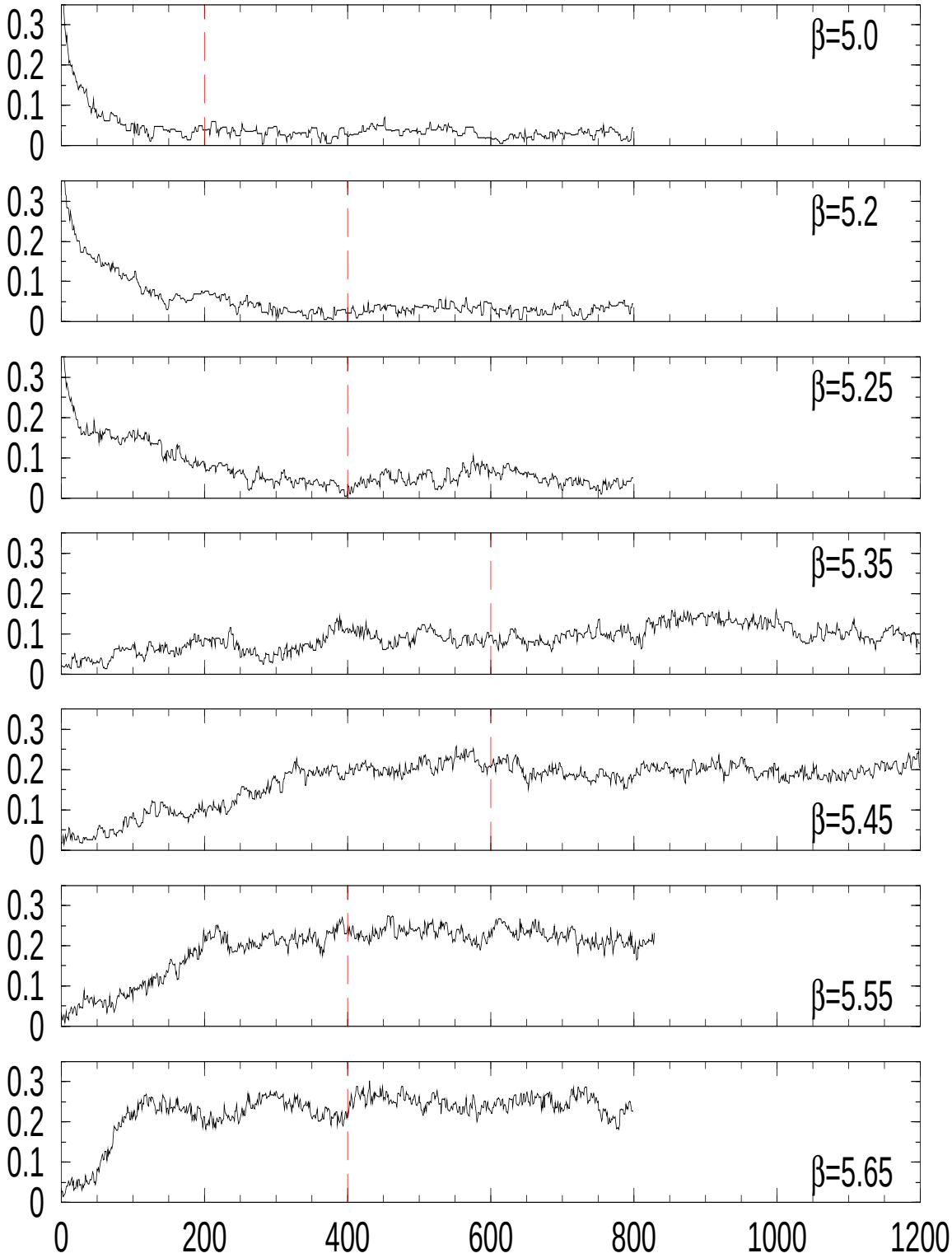


Figure 10: $\langle |W_3| \rangle$ evol: $8^3 \times 4, m_0 = 1.9, L_s = 12, m_f = 0.1$

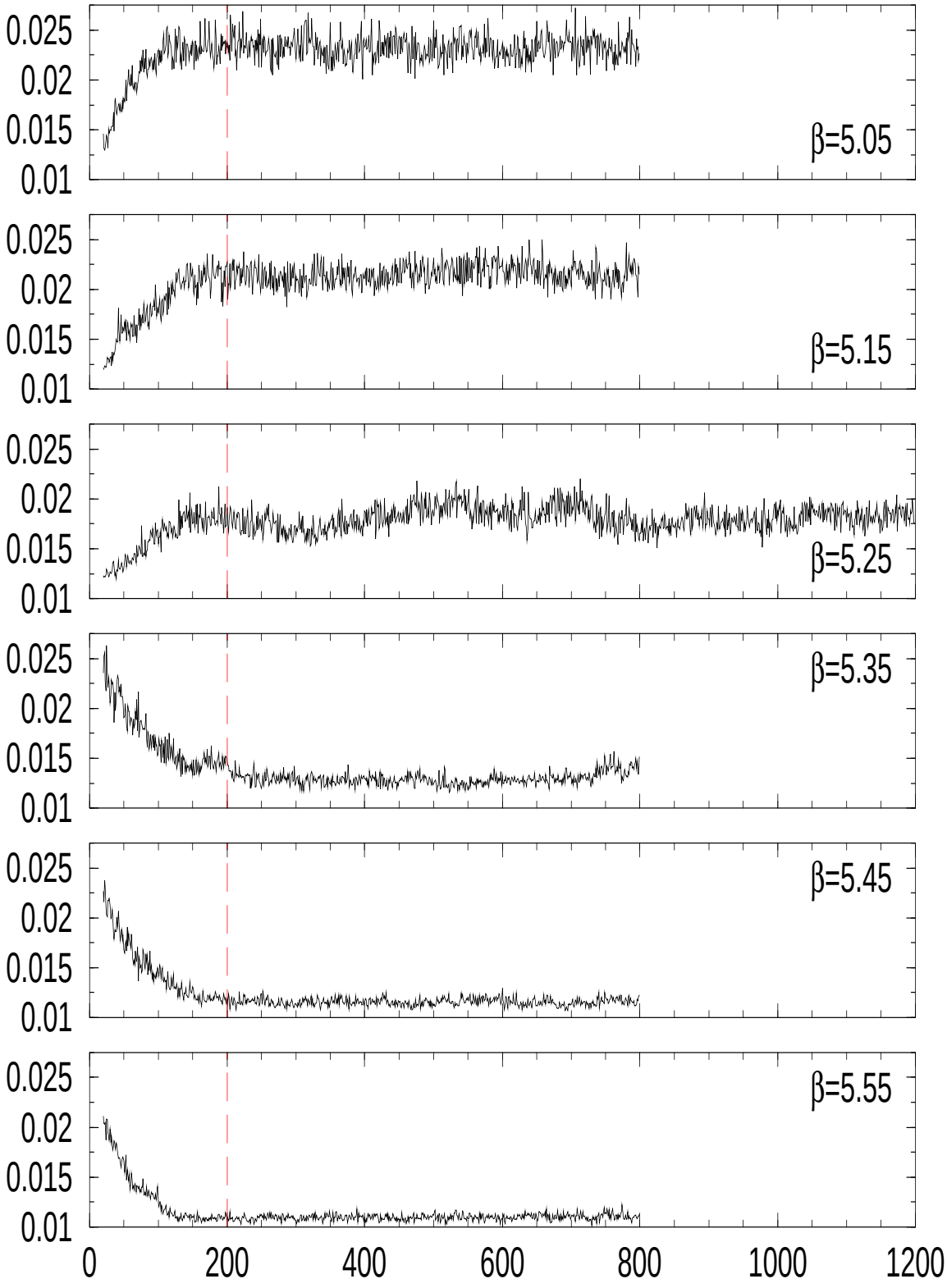


Figure 11: $\langle \overline{q}q \rangle$ evol: $8^3 \times 4, m_0 = 2.0, L_s = 12, m_f = 0.1$

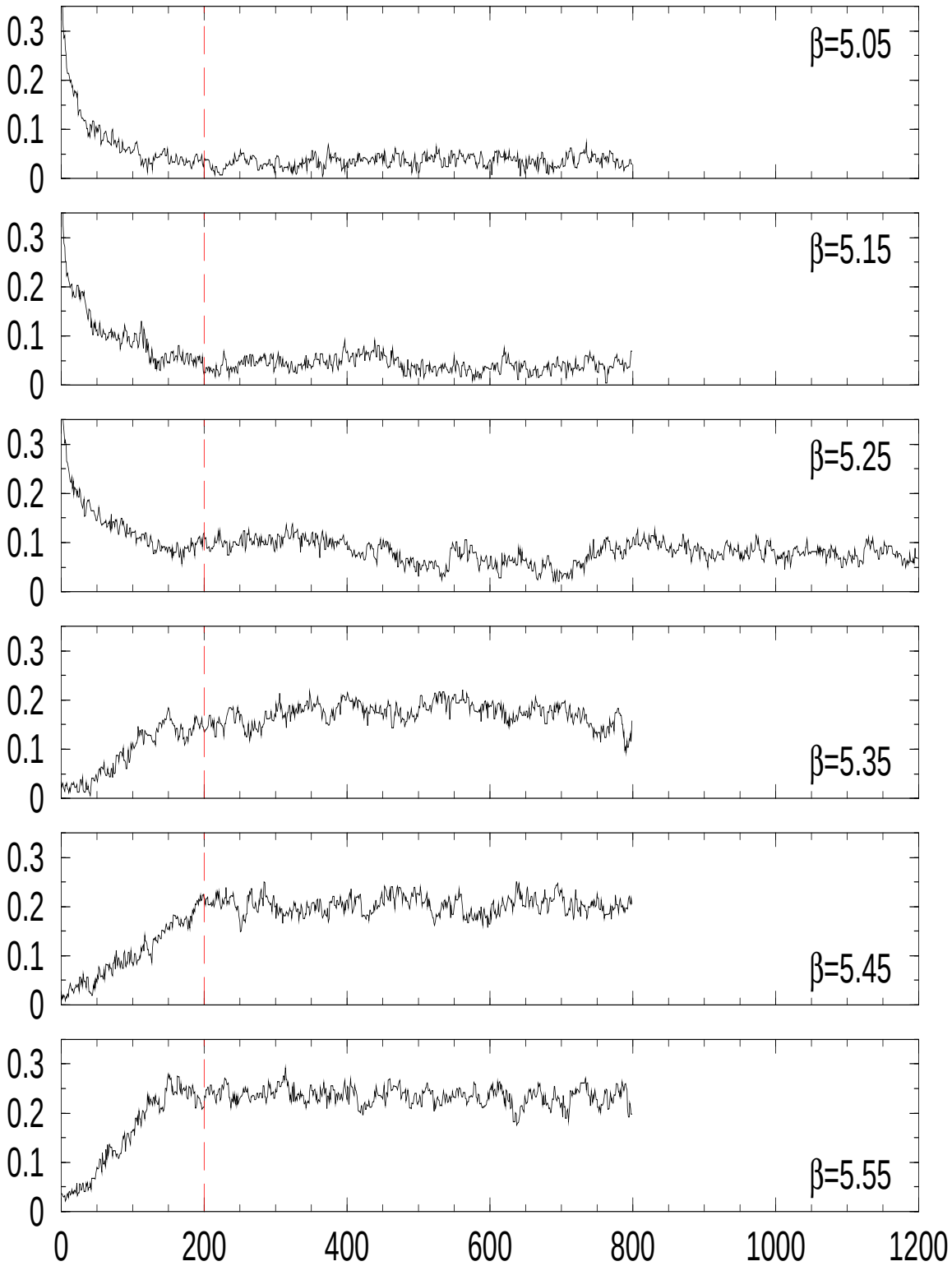


Figure 12: $\langle |W_3| \rangle$ evol: $8^3 \times 4, m_0 = 2.0, L_s = 12, m_f = 0.1$

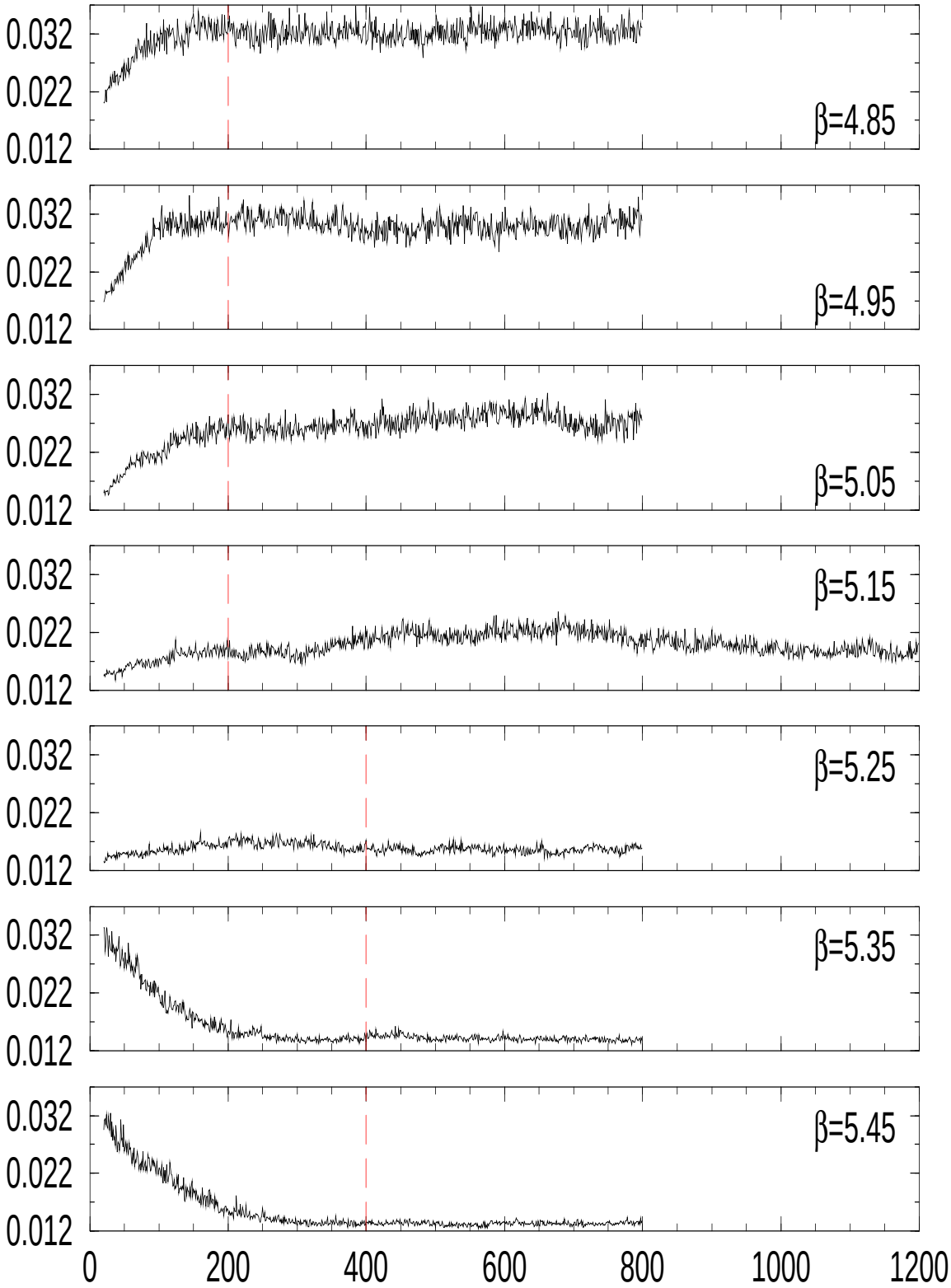


Figure 13: $\langle \overline{q}q \rangle$ evol: $8^3 \times 4, m_0 = 2.15, L_s = 12, m_f = 0.1$

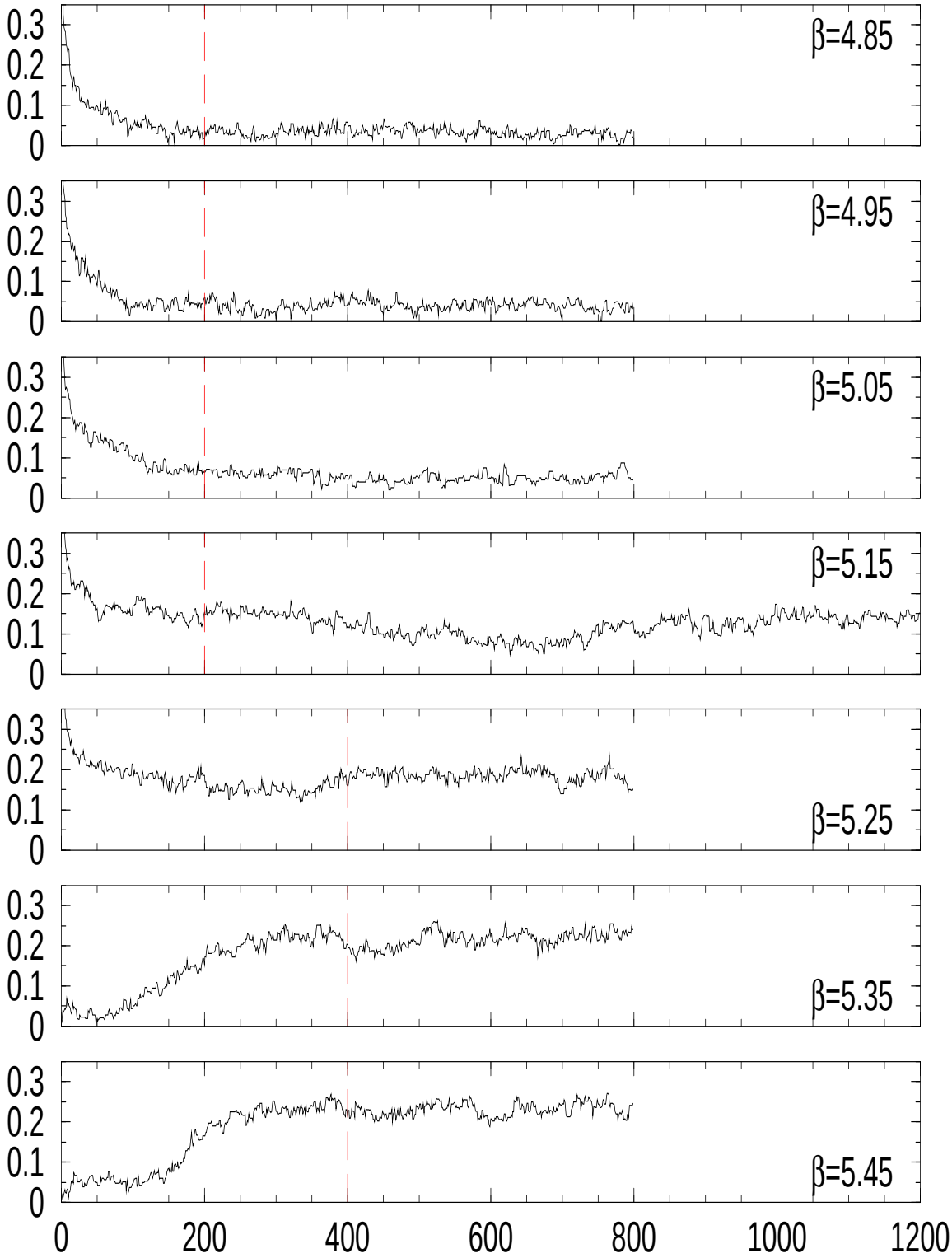


Figure 14: $\langle |W_3| \rangle$ evol: $8^3 \times 4, m_0 = 2.15, L_s = 12, m_f = 0.1$

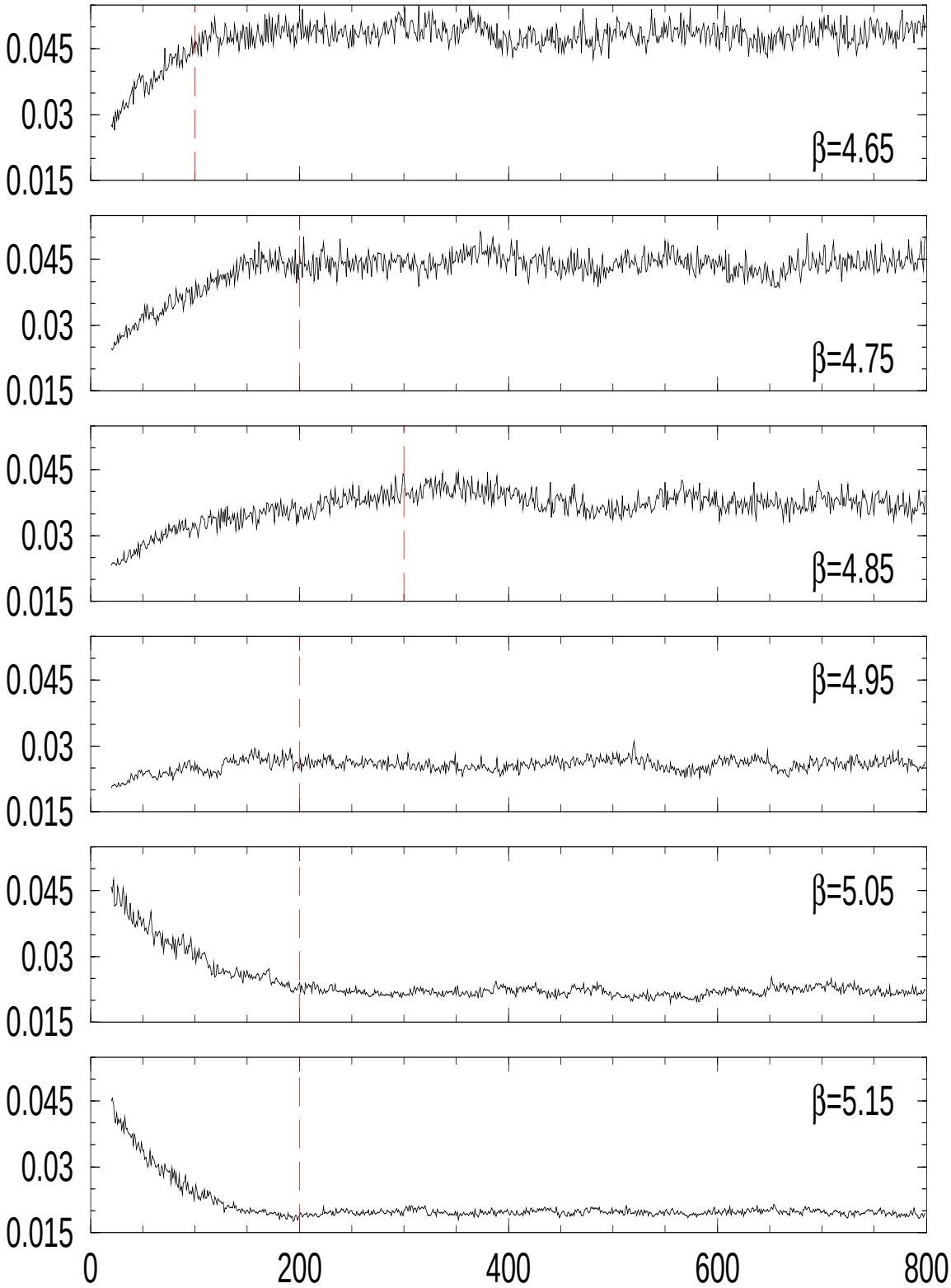


Figure 15: $\langle \overline{q}q \rangle$ evol: $8^3 \times 4, m_0 = 2.4, L_s = 12, m_f = 0.1$

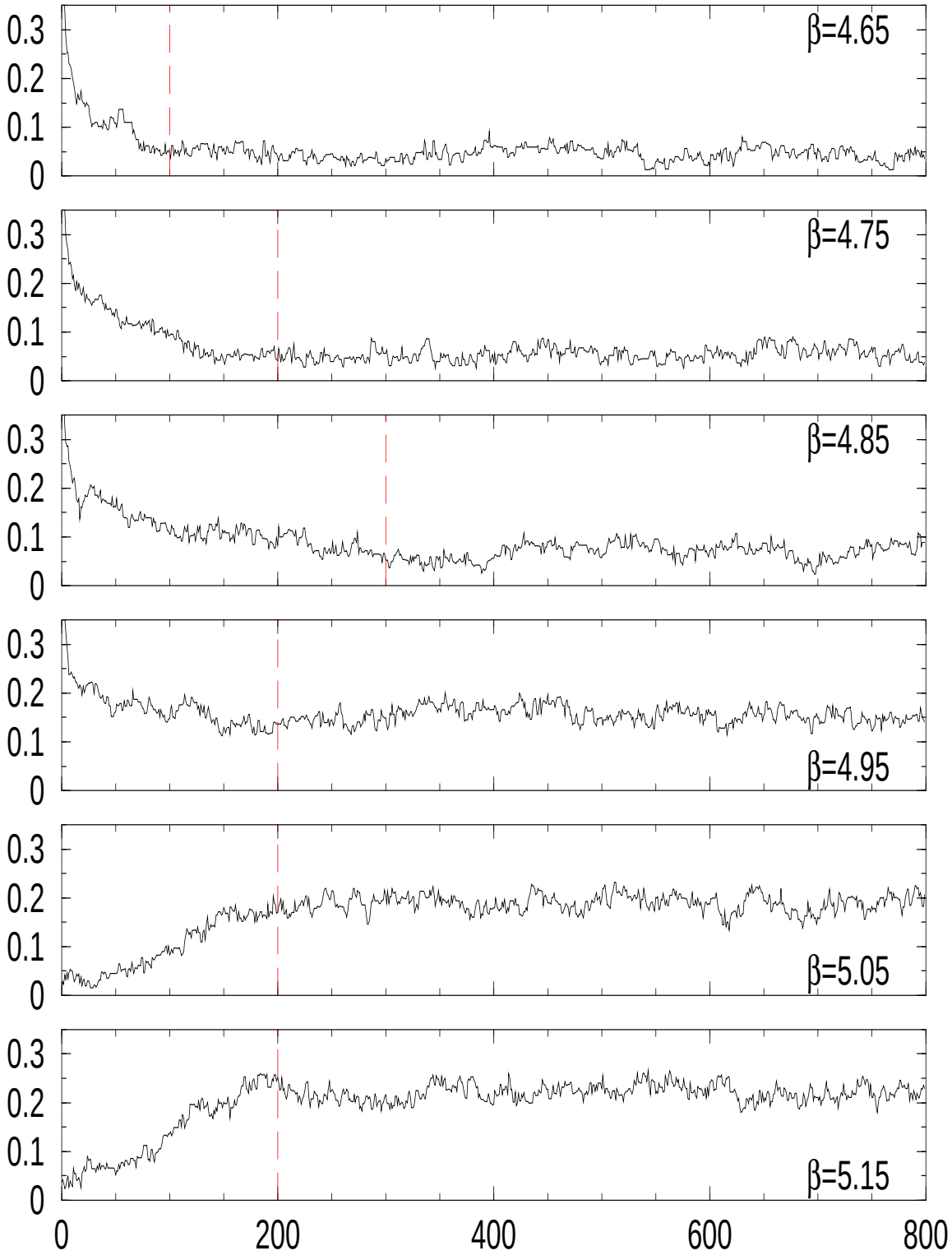


Figure 16: $\langle |W_3| \rangle$ evol: $8^3 \times 4, m_0 = 2.4, L_s = 12, m_f = 0.1$

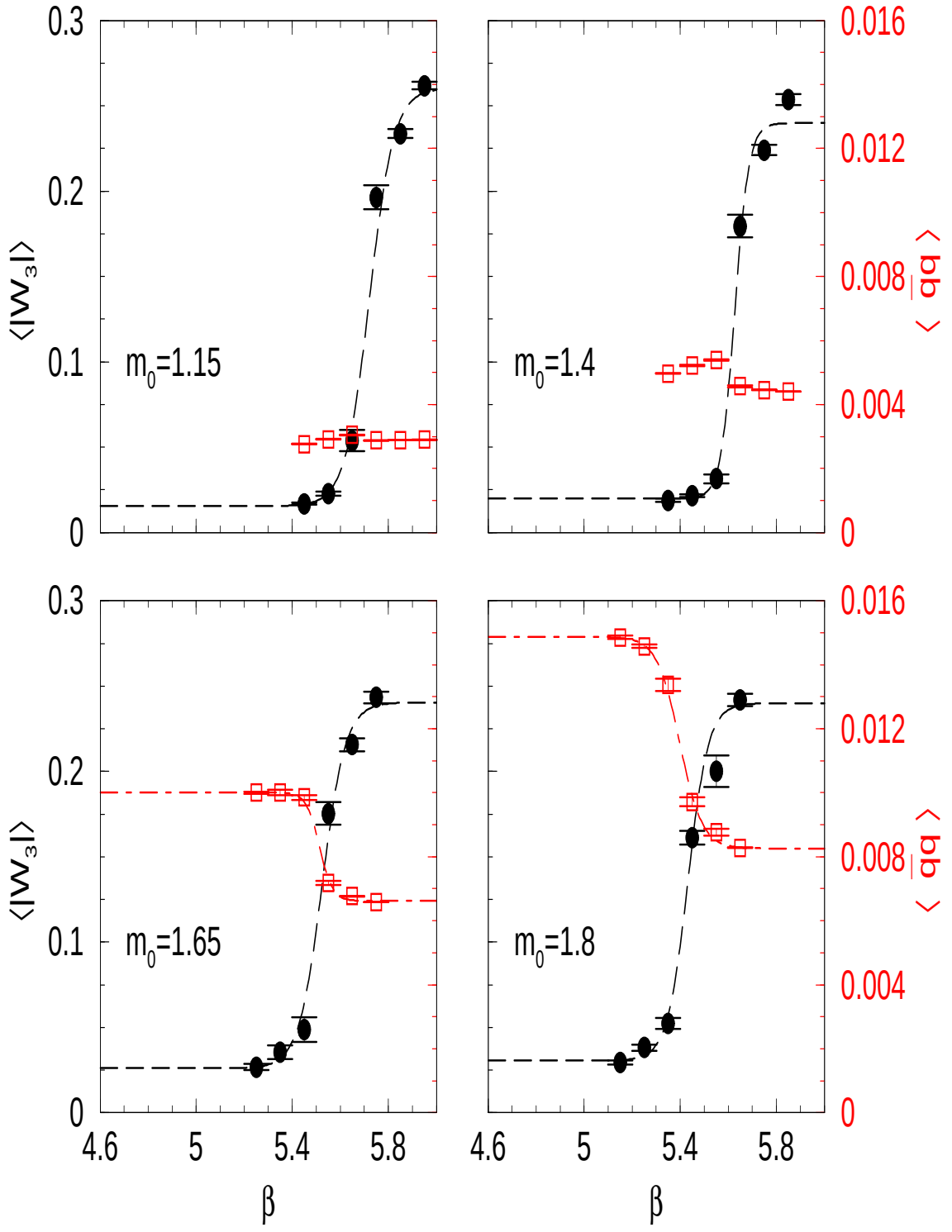


Figure 17: tanh fits of $\beta_c$: $8^3 \times 4; m_0 = 1.15, \cdots, 1.8; L_s = 12; m_f = 0.1$

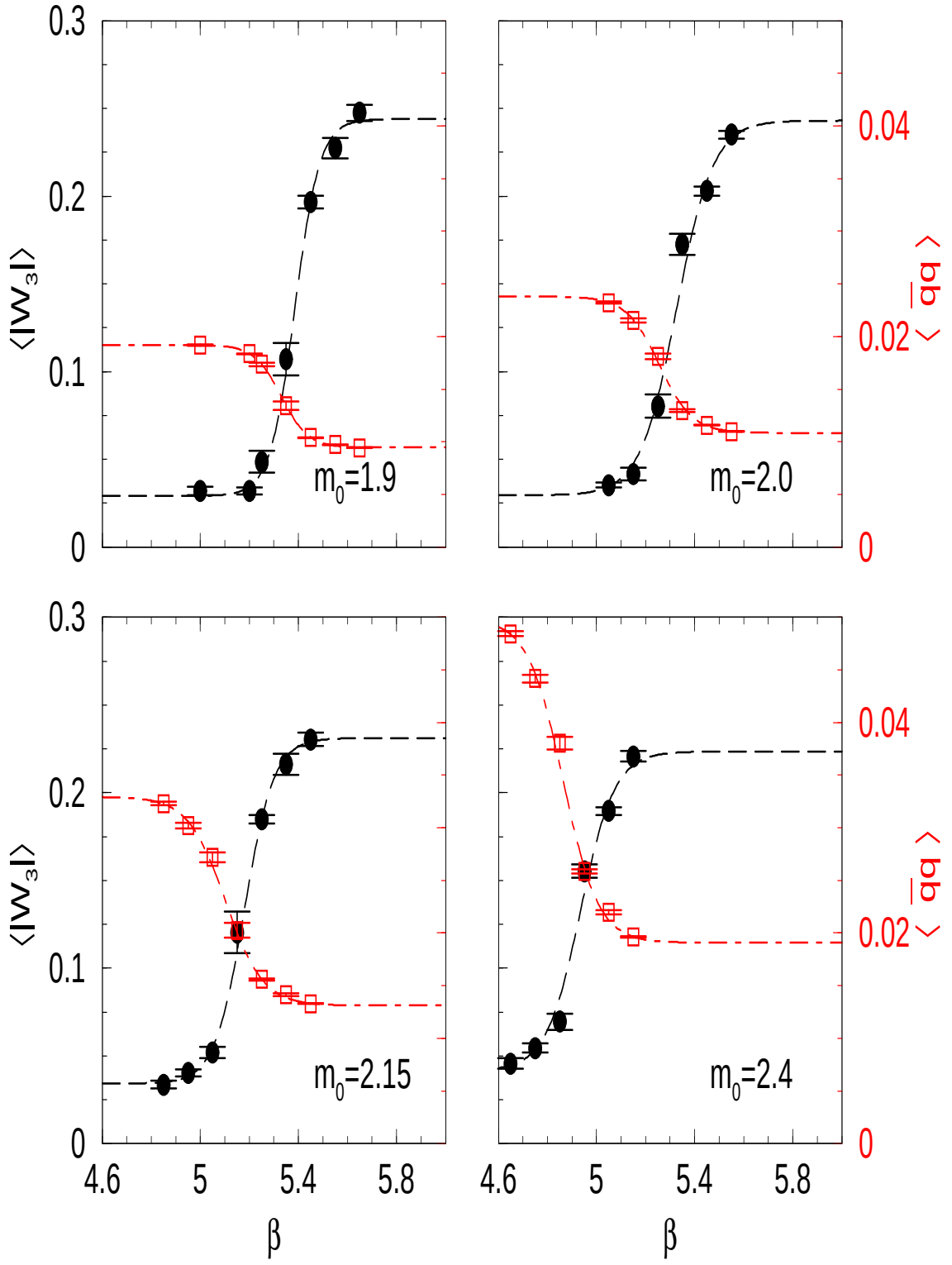


Figure 18: tanh fits of $\beta_c$: $8^3 \times 4; m_0 = 1.9, \cdots, 2.4; L_s = 12; m_f = 0.1$

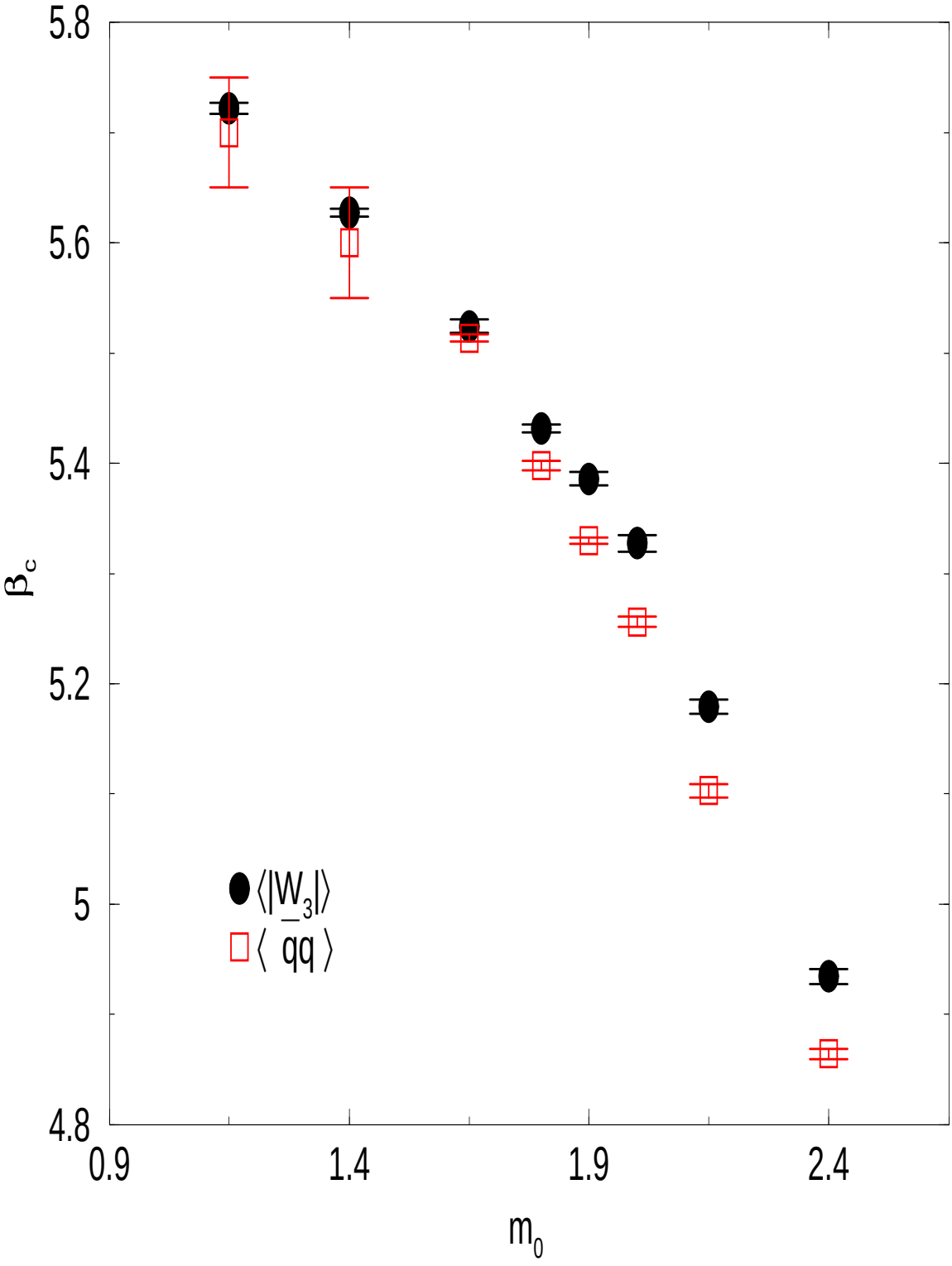


Figure 19: $\beta_c$ versus $m_0$: $8^3 \times 4, L_s = 12, m_f = 0.1$

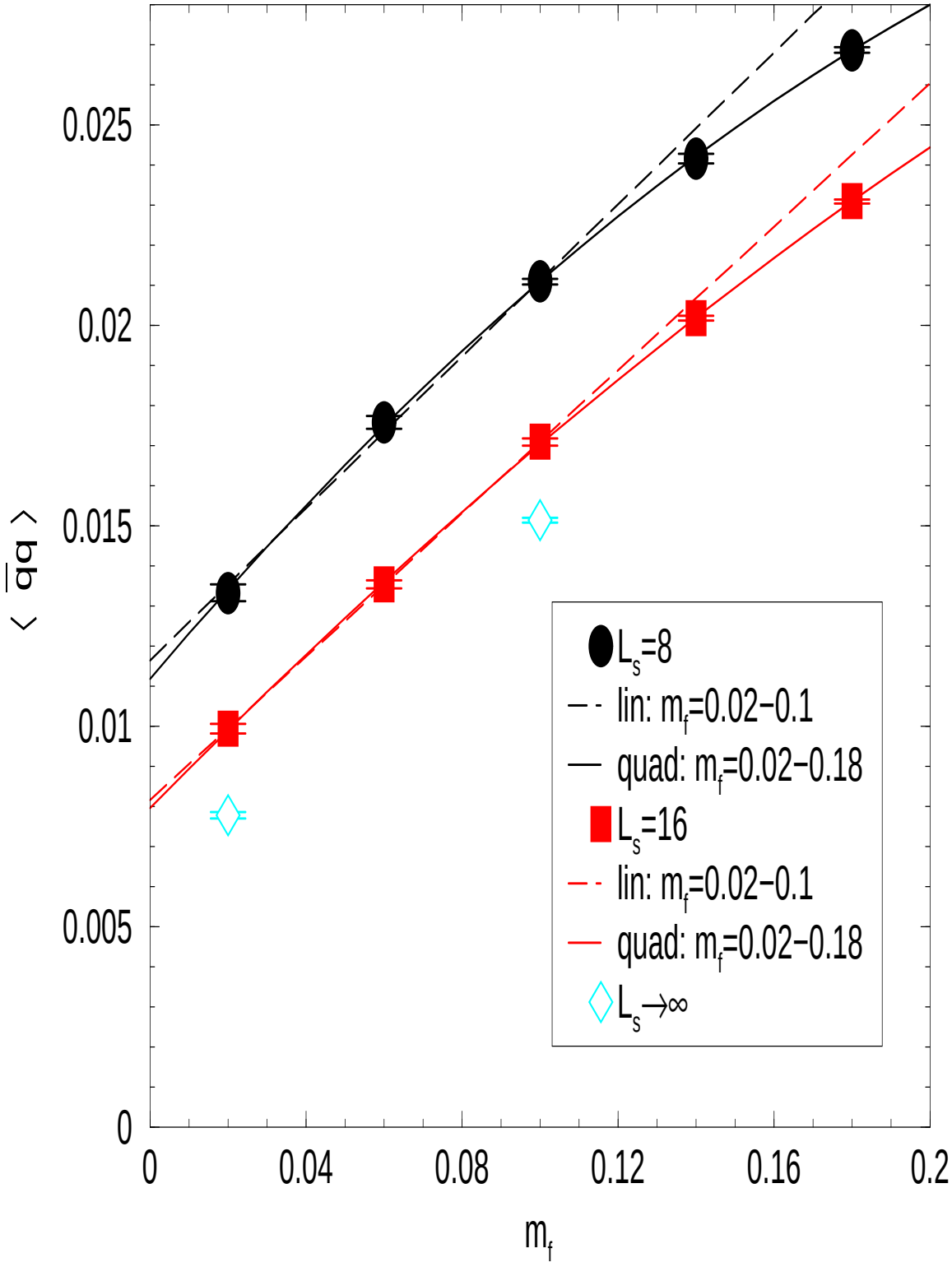


Figure 20: Fit of $\langle \overline{q}q \rangle = c_0 + c_1 m_f + c_2 m_f^2$: $8^3 \times 4; \beta = 5.2; m_0 = 1.9; L_s = 8, 16$

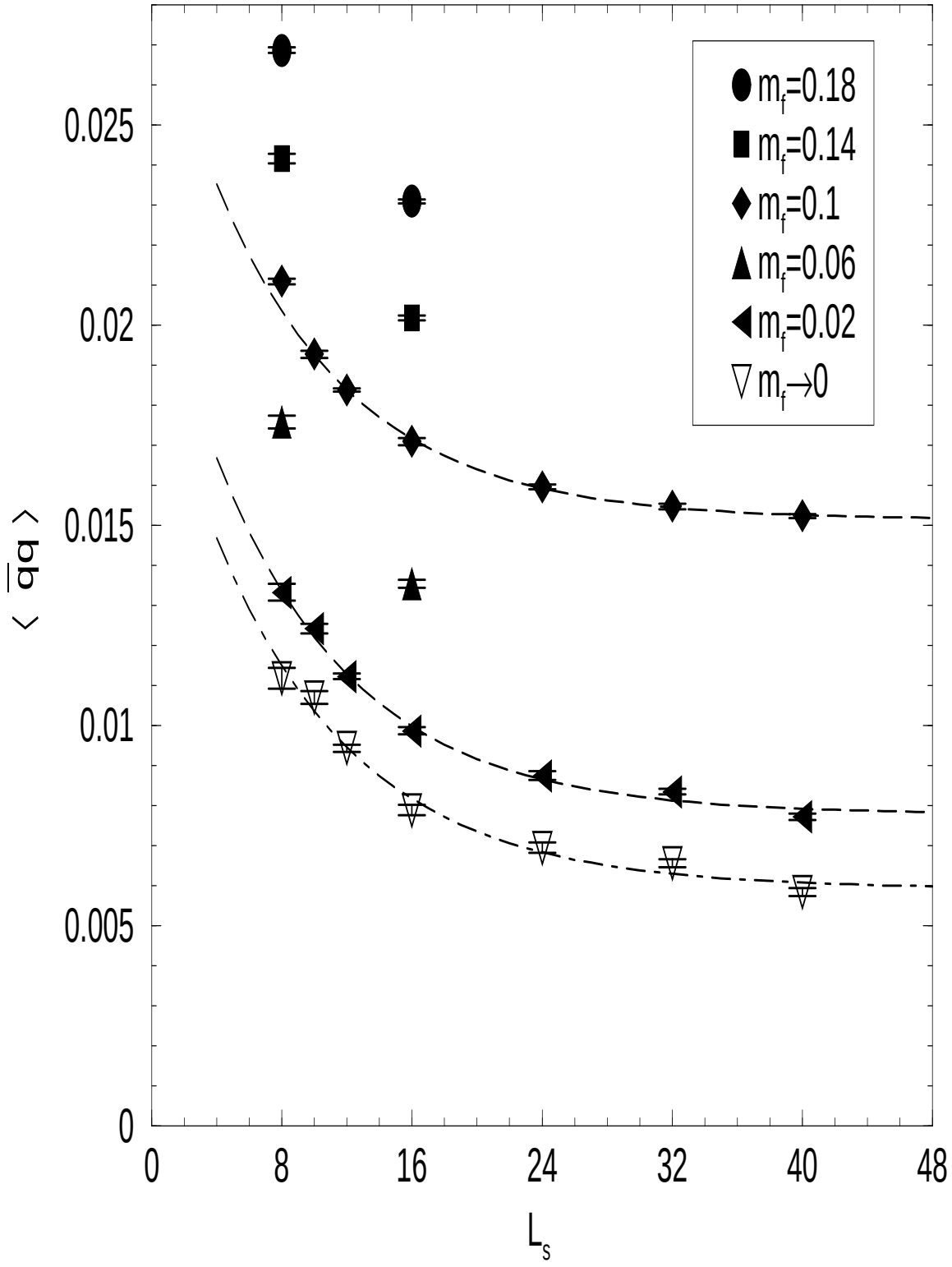


Figure 21: Fit of $\langle \overline{q}q \rangle = c_0 + c_1 \exp(-c_2 L_s)$: $8^3 \times 4, \beta = 5.2, m_0 = 1.9$

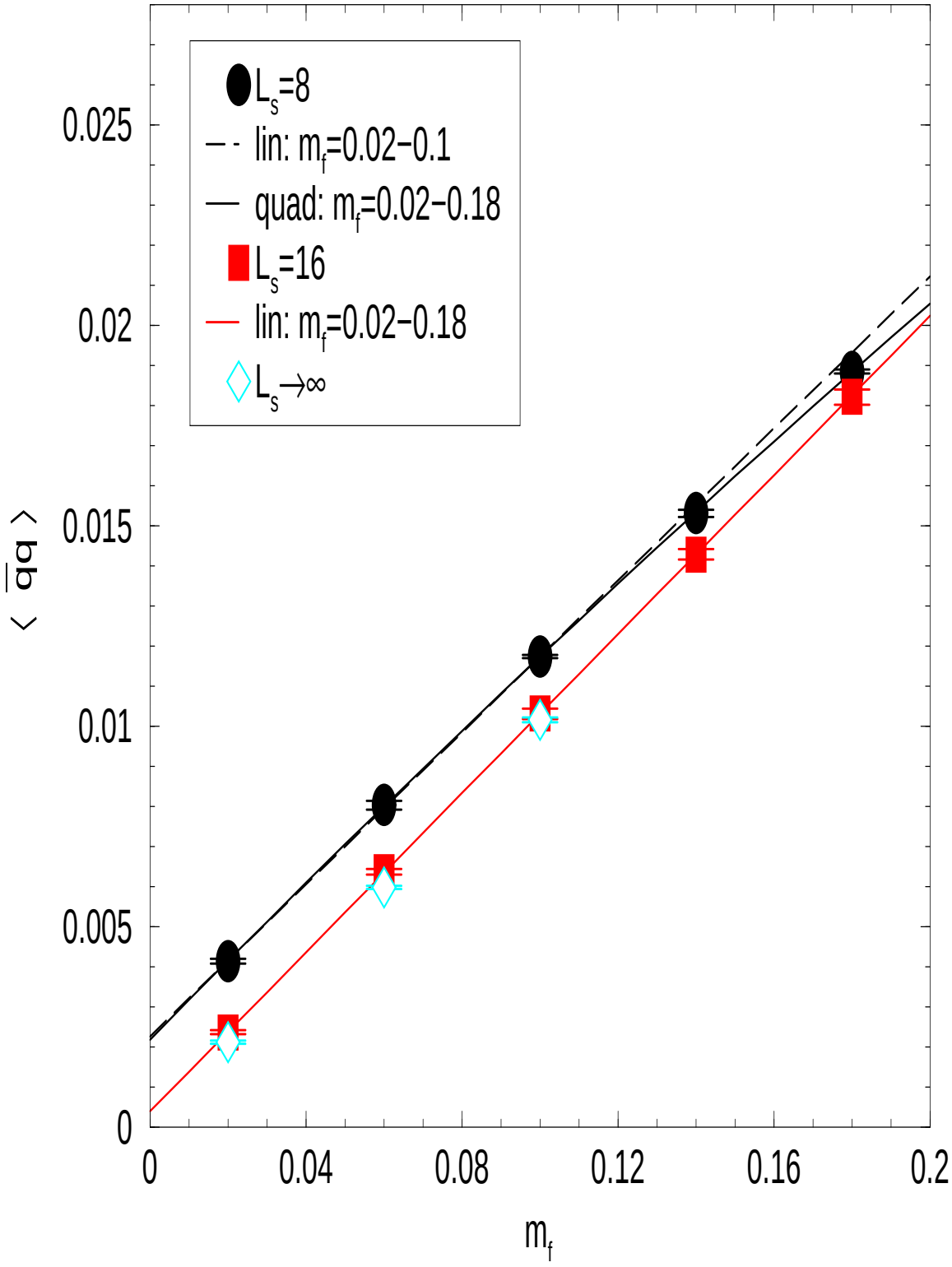


Figure 22: Fit of $\langle \overline{q}q \rangle = c_0 + c_1 m_f + c_2 m_f^2$: $8^3 \times 4; \beta = 5.45; m_0 = 1.9; L_s = 8, 16$

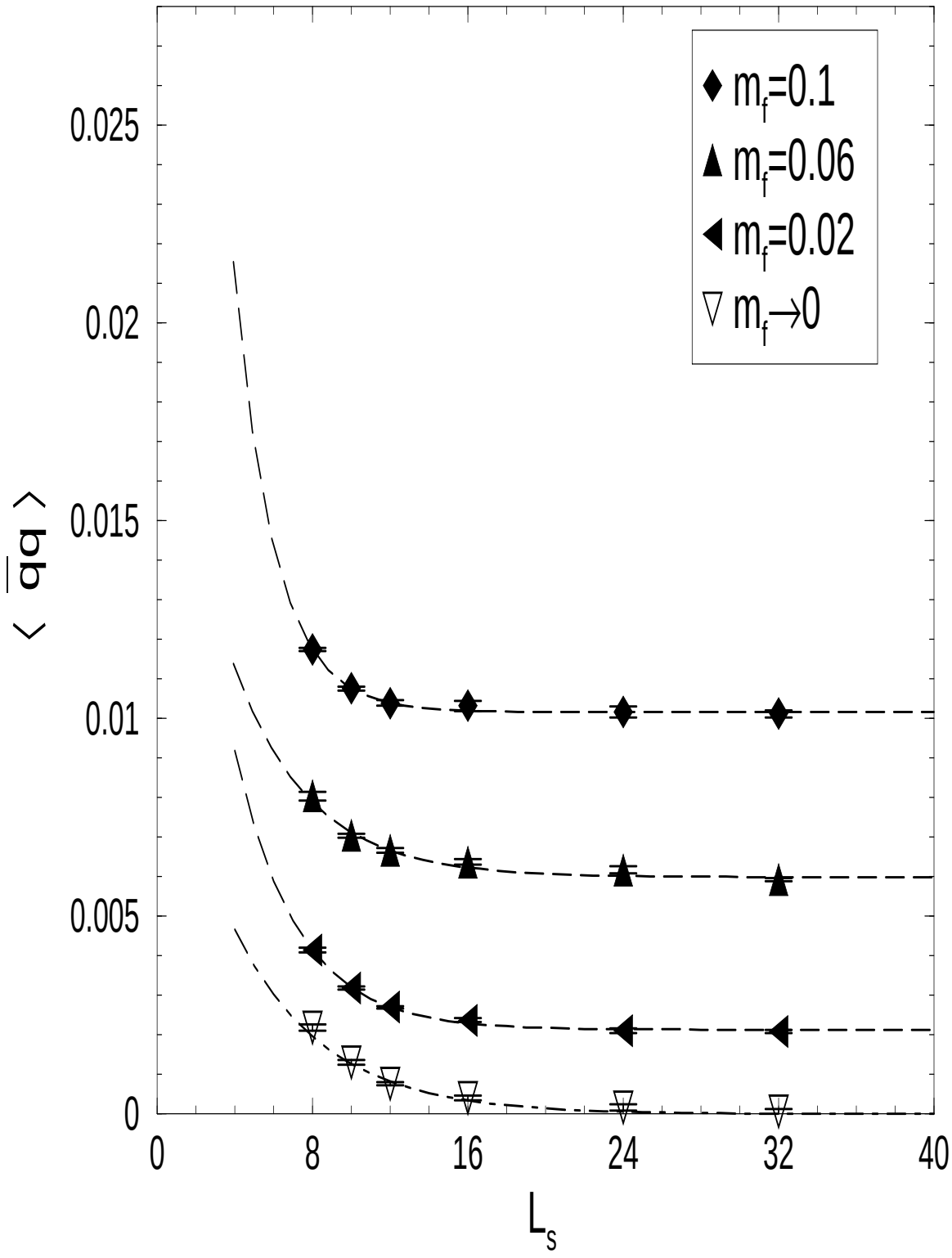


Figure 23: Fit of $\langle \overline{q}q \rangle = c_0 + c_1 \exp(-c_2 L_s)$: $8^3 \times 4, \beta = 5.45, m_0 = 1.9$

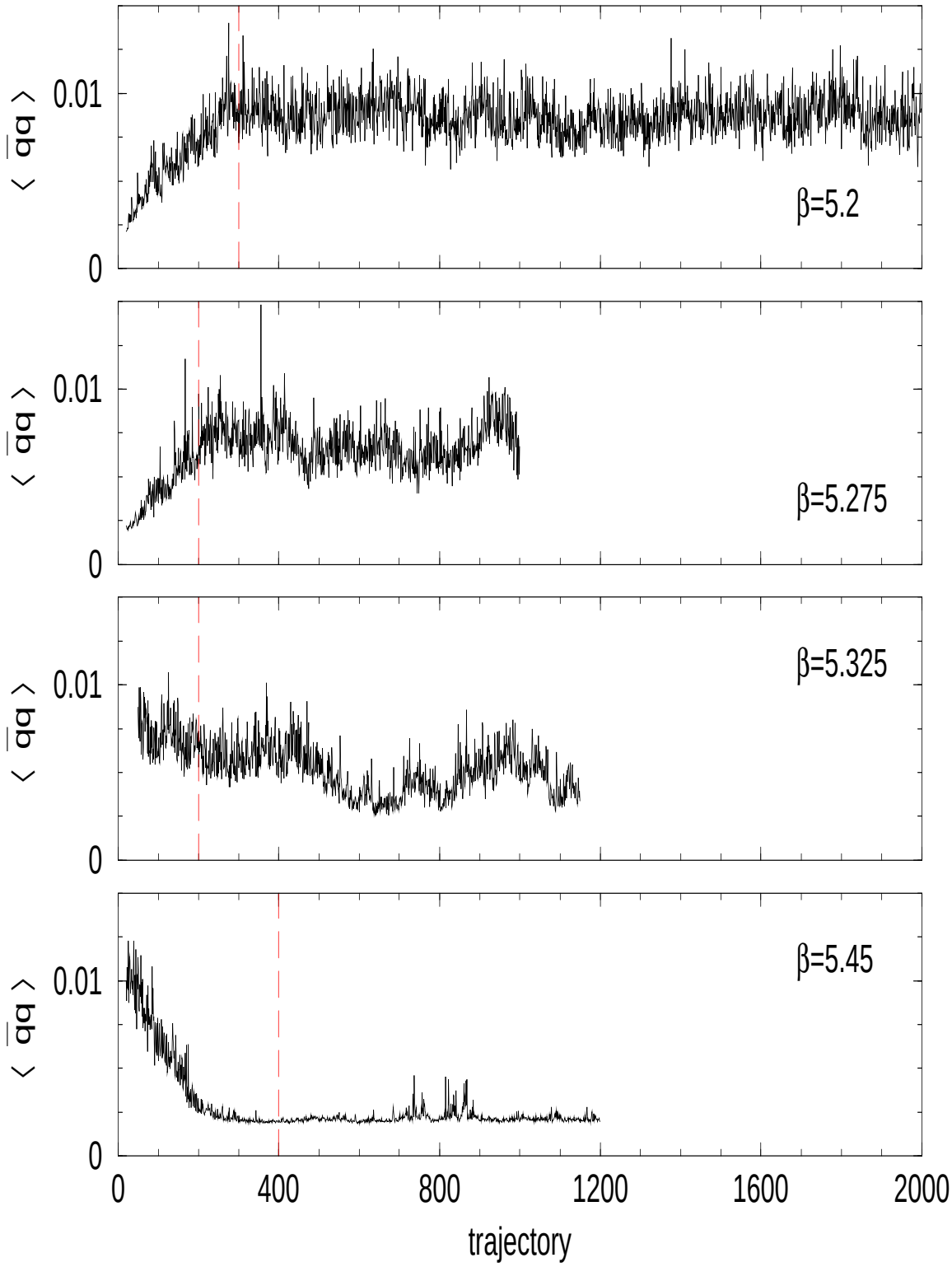


Figure 24: $\langle \overline{q}q \rangle$ evol: $8^3 \times 4, m_0 = 1.9, L_s = 24, m_f = 0.02$

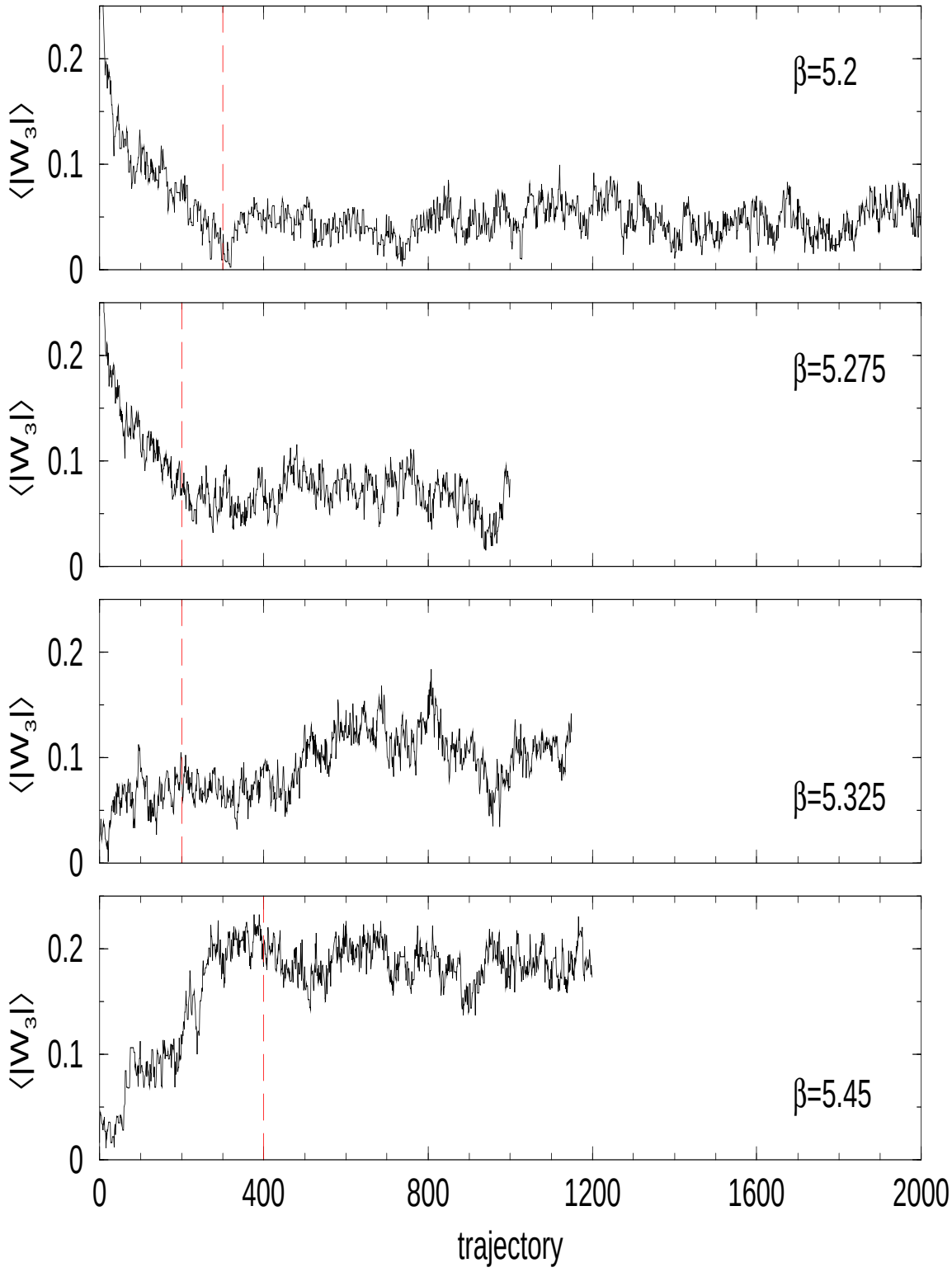


Figure 25: $\langle |W_3| \rangle$ evol: $8^3 \times 4, m_0 = 1.9, L_s = 24, m_f = 0.02$

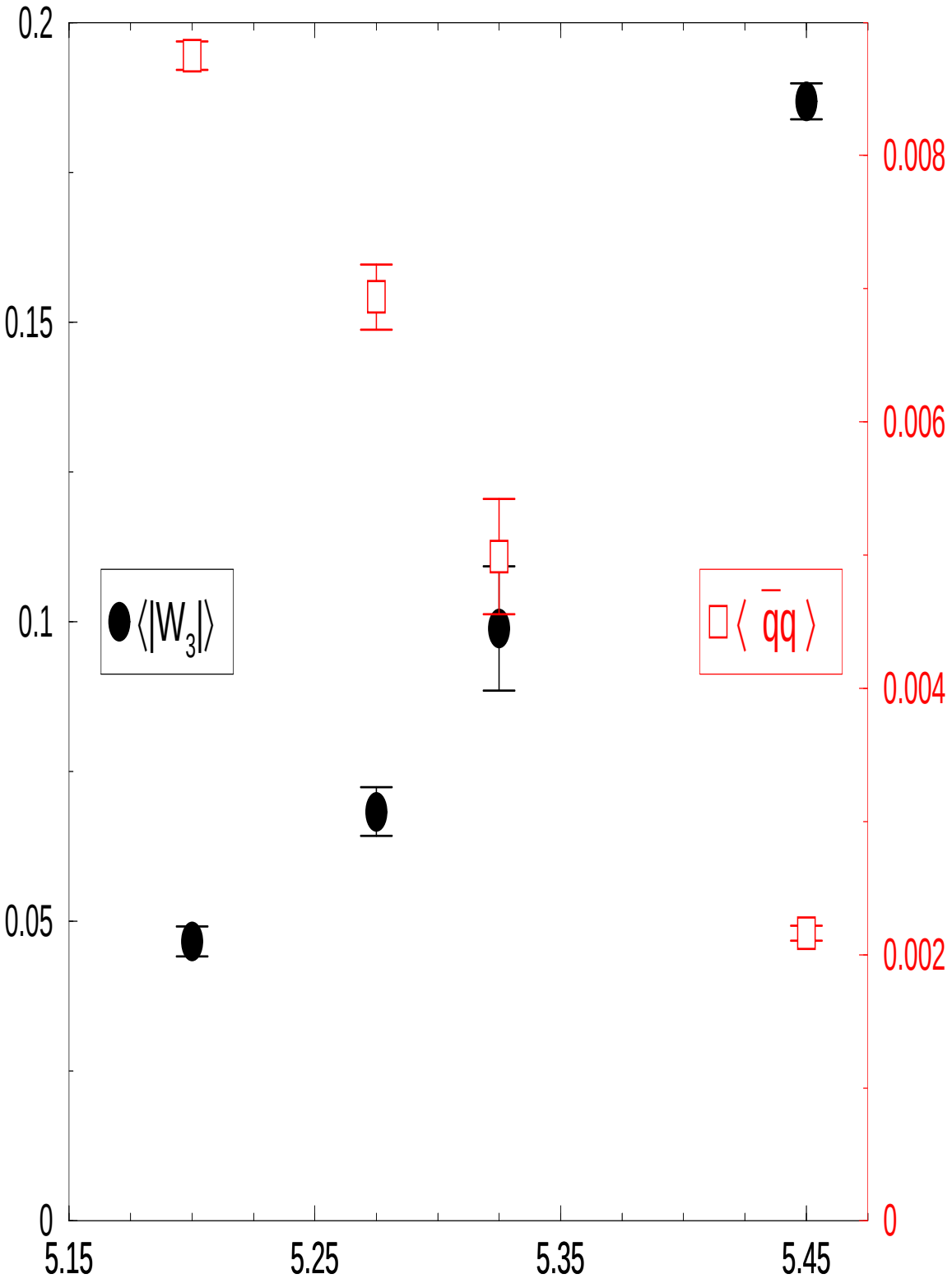


Figure 26: $\langle \overline{q}q \rangle$, $\langle |W_3| \rangle$ *vs.* $\beta$: $8^3 \times 4, m_0 = 1.9, L_s = 24, m_f = 0.02$

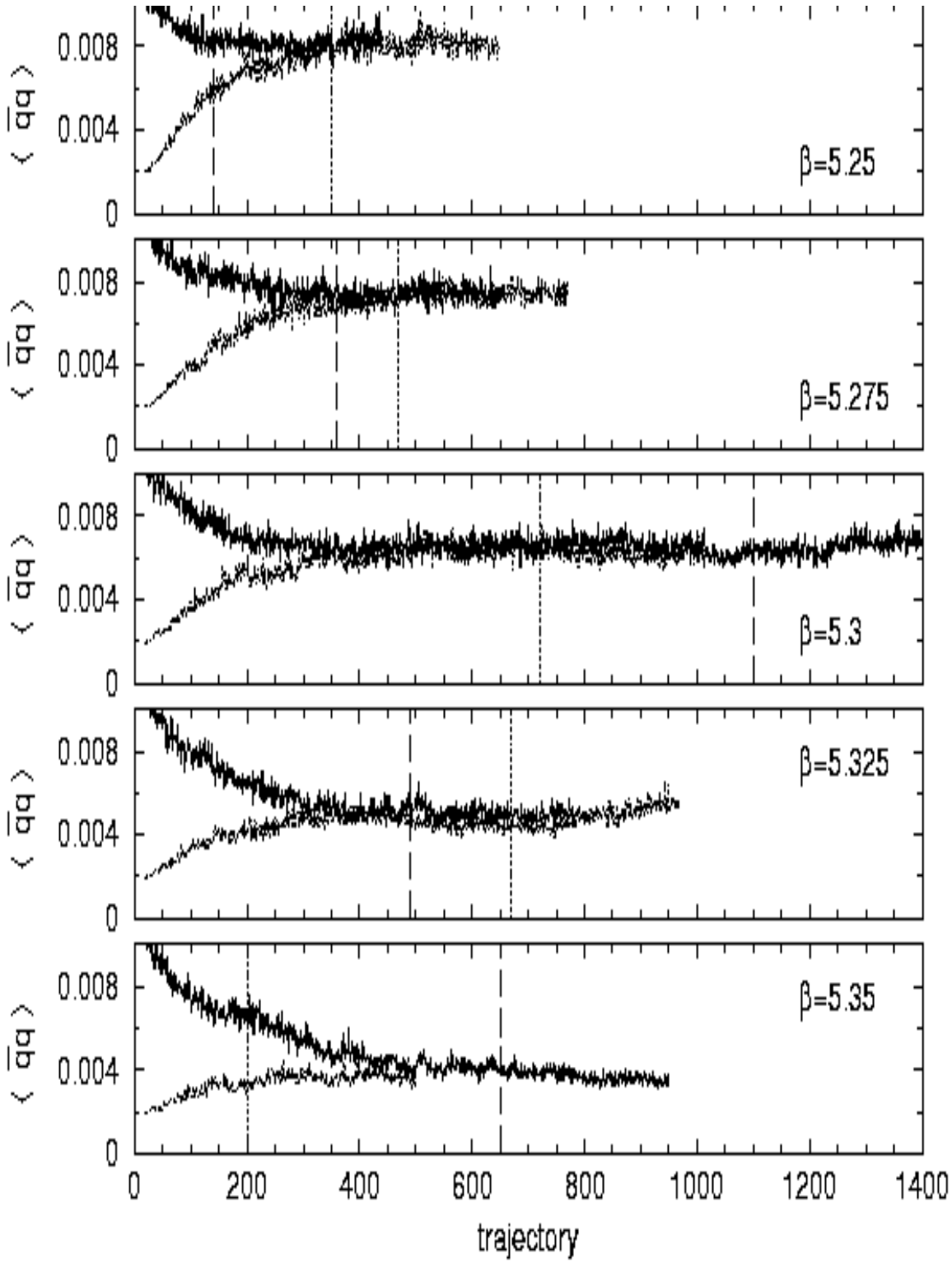


Figure 27: $\langle \overline{q}q \rangle$ evol: $16^3 \times 4, m_0 = 1.9, L_s = 24, m_f = 0.02$

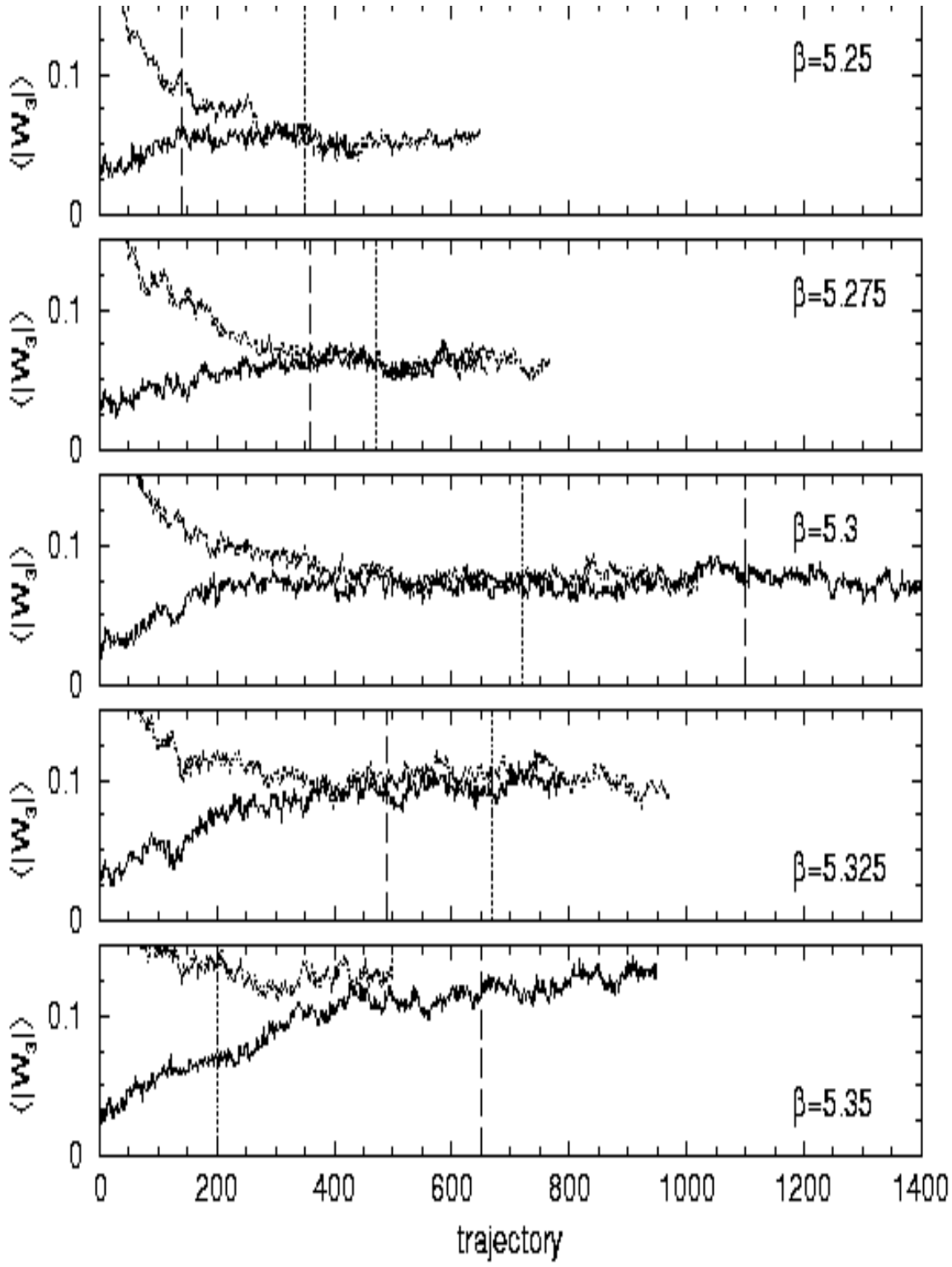


Figure 28: $\langle |W_3| \rangle$ evol: $16^3 \times 4, m_0 = 1.9, L_s = 24, m_f = 0.02$

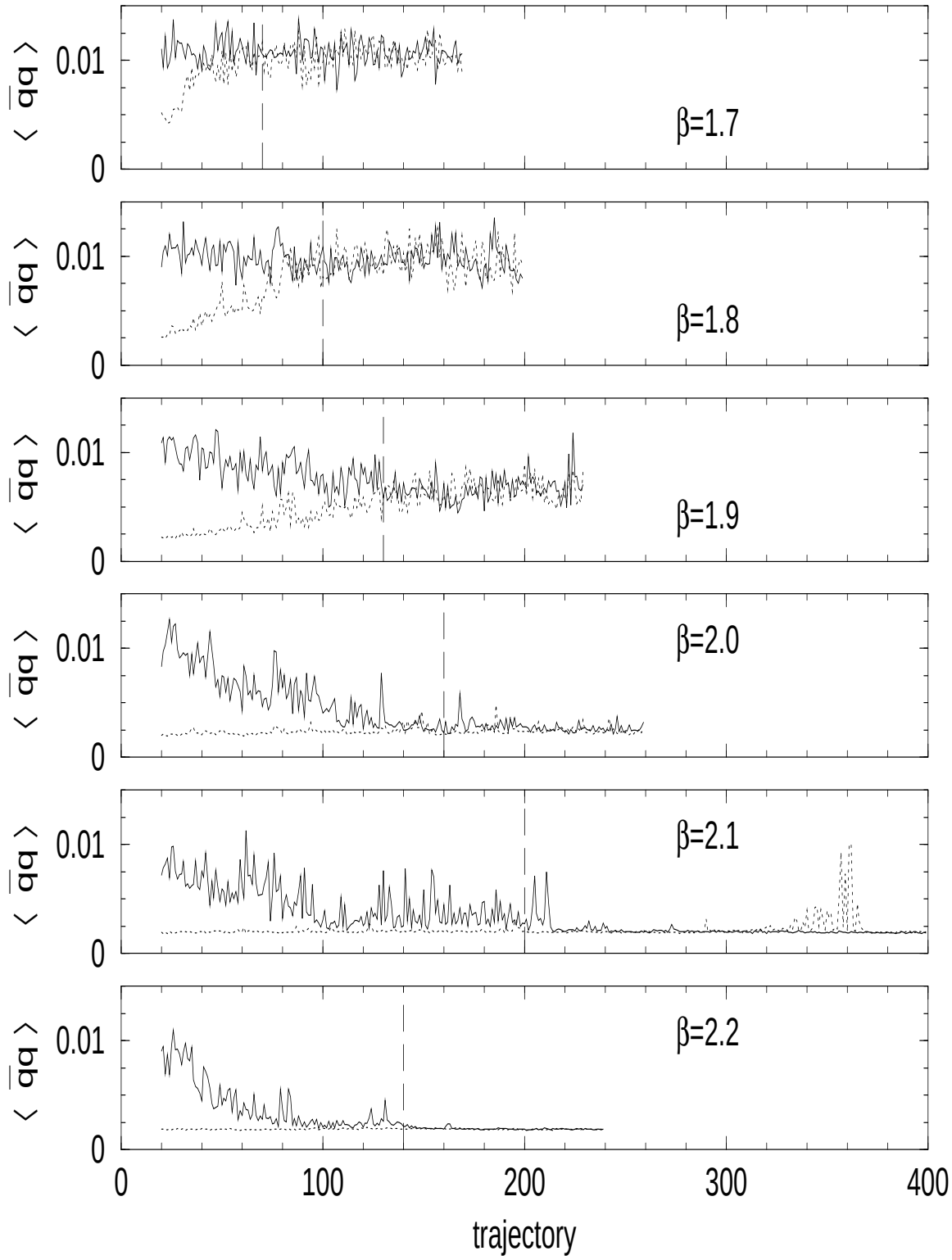


Figure 29: $\langle \overline{q}q \rangle$ evol: $8^3 \times 4, c_1 = -0.331, m_0 = 1.9, L_s = 24, m_f = 0.02$

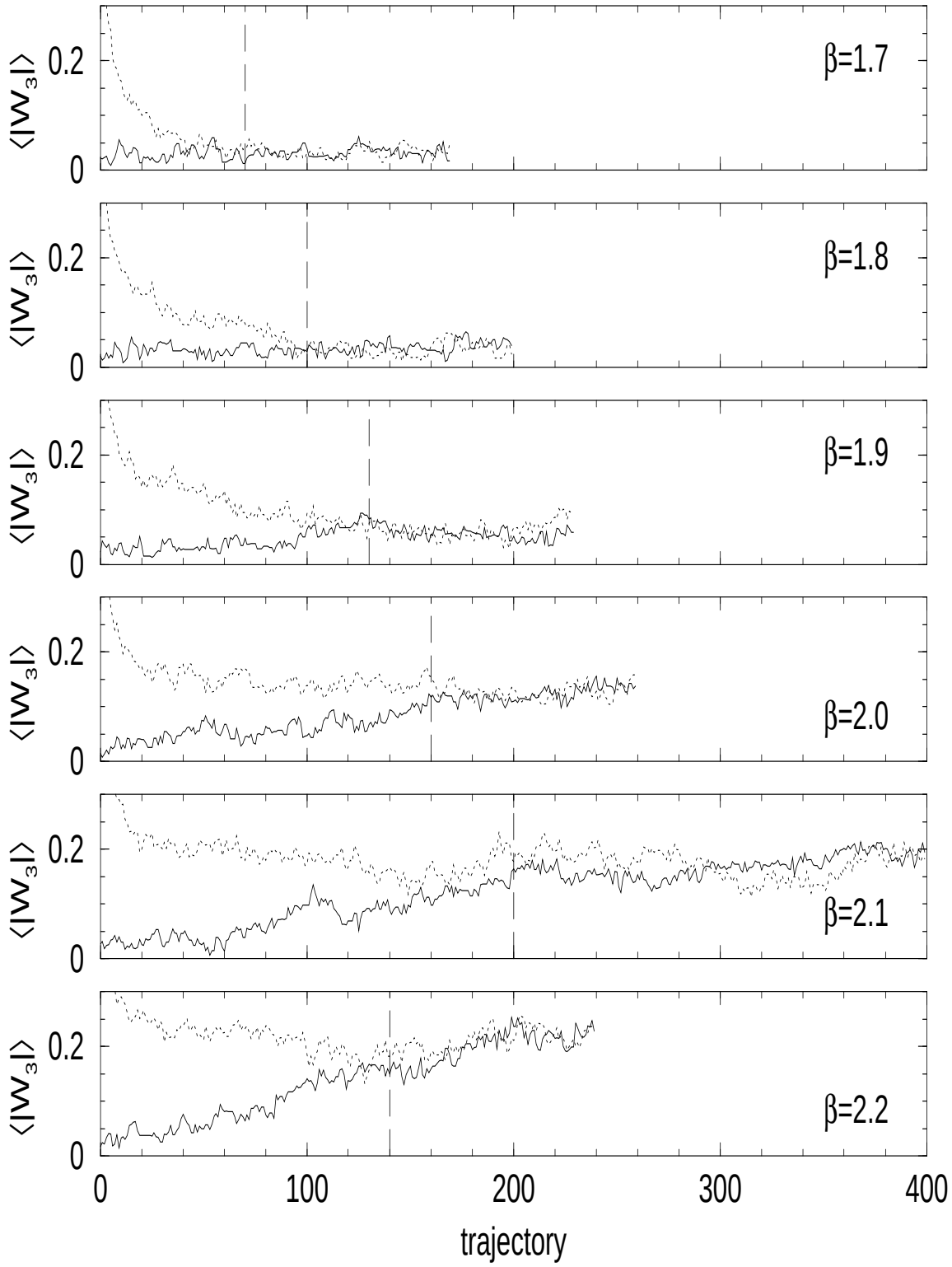


Figure 30: $\langle |W_3| \rangle$ evol: $8^3 \times 4, c_1 = -0.331, m_0 = 1.9, L_s = 24, m_f = 0.02$

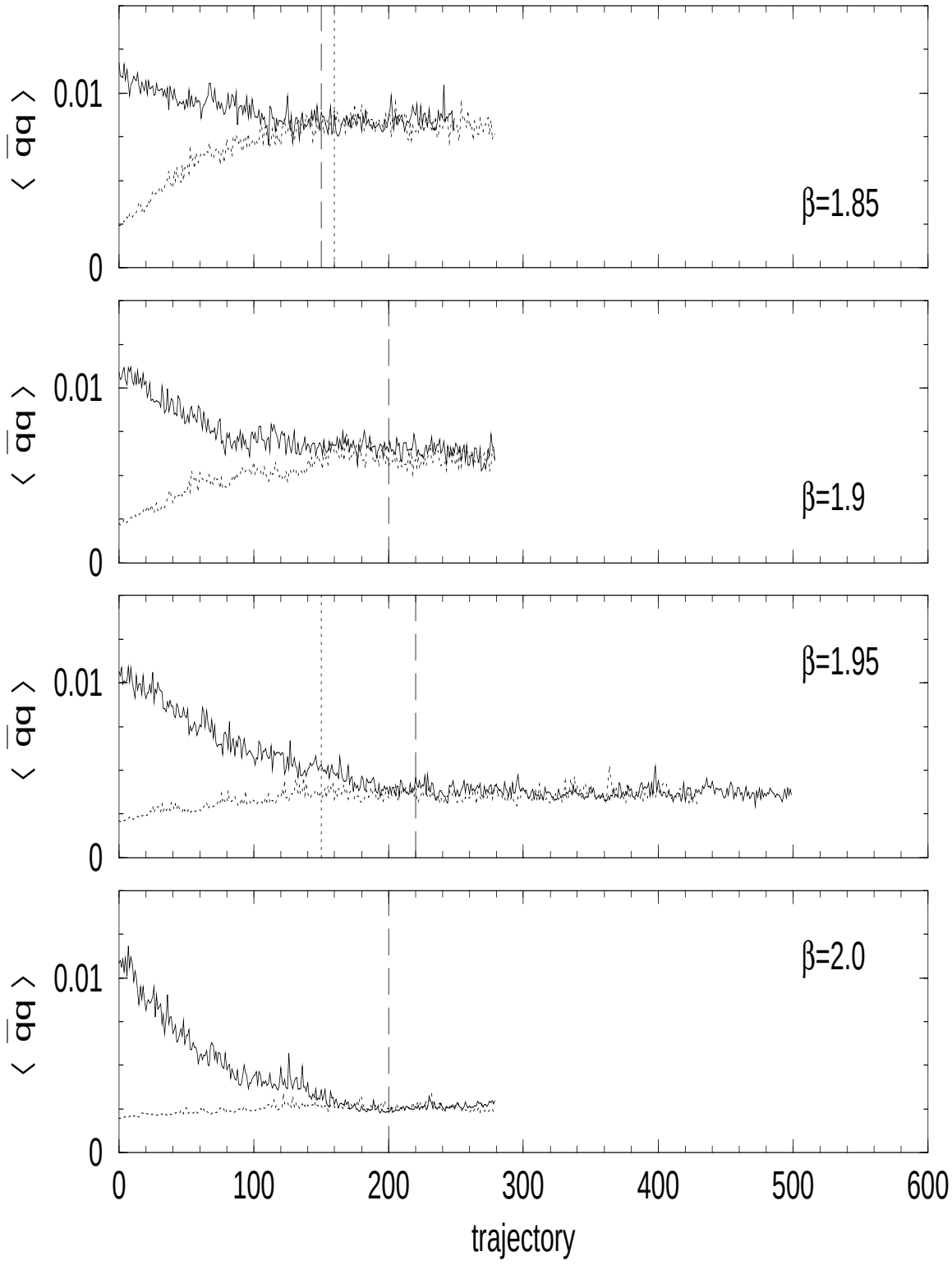


Figure 31: $\langle \overline{q}q \rangle$ evol: $16^3 \times 4, c_1 = -0.331, m_0 = 1.9, L_s = 24, m_f = 0.02$

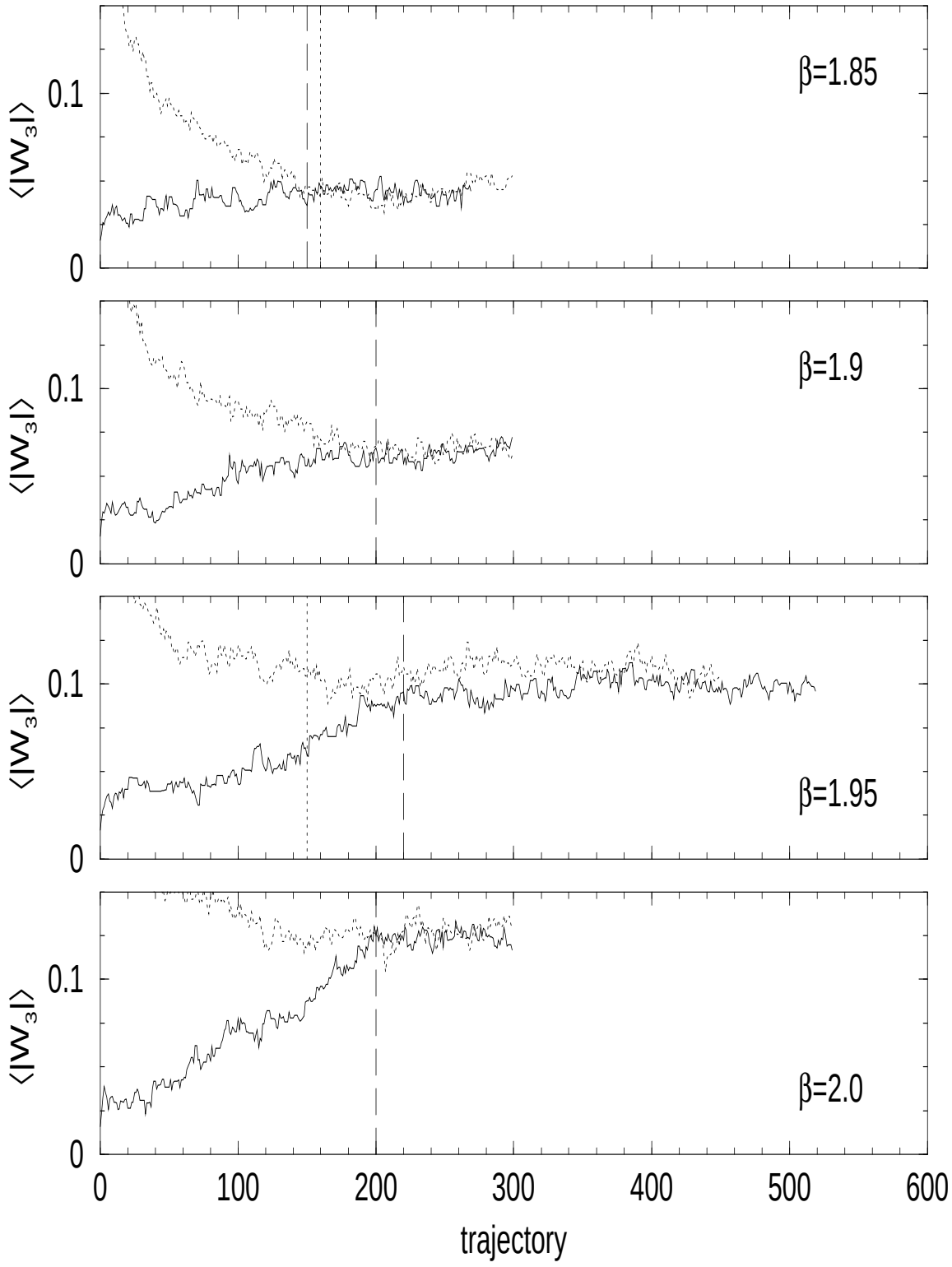


Figure 32: $\langle |W_3| \rangle$ evol: $16^3 \times 4, c_1 = -0.331, m_0 = 1.9, L_s = 24, m_f = 0.02$

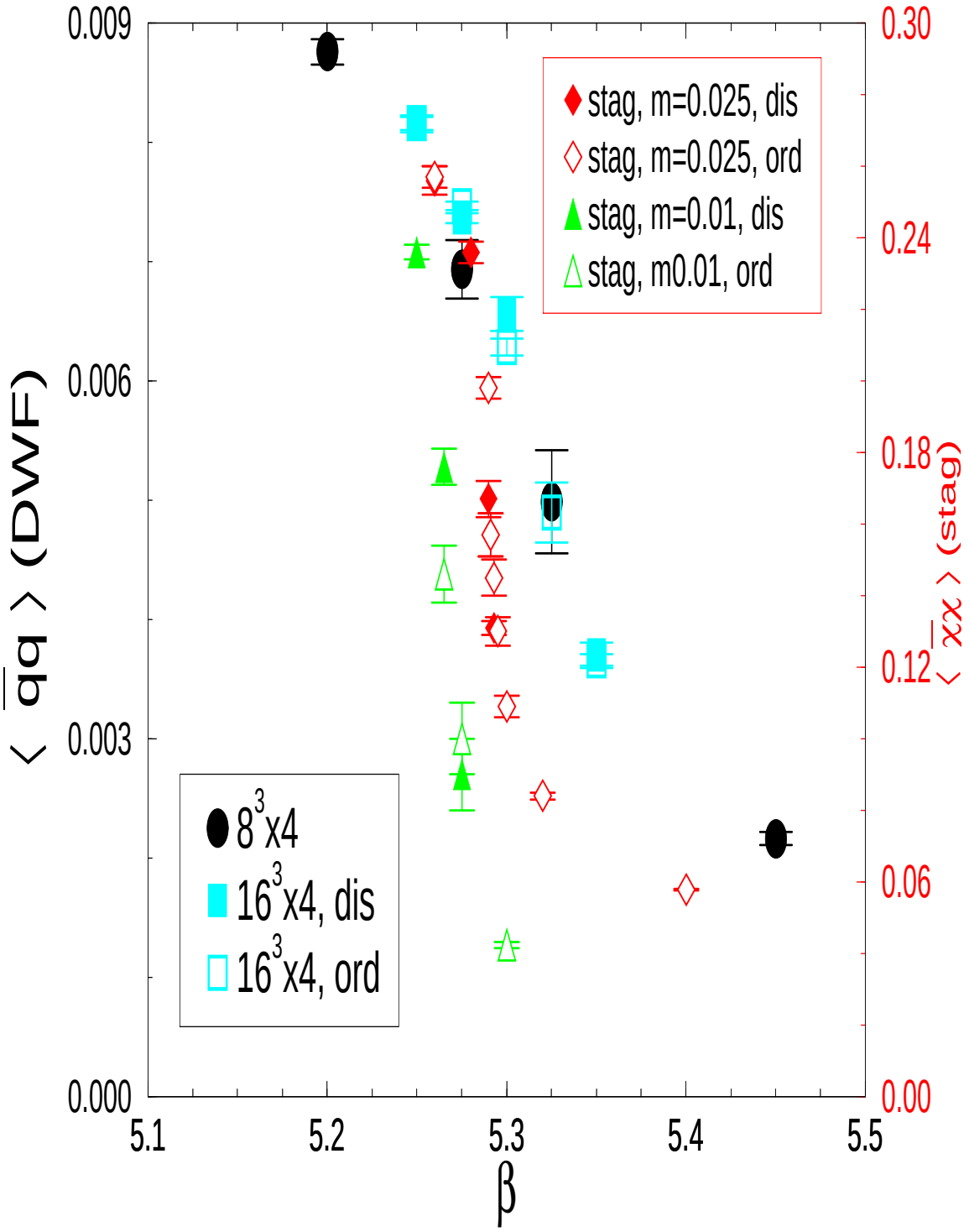


Figure 33: $\langle \overline{q}q \rangle$ *vs.* $\beta$: $16^3 \times 4, m_0 = 1.9, L_s = 24, m_f = 0.02$

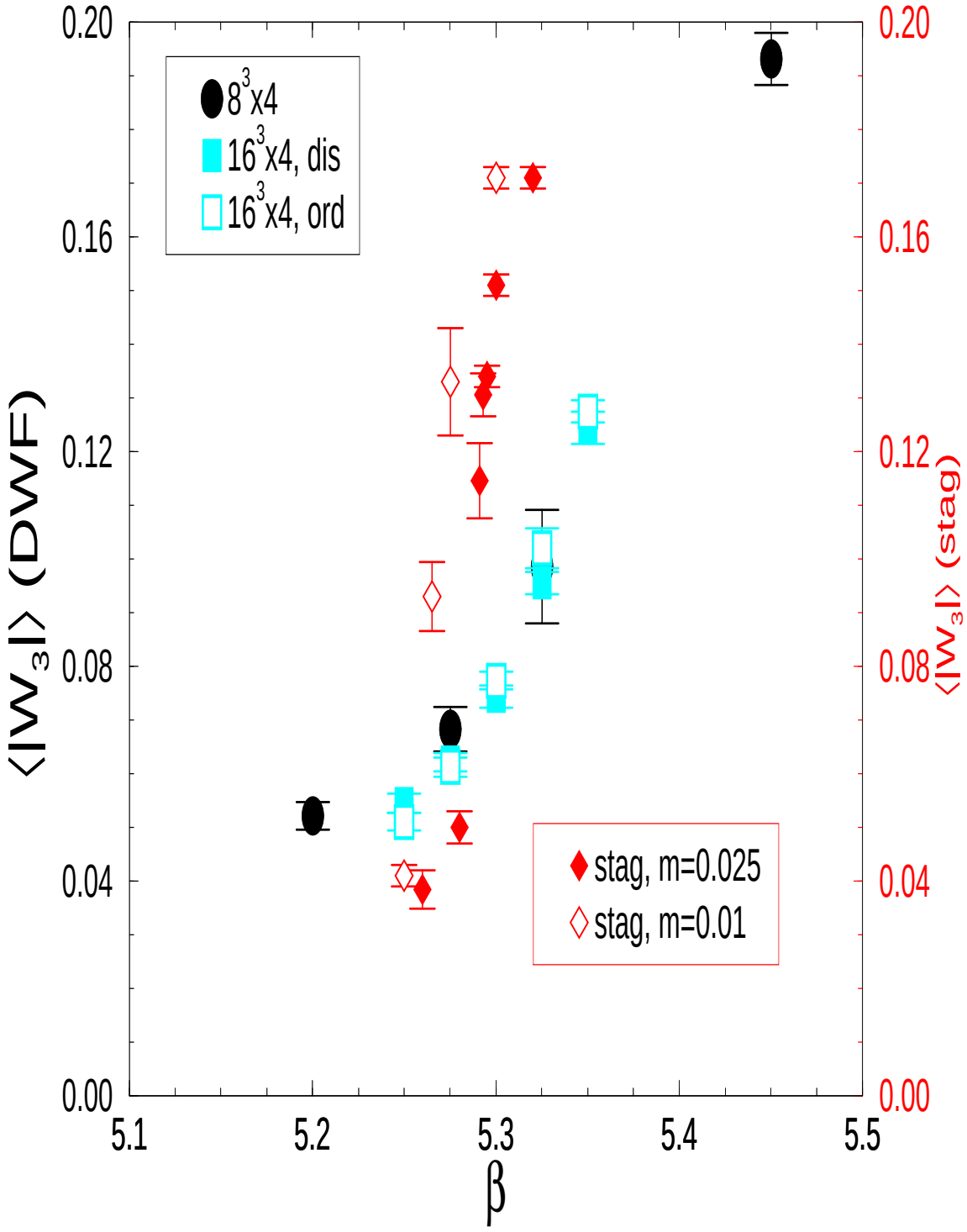


Figure 34: $\langle |W_3| \rangle$ *vs.* $\beta$: $16^3 \times 4, m_0 = 1.9, L_s = 24, m_f = 0.02$

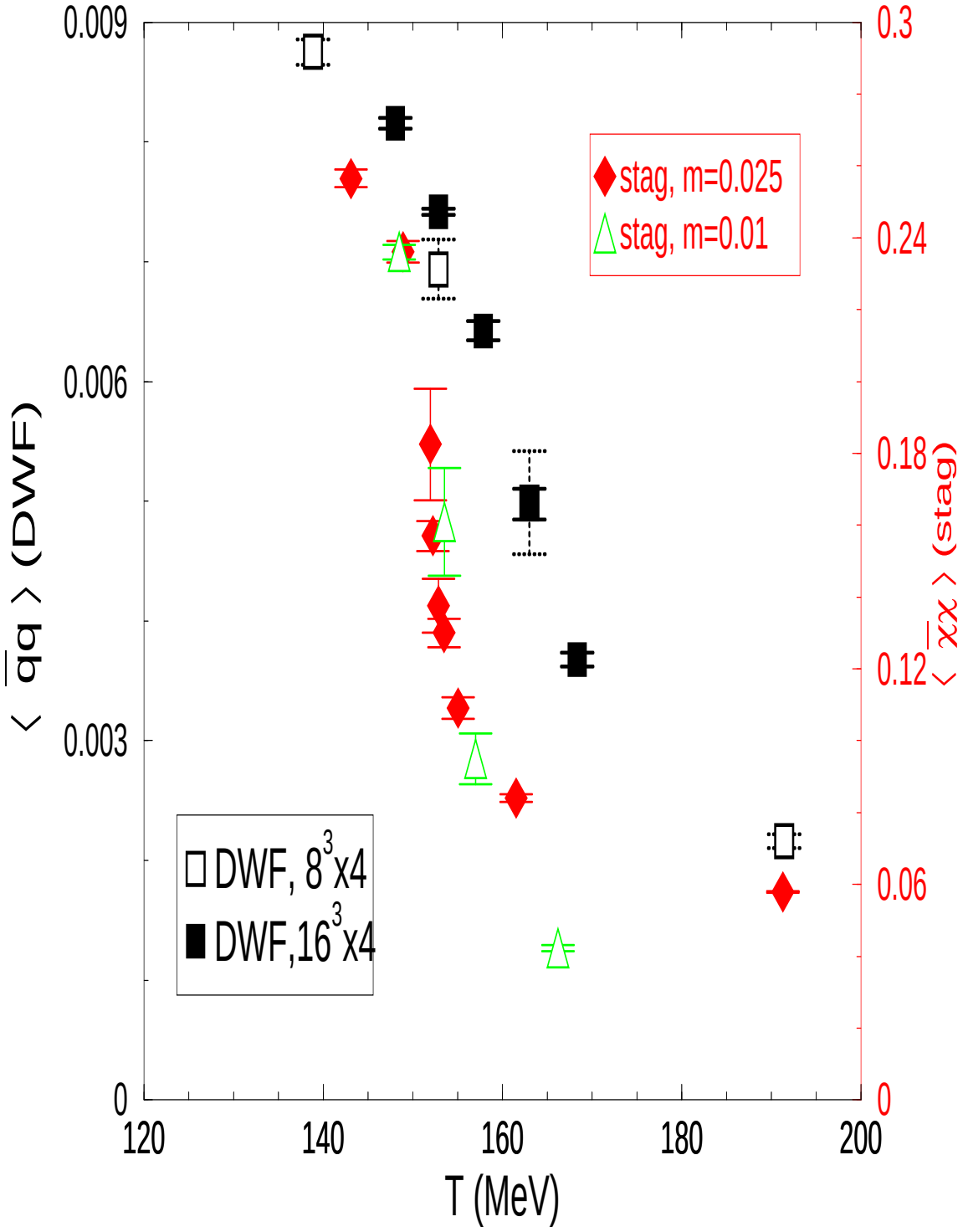


Figure 35: $\langle \overline{q}q \rangle$ *vs.* $T$ (MeV): $16^3 \times 4, m_0 = 1.9, L_s = 24, m_f = 0.02$

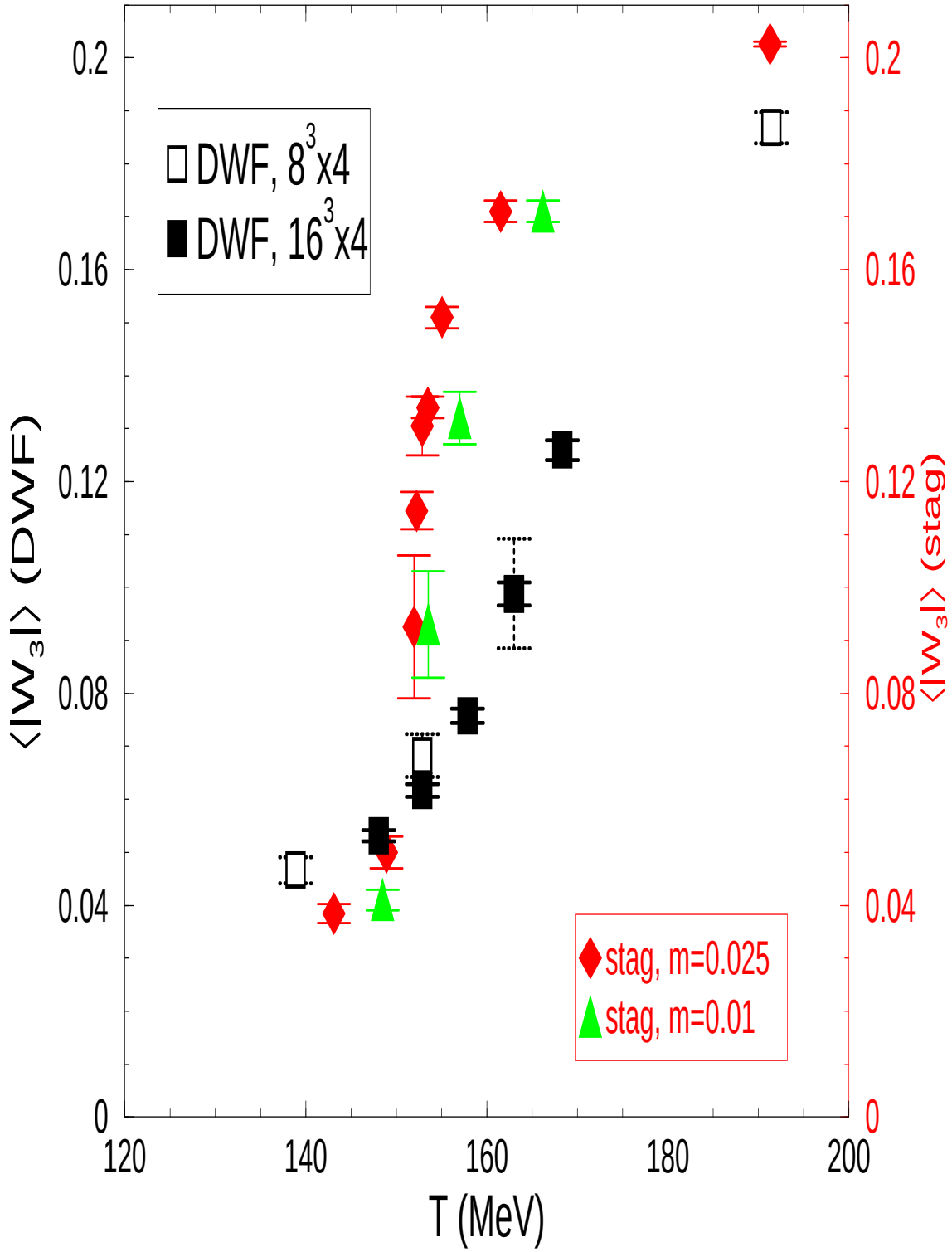


Figure 36: $\langle |W_3| \rangle$ *vs.* $T$ (MeV): $16^3 \times 4, m_0 = 1.9, L_s = 24, m_f = 0.02$

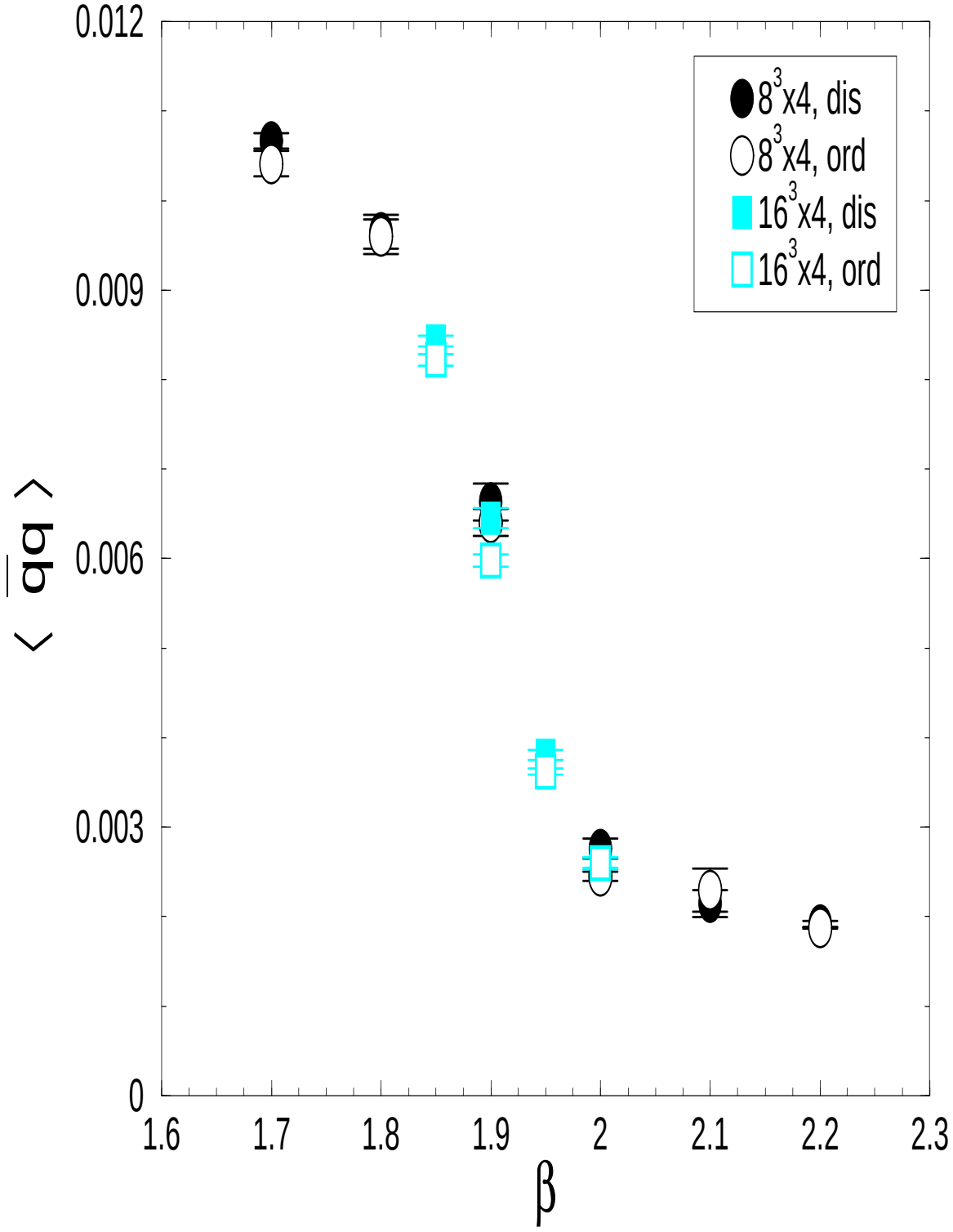


Figure 37: $\langle \overline{q}q \rangle$ *vs.* $\beta$: $16^3 \times 4$, $c_1$=-0.331, $m_0$=1.9, $L_s$=24, $m_f$=0.02

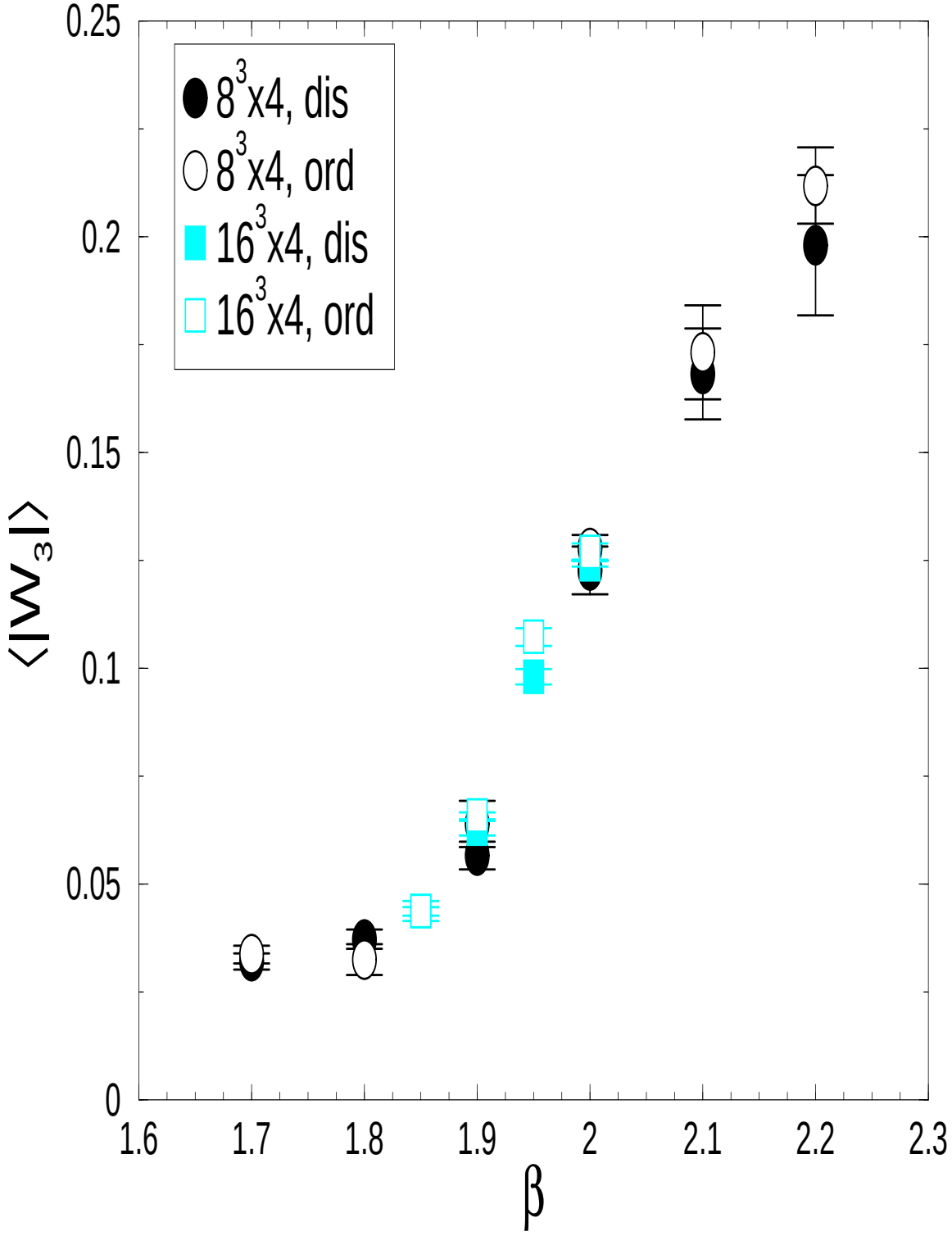


Figure 38: $\langle |W_3| \rangle$ *vs.* $\beta$: $16^3 \times 4$, $c_1$=-0.331, $m_0$=1.9, $L_s$=24, $m_f$=0.02

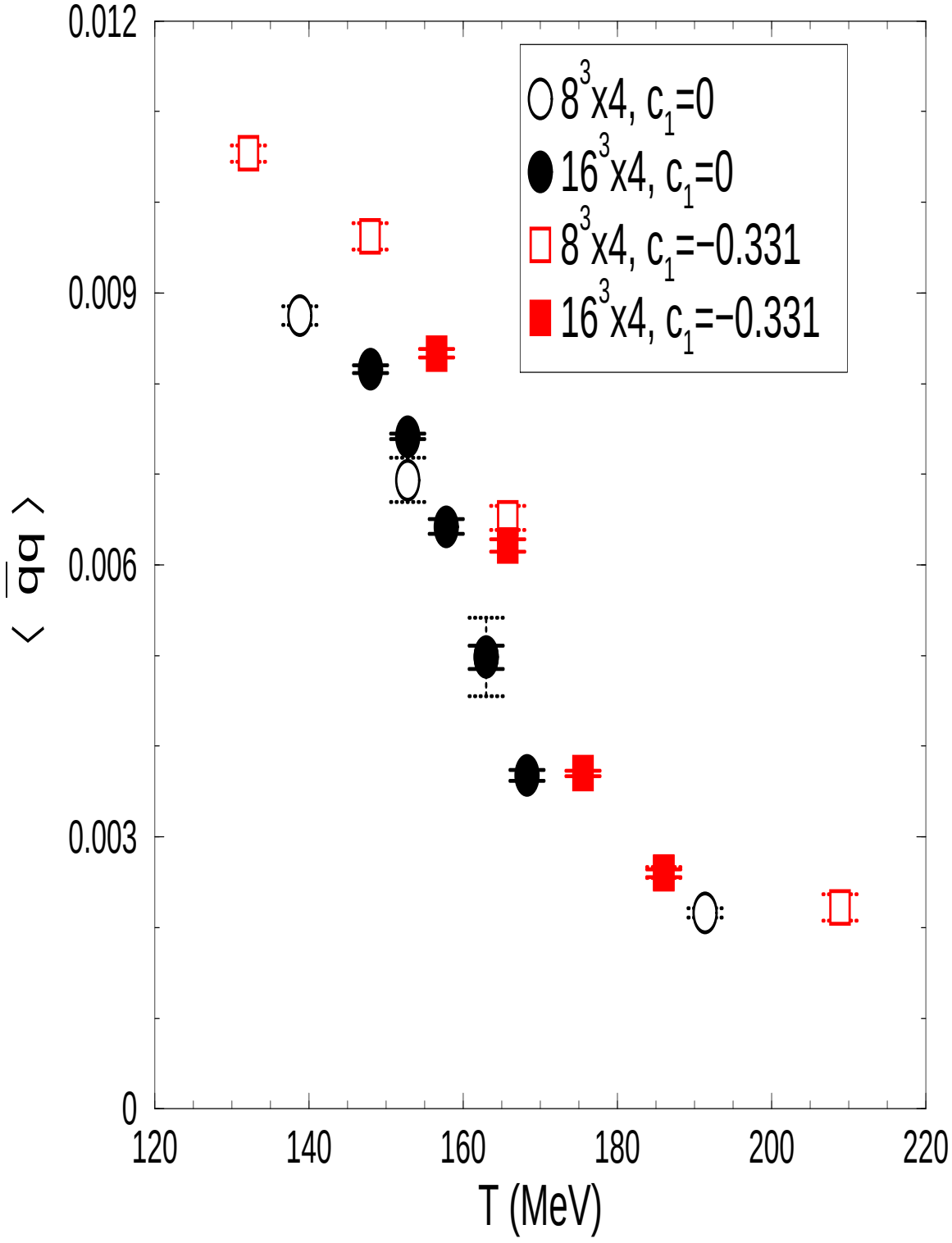


Figure 39: $\langle \overline{q}q \rangle$ *vs.* $T$ (MeV): $16^3 \times 4$, $c_1$=-0.331, $m_0$=1.9, $L_s$=24, $m_f$=0.02

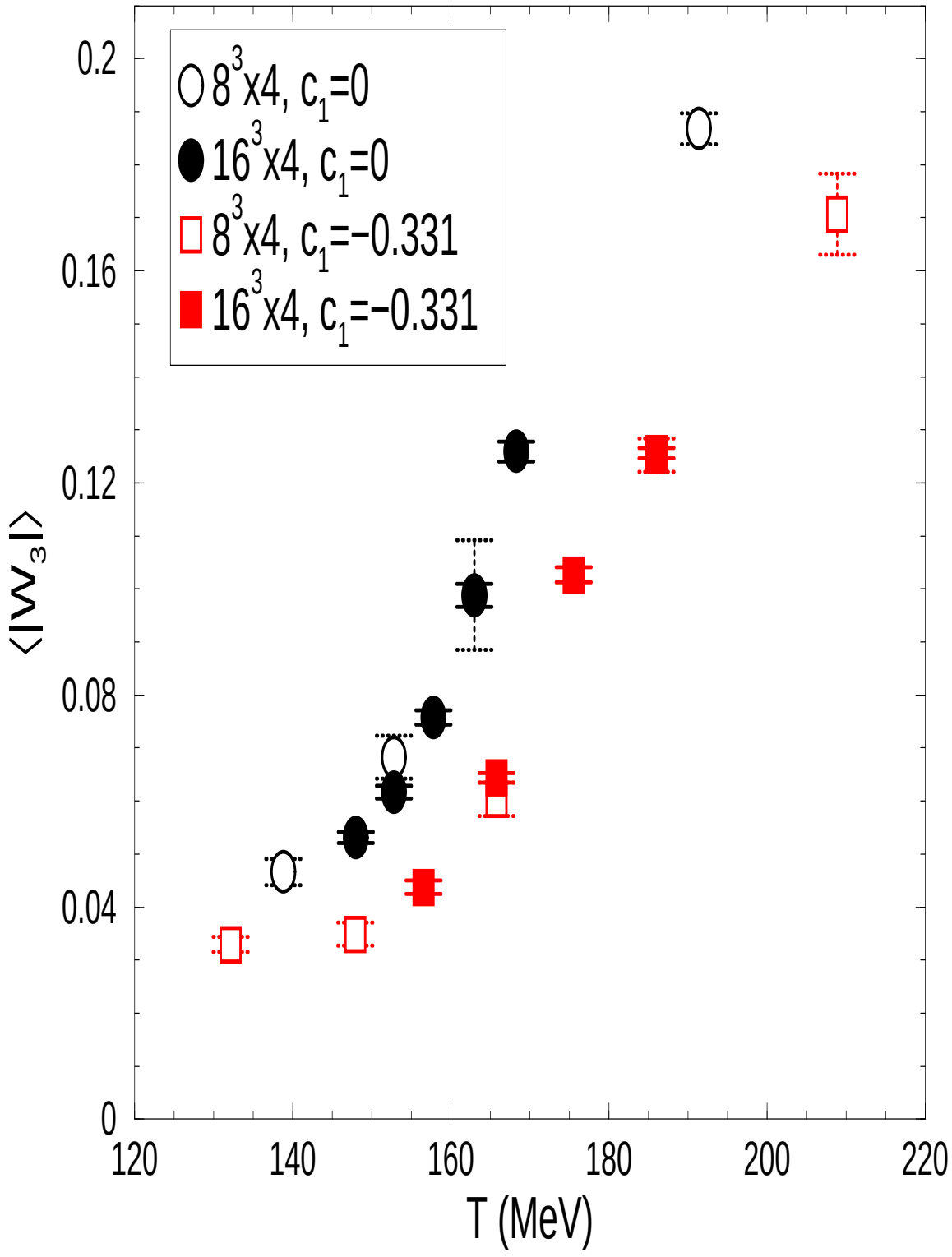


Figure 40: $\langle |W_3| \rangle$ *vs.* $T$ (MeV): $16^3 \times 4$, $c_1$=-0.331, $m_0$=1.9, $L_s$=24, $m_f$=0.02

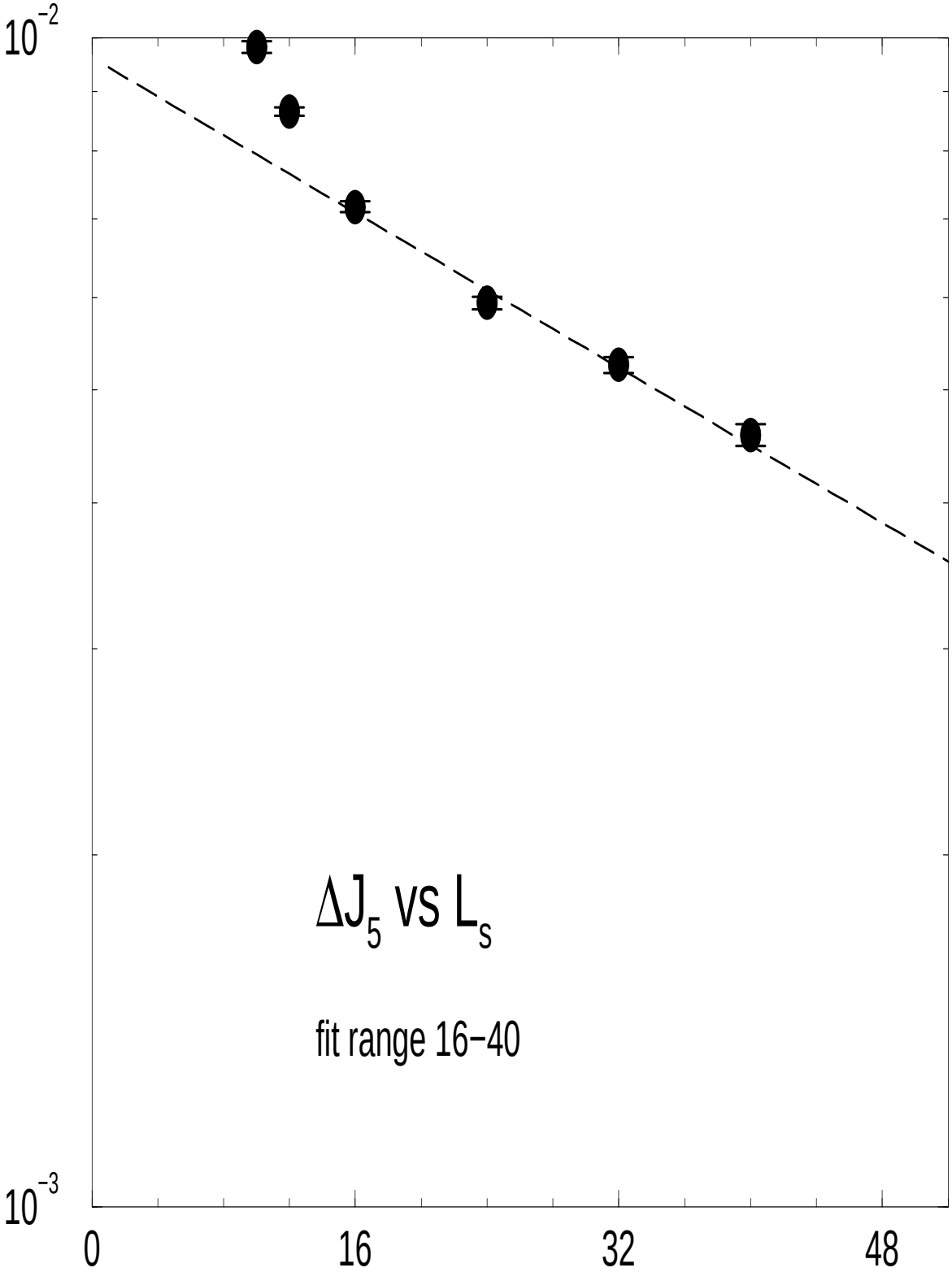


Figure 41: Fit of $\Delta J_5 = c_0 e^{-c_1 L_s}$; $8^3 \times 4, \beta = 5.2, m_0 = 1.9, m_f = 0.02$

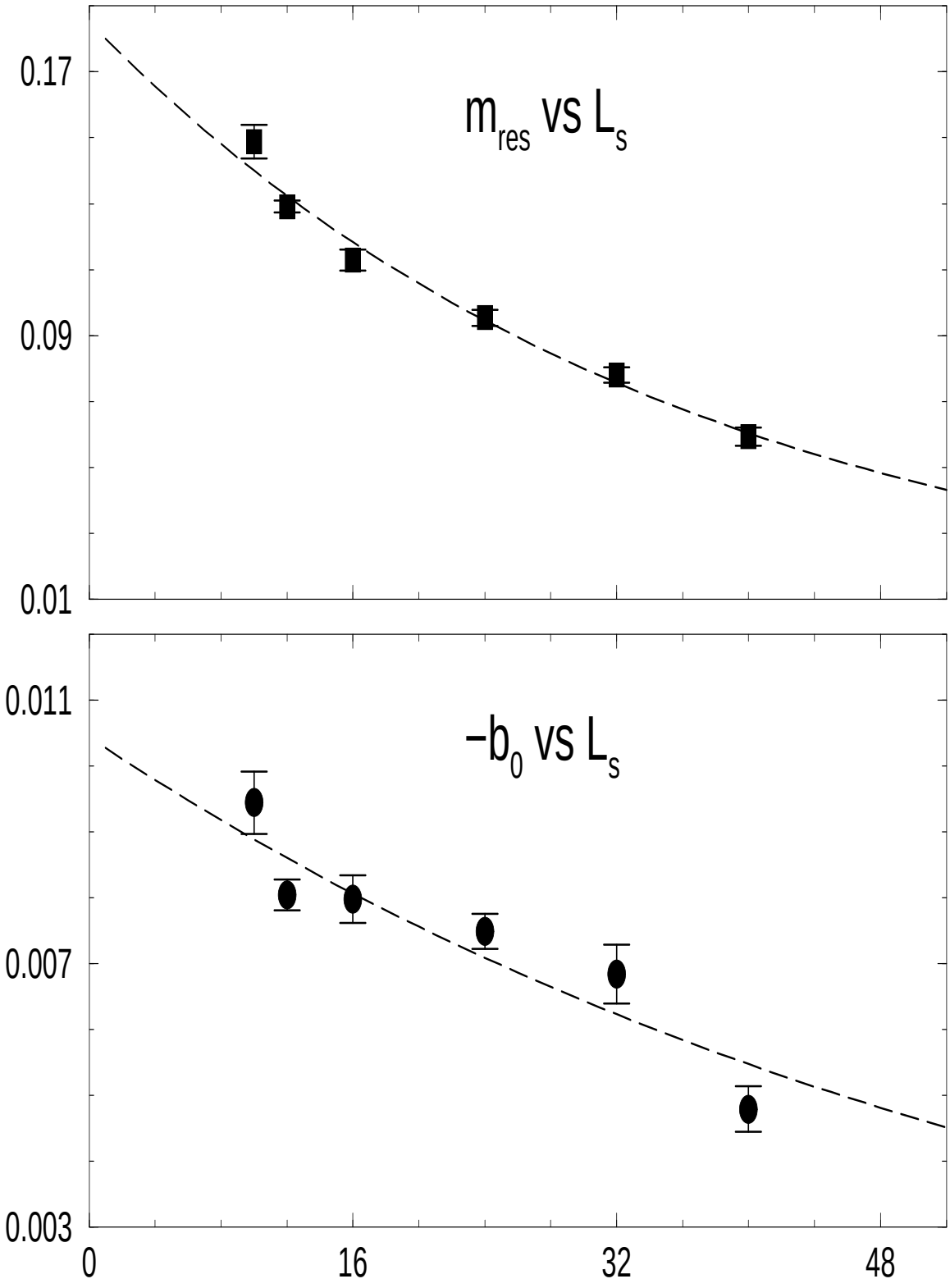


Figure 42: $L_s$ dependence of $m_{\rm res}$ and $b_0$: $8^3 \times 4, \beta = 5.2, m_0 = 1.9, m_f = 0.02$